Environmentally-friendly perovskite nanocrystals based on titanium and tin

Shanti Maria Liga

ICFO - The Institute of Photonic Sciences
Barcelona, 2023

Environmentally-friendly perovskite nanocrystals based on titanium and tin

Shanti Maria Liga

under the supervision of

Professor Gerasimos Konstantatos

submitted this thesis in partial fulfillment
of the requirements for the degree of

Doctor of philosophy in photonics

by the

Universitat Politècnica de Catalunya
Barcelona, 2023

Gracias quiero dar al divino
laberinto de los efectos y de las causas
por la diversidad de las criaturas
que forman este singular universo,
por la razón, que no cesará de soñar
con un plano del laberinto, [...]
por el hecho de que el poema es inagotable
y se confunde con la suma de las criaturas [...]
por la música, misteriosa forma del tiempo.

"Otro poema de los dones", J.L.Borges

Abstract

The availability of energy is a fundamental ingredient for the development of society. However, the intense consumption of fossil fuels as an energy resource since the second industrial revolution has caused a massive increase in the concentration of CO_2 and other greenhouse gases in the atmosphere, which is nowadays known to be the first cause of climate catastrophe. For this reason, it has become a priority to replace fossil fuels with more sustainable sources, which are renewable and produce low greenhouse gas emissions. Photovoltaics is one of the suitable technologies to carry out this fast transition because it is already well-developed and is based on the use of the infinite energy source, the Sun. However, increasing the efficiency of solar light conversion into electricity and reducing the cost of photovoltaic devices is fundamental to achieve the goals set by policy makers. Consequently, the development of novel optoelectronic materials, based on abundant and environmentally friendly elements, is one of the fundamental scientific advances needed to boost the shift towards a low-carbon society.

Perovskites, whose solar cells reached this year a certified record efficiency of 25.7%, are the first solution-processed materials to outperform multicrystalline and thin-film silicon and therefore one of the most interesting new materials for photovoltaic applications. In spite of their astonishing performances in solar cells, the most promising perovskites contain lead, which is toxic for human beings and potentially a threat to the environment. Hence, over the last decade, there has been intensive research on strategies to replace lead in the perovskite structure with nontoxic elements. Among all the novel perovskites studied, titanium-based vacancy-ordered double perovskites demonstrated one of the most promising performances when applied in solar cells.

This thesis focuses on the development of new solution syntheses for the preparation of novel lead-free vacancy-ordered double perovskite nanocrystals based on titanium and tin in the oxidation state +4, which are nontoxic and abundant elements. All the synthesized perovskite nanocrystals were characterized structurally, chemically and

optically. Moreover, the experimentally observed optical properties and the stabilities of these materials were further confirmed by ab initio density functional theory calculations.

We initially developed a colloidal synthesis to prepare mixed bromide-iodide $Cs_2TiBr_{6-x}I_x$ perovskites. All these materials are intrinsically stable with bandgaps in the visible region; suitable for solar cell applications. However, they showed very high instability in air, which prevented their application in devices and that motivated us to search for strategies to stabilize them.

Encouraged by the higher reported stabilities of Sn^{+4} perovskites with the same vacancy-ordered double perovskite structure, we synthesized pure tin halide perovskite NCs and novel mixed titanium/tin iodide and bromide perovskite NCs. The experiments confirmed that tin perovskites are stable in air and that the mixtures with the highest amount of tin in the structure are stable in air for longer than pure titanium perovskites. Finally, for the case of Cs_2TiBr_6, we developed a room temperature method to reach comparable stabilities in air through a surface treatment with tin compounds.

In summary, we have developed a low-temperature solution method for the preparation of novel environmentally-friendly perovskites based on tin and titanium and studied their properties for the first time, both computationally and experimentally. Finally, we have found a way to increase the stability in air of titanium-based perovskites through the addition of tin in the structure. Overall, this thesis provides an insight into novel lead-free perovskites based on titanium and tin and it represents a milestone for the understanding and development of this new class of materials.

Resumen

La disponibilidad de energía es un ingrediente fundamental para el desarrollo de las sociedades. A pesar de eso, el elevado consumo de combustibles fósiles como principal fuente de energía desde la segunda revolución industrial ha causado un aumento excesivo de la concentración de CO_2 en la atmosfera, que a día de hoy se ha reconocido como la primera causa del cambio climático. Por esta razón, se ha convertido en una prioridad remplazar los combustibles fósiles con fuentes más sostenibles, que sean inagotables y que produzcan una baja emisión de gases de efecto invernadero. La energía fotovoltaica es una de las tecnologías más adecuadas para progresar rápidamente en esta transición porqué ya está bien desarrollada y se basa en el uso de la energia solar, la cual es una fuente inacabable. Aún así, el aumento de la eficiencia del proceso de conversión de luz solar a electricidad y la reducción del coste de los dispositivos fotovoltaicos son fundamentales para conseguir a tiempo los objetivos establecidos por los órganos decisorios. Por lo tanto, el desarrollo de nuevos materiales optoelectrónicos, compuestos a partir de elementos que sean abundantes y respetuosos con el medio ambiente, es uno de los avances científicos fundamentales necesarios para impulsar este cambio hacia una sociedad "low-carbon".

Las perovskitas, cuyas celdas fotovoltaicas han alcanzado este año una eficiencia del 25.7%, son los primeros materiales procesados en solución que han superado las eficiencias obtenidas con el silicio multicristalino y con el silicio en lámina delgada y por eso están entre los nuevos materiales más interesantes para aplicaciones fotovoltaicas. A pesar de esto, las perovskitas más prometedoras contienen plomo, que es un elemento tóxico para los seres humanos y una amenaza potencial por el medio ambiente. En consecuencia, a lo largo de la última década, muchos proyectos de investigación se han centrado en la búsqueda de estrategias para remplazar el plomo en la estructura de las perovskitas con elementos que no sean tóxicos. Entre todas las nuevas estructuras estudiadas, las perovskitas dobles con vacantes ordenadas con base de titanio son las que han alcanzado uno de los rendimientos más prometedores en las celdas fotovoltaicas.

Esta tesis está centrada en el desarrollo de nuevas síntesis en solución para la preparación de nuevos nanocristales de perovskitas dobles con vacantes ordenadas de titanio y estaño en estado de oxidación +4, ambos elementos abundantes y no tóxicos. Todos los nanocristales de perovskitas que han sido preparados fueron caracterizados estructural, química y ópticamente. Además, las propiedades ópticas y las estabilidades observadas experimentalmente han sido confirmadas mediante cálculos de la teoría del funcional de la densidad ab initio.

Inicialmente, se ha desarrollado una síntesis coloidal para preparar perovskitas mixtas de ioduro y bromuro de cesio y titanio con fórmula $Cs_2TiBr_{6-x}I_x$. Todos estos materiales tienen brechas de bandas en el visible, entonces serian aptos para aplicaciones en celdas solares. Por otro lado, tienen una inestabilidad muy alta en aire, que impediría cualquier aplicación en dispositivos, y que nos ha impulsado a focalizarnos en la búsqueda de estrategias para estabilizarlas.

Motivados por las altas estabilidades en aire reportadas en las perovskitas análogas que contienen Sn^{+4}, se han sintetizado las perovskitas nanoestructuradas de estaño y de titanio y estaño. Se ha observado que las mezclas con el porcentaje más alto de estaño en la estructura son estables en aire por un tiempo más largo que las perovskitas a base de titanio. Finalmente, para el caso de Cs_2TiBr_6, se ha desarrollado un método para conseguir una estabilidad comparable, mediante un tratamiento superficial a temperatura ambiente utilizando compuestos de estaño.

En resumen, se ha desarrollado una nueva síntesis en solución para la preparación de nuevas perovskitas sin plomo a base de estaño y titanio y se han estudiado por primera vez sus propiedades mediante métodos experimentales y computacionales. Finalmente, se ha encontrado una manera para mejorar la estabilidad en aire de las perovskitas a base de titanio, mediante incorporación de estaño en la estructura. En general, esta tesis aporta un entendimiento de las nuevas perovskitas dobles con vacantes ordenadas de titanio y estaño y representa un punto de referencia por la comprensión y el desarrollo de esta nueva clase de materiales.

Acknowledgements

This work wouldn't have been possible without the support of all the wonderful people that have been around me in the last 4 years. Here I would like to express my gratitude to all of those who helped me in different ways to accomplish this work.

First of all, I would like to thank my supervisor Gerasimos Konstantatos for giving me the opportunity to be a part of the group. Thanks for the support, for guiding me with your experience, for being always available to discuss anything and giving me all the freedom in my research.

The calculations reported in this thesis have all been carried out by Sean Kavanagh. Sean, thanks for the great collaboration, the theory explanations, the interesting discussions. I learned a lot from this collaboration.

The TEM experiments showed in this work were carried out at the University of Barcelona, under the guidance of Lluís Conesa. Thank you for always being so helpful, for aligning back the electron beam when I lost control of it and for being so available and friendly.

The XPS experiments were carried out at ICN2, by Guillaume, which I would like to acknowledge for being my point of reference for solving all the doubts during the analysis of the XPS spectra. Thanks for your availability and kindness.

During my PhD, I spent a lot of time in the lab and in the office with many people that made my life at ICFO always happy and warm.

Eh! Si la nit t'espanta vine aquí
Tinc un circ de cançons fins a l'alba
Eh! Quan et plogui a dins vine a casa
Tanca els ulls si no veus el camí

Starting from the person that seats behind the wall of monitors that I've built in front of me in the last months, I would like to thank the QDs queen, my officemate and

labmate, Mariona. I cannot imagine these 4 years without you. Thanks for all the infinite help in the lab, for your psychological support when everything was so unstable (my samples mainly), for the chemistry talks, the talks with the door closed, the laughts to tears, the singing in the lab, and the incredible flight together in Ager! Me lo he pasado genial contigo! Sos lo más, boluda!

Then I want to thank Guy, first of all for being the best and my exclusive salsa partner, for giving me a lot of light-hearted moments with his amazing rhythm, but also for all the walks (the "short" and the long) after lunch talking about everything and for accepting my extreme sensitivity during the thesis writing and supporting me always! Thank you also for helping me with the PL doubts and listening to my research worries... and for the birthday cakes, every year more delicious. 12 minutes??

Iñigo and Ignasi, the Pedrogrullo team, me encanto compartir los primeros años aquí con vosotros, la carrera de 10k, las primeras veces en bici hasta ICFO, los baños en invierno, los bares en Sants, las charlas sobre solar cells y no. Habéis sido una fuente de inspiración con vuestra pasión por la ciencia más allá del laboratorio. Sois 2 cracks.

Then the lunch/beachvolley/ski team: Onur, cacik, thanks for the support with all the thesis bureaucracy and for understanding my irrational stress, for the lab cleaning together that was always fun. Overall, it was... good; Nima, thanks for making our lunches lighter with your real but fantasy stories, it was cool to have lunch with a movie star, director, personal trainer, hair model and more; Katerina, thanks for many things but above all for motivating everyone to play beachvolley, we needed you; Miguel el niño, sin tus SaladitasSalgaditas los ultimos meses hubieran sido mucho peores, gracias por intender mis necesidades, y gracias por el IT support y mucho màs; and the new entry Hamed, thanks for your kindness and I'm sorry for your chicken.

Then I would like to thank all the other people of the group, for creating a peaceful working environment filled with kind and happy moments. Shuchi, for welcoming me when I arrived; Yongjie and Zhuoran for your availability in sharing your experience and knowledge on solar cells and on the preparation of various ELT and HTL materials; Jae Taek for his fantastic corean humor; Lucheng for being the only one understanding my problems with perovskites and for transforming the fights for the glovebox in fun moments together with Debranjan and Avijit. Thanks Stephy for your kindness and for the Kerala vibes you brought to the group, and thanks to Gaurav, Shanmukh, Adi, Yurong, Hyun-Soo, Goretti and Zafer; it was nice to spend time with you in the lab.

Outside the group, some people at ICFO warmed up the freezing ambient of the

allseasonsopenwindows-Cafè la Llum. Alfredo y Nacho, gracias por los desayunos felices, los chistes tontos, las carreras en las escaleras, y Alfredo grazie per avermi salvato aiutandomi a friggere quelle panelle. Solo tu potevi farlo. E grazie pure per avermi aiutato a strutturare la tesi e aver ascoltato i miei dubbi esistenziali sul nulla, sei un grande! Baja Nacho. Together with them, I'm happy that in the last year new people joined our breakfasts, Fede, Paolo, Stefano, thanks for your super cool company, the beers, the running and the climbing. And, finally, thanks to the nice and smiling people that made us coffee every morning, Silvia, Maria, Paki and Joana.

Thanks to Seba, for passing by my office in the late afternoon for some fun conversations, to Robin to be my friend outside ICFO but only a very far person inside and Hani for the happy moments climbing in the tunnel during the very tough period of the toque de queda.

Tu vestido agua marfil
Salió volando a todos lados
Estallo en un mar sin fin
Sirenas cantaban al costado

Gracias a mis compis de piso de los ultimos 2 años, moshishas y no, por construir juntos un ambiente lindo donde volver a la noche. Gracias Oli y Lu, por ser dos amigas que están siempre con las cuales he compartido momentos lindos y duros, y que son las mejores compis de piso que podia imaginarme! Gracias por vuestra alegria y por ser siempre propositivas. Gracias Lau por saber escuchar y saber reírse un montón, Mario por compartir las dudas existenciales del PhD con una cerveza, Juan por sus quesadillas y charlas de cine, Alfo por el ajedrez y la guitarra que me han mejorado muchas noches.

Gracias a los primeros dos argentinos que cruzaron mi camino en Barcelona hace 4 años. Pedro porqué es la paz en persona y lleva tranquilidad en todas partes vaya. Emilio, por los suspiros compartidos, de 1 a 2 te agradezco 2 por el tiempo pasado juntos. Lucia también, para enseñar a dejarlo fluir.

Grazie Leone per gli aperitivi, le passeggiate, le conversazioni profonde e divertenti, per aver migliorato alcune giornate con la tua fantasia e la tua sensibilitá.

Gracias a los amigos de escalada, a Juani y Nati, Juani por todos los tzaaaa y Nati por los budines de banana. Gracias al boludo más boludo del mundo, Ber, por haber compartido un montón de momentos de ligereza y felicidad juntos, por subirme como una bolsa de papas cuando no podía mas, para compartir xuxos conmigo, y vos qué vas a comer? Gracias también por todas las charlas de vida/doctorado que me han

ayudado entenderme más.

Ci si risveglia ancora in questo corpo attuale
Dopo aver viaggiato dentro il sonno
L'inconscio ci comunica coi sogni
Frammenti di verità sepolte
Quando fui donna o prete di campagna
Un mercenario o un padre di familia

Vieni a prendere un tè
Al "Caffé de la Paix"?
Su vieni con me

Grazie ai miei amici di sempre di Palermo, a Stefi, Giorgio e Costanza A.S.I.N.C.E.D. per il sostegno in questi anni, ad Angelo per le rubriche del cuore e le scalate in Sicilia. Grazie Fra per esserci stata sempre nei momenti difficili e nei capodanni felici, per la tua fantasia e allegria.

Grazie ad Aldo e Antonio, per essere stati due punti di riferimento da sempre e per avermi fatto sentire di essere vicini in questi ultimi anni passati lontani.

Grazie alla nonna, che mi ha insegnato a provare sempre ad essere una persona migliore.

Grazie ai miei genitori, per avermi trasmesso la fantasia e la curiositá che mi spingono a fare tutto ció che mi piace, per avermi sostenuto sempre in questi anni ed essere stati sempre presenti.

Shanti, December 2022, Barcelona

Contents

Acronyms and Symbols

DMF Dimethylformamide

DMOP 3-(N,N-dimethyloctadecylammonio)propanesulfonate

DMSO Dimethylsulfoxide

EDX Energy-Dispersive X-ray Spectroscopy

FFT Fast Fourier Transform

HRTEM High-Resolution Transmission Electron Microscopy

MA Methylammonium

NC Nanocrystal

OA Oleic acid

OLam Oleylamine

ODE 1-Octadecene

PCE Power Conversion Efficiency

PL Photoluminescence

PV Photovoltaic

TMS Trimethylsilil

XRD X-Ray Diffraction

1

Introduction

1.1 Context

The last few years have been the stage of the biggest challenges that European countries have been facing since the second world war. It became a priority to achieve energy security in a sustainable way, both in the sense of CO_2 production reduction and attention on resources distribution and depletion. Indeed, while the availability of energy is fundamental for the development and wealth of societies, it is nowadays known that the emission of CO_2 associated with energy production from fossil fuels combustion over the last 2 centuries is the principal cause of global warming. [1] Therefore, the transition to renewable energy resources has been set as a priority by the United Nations and many experts have already identified Photovoltaics (PV) as the fundamental technology for cost optimized climate change mitigation. [2–5] Contrary to other renewable energies, such as hydropower or geothermal energy, solar energy has the advantage to be potentially harvested everywhere in the world, which makes it strategic in order to avoid the hazardous situation of energy dependence from few other countries. However, this is entirely true only if solar technologies are constituted by elements that are abundant across many regions of the world, a condition that

makes possible to diversify the resources suppliers. Increasing the installed PV power to a level sufficient to support the energy transition, while limiting the costs associated with it and making it doable from a resource point of view, is possible only considering a fast development to more efficient technologies, which determines a reduction of materials usage. This technological development must be done considering the large-scale production required for the next century transition, which entails avoiding rare elements and, on the contrary, implementing the usage of abundant elements, while considering their toxicity for human beings and their potential negative impact on the environment.

1.2 Efficiency and new applications

The total solar power incident on earth is 1.7×10^5 TW, while in 2021, only 0.11 TW was generated from solar PV power in the world, [6] a representative comparison of how little and inefficiently we still exploit this massive sustainable energy resource. On the other hand, the main scenarios for climate change mitigation consider that the installed PV capacity should increase 20-fold by 2050. [7] One of the necessary conditions to achieve such a high installed power is to increase the solar cells efficiency, where the efficiency is defined as the output power divided by the power of the incident sunlight. Nowadays, the efficiency of common silicon solar panels available in the market is around 20%, even though silicon heterostructure solar cells reached 26.7% efficiency in 2017. Noteworthy, the maximum theoretical efficiency for a solar cell made with one absorbing material is around 33.6%, for a bandgap at 930 nm, corresponding to InP (1.34 eV) and close to GaAs (1.44 eV, 860 nm). [8] The lower bandgap of silicon (1.1 eV) results in a maximum theoretical efficiency of about 32%, which is still relatively far from the value reached in 2017 but that has not increased in the last 5 years, demonstrative of the difficulty of overtaking this record.

An alternative technology to harvest a higher percentage of sunlight and push the efficiency limits to higher values is that of tandem solar cells, which are solar cells where one or more intermediate bandgap materials are deposited on top of a narrow bandgap material in order to absorb over a broader range the solar radiation while reducing thermalization losses, which are the largest source of power loss in PV solar-energy conversion. [9] This year, a record efficiency of 31.3% was reached for tandem silicon/perovskite solar cells. [10] Moreover, the potential of triple junction perovskite/perovskite/silicon [11] and all-perovskite triple-junction [12] solar cells was also already demonstrated, showing the very high potential of perovskite materials for the development of new PV technologies.

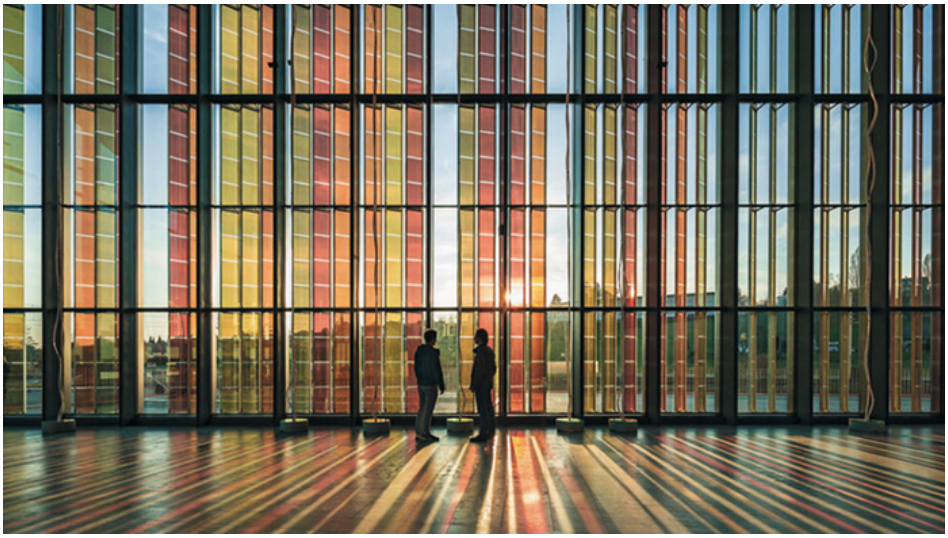

Figure 1.1: Dye solar cell façade of SwissTech convention center, EPFL, Switzerland, made by Solaronix. Picture taken from Science

Another way to boost the energy transition through solar light harvesting is by exploiting the vertical space of cities, developing innovative solar technologies that can be incorporated in windows or on buildings' walls, as shown in Figure 1.1. Also for these new applications, perovskites have been found to have the suitable properties [13, 14] and for this reason they represent nowadays one of the most interesting emerging PV materials.

1.3 Perovskites, from their discovery to solar cell application

Perovskites are defined as any materials with the same cubic structure of calcium titanate and chemical formula ABX_3. [15] Hundreds of different materials adopt this structure and depending on the elements constituting them, they acquire different properties, making them suitable for a multitude of applications, as insulating, thermoelectric, semiconducting, conducting till superconducting materials. Perovskites that are applied in solar cells most commonly contain a halide anion as X component, Pb^{+2} or Sn^{+2} as B component and Cs^{+1} or an organic cation such as methylammonium (MA) as A component. In this latter case, they are called hybrid organic-inorganic perovskites and are those that historically paved the way towards the discovery of the optimal optoelectronic properties for PV applications. These kind of perovskites, specifically organic-inorganic iodoplumbate and bromostannate perovskites, were synthesized for the first time in 1978. [16, 17] Around 15 years later, the studies of Mitzi et al.

demonstrated their semiconducting properties, [18,19] though they were not employed in PV applications until 2009, when for the first time methylammonium lead iodide ($MAPbI_3$) was used in a liquid-electrolyte-based dye-sensitized solar cell, reaching an efficiency of 3.9%. [20] The impressive performance of $MAPbI_3$ as light harvester came together with the observation of its instability in the electrolyte, which was consequently replaced in 2012 with a solid organic hole conductor. [21,22] In the same year, it was demonstrated for the first time that halide $MAPbX_3$ were not only good light harvesters but could also act as both n-type component in dye-sensitized solar cells, transporting the electrons through their thickness to the electrode surface, [23] and as p-type layer. [21,24] Ultimately, it was demonstrated that they could assume all the principal roles of PV operation, namely light absorption, charge generation and charge separation. [25] From 2012 perovskite solar cells' efficiency has shown a tremendous increase reaching 25.7% this year, [10] being the PV technology that demonstrated the steepest efficiency increase ever.

The astonishing performance of perovskites in solar cells, which is related to their outstanding optoelectronic properties, [26–28] would not be so unique in the PV field if it was not combined with the ease of synthesis of perovskite thin films, which involve low-temperature and solution-based deposition, as well as with the facile replacement of the elements in the crystal structure, which allows to tune the optoelectronic properties of the material. The low-temperature synthesis and bandgap tunability in combination with the optimal optoelectronic properties, make perovskites one of the most interesting materials in the world of new generation PVs.

1.4 Perovskite NCs

In 2015, perovskites were synthesized for the first time as nanocrystal quantum dots (Figure 1.2), [29] which are nanoparticles with a size smaller than their Bohr radius, a condition in which the band structure of the materials depend upon the size and shape of the particles. The history of nanocrystals (NCs) dates back to thousands of years ago: lead sulfide NCs were used 4000 years ago by Egyptian to dye their hair, [30] while in the Middle age copper NCs were used to paint ceramics [31] and in the Renaissance period silver and gold NCs were used to fabricate stained glass, used in the windows of cathedrals. [32] Nevertheless, the first scientific study on size dependent optical properties of NCs was carried out by Michael Faraday in 1857, when he accidentally observed that gold leaves of different thicknesses showed different colors. [33] Yet, only in 1986, after the transmission electron microscope (TEM) reached a sufficient spatial resolution to observe the NCs, they were finally able to compare the theoretical models developed over this period of time with experimental data. [34] The vast research on the

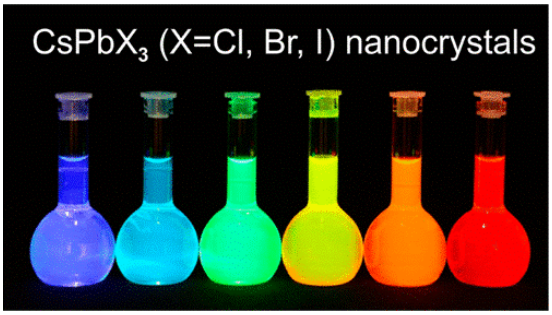

Figure 1.2: Cesium lead halide nanocrystals solutions. From left to right X= Cl, Br and I. Taken from [29]

synthesis of novel NCs and on their application for the development of new technologies started only in 1993, when Bawendi's group reported the first synthesis with good control over the size and shape of colloidal CdE (E = Sulfur, Selenium, Tellurium) NCs, [35] where the word "colloidal" indicates that the NCs are durably suspended in a solution. The ability to synthesize the NCs suspended in a solution is a great advantage when it comes to deposit the NCs as thin films in order to fabricate devices. Indeed, when the NCs in the colloidal solution are well-dispersed, i.e. they do not aggregate, they can be deposited as thin films with simple deposition techniques like spray painting or inkjet printing, which is an attracting feature for industrial applications. With regard to perovskite NCs, their most interesting properties compared with polycrystalline thin films are the tunability of the bandgap through NCs size variation; [36, 37] a higher stability towards phase transition; [38–41] the tunability of the properties through ligand engineering, [42] where the ligands are the molecules attached to the surface of the NCs that stabilize them in solution; the sharp photoluminescence (PL) peak and photoluminescence quantum yield (PLQY) close to unity; [43–45] the negligible electron or hole trapping; [46] and finally, the fact that, contrary to polycrystalline thin film deposition, the perovskite crystallization and the film deposition are two separate events, which enables higher control on both processes. Despite all these advantages, perovskite NCs still have a lower efficiency in solar cells compared to bulk because the charge transport is less effective, due to the isolated NCs and the necessary step of the ligand exchange that leaves the NCs with defects on the surface. [44, 47]

From 2016, when the first perovskite $CsPbI_3$ NCs solar cell was reported with an efficiency of around 10.8%, [41] many works have been published with increased efficiency and different lead perovskites, [48–51] and to date, the highest reported efficiency for perovskite NCs solar cell is 16.6%. [52]

1.5 Lead toxicity

As mentioned beforehand, the highest-performing perovskites in PV devices contain lead as B component, which is considered worldwide a hazardous material. [53,54] The high toxicity of lead [55–57] is the major concern for perovskite solar cells commercialization, together with their low, still continuously improving stability. [58]

Lead is considered a threat for human beings because it has negative effects on the nervous, hematopoietic, reproductive and cardiovascular systems, besides causing renal dysfunction, mainly as consequences of increased oxidative stress. [55] Lead from perovskites might enter the food chain if perovskites get in contact with water or humid air and as a consequence decompose into highly water-soluble lead precursors, which can then be absorbed by plants or ingested by animals. Besides the risks due to the possibility of leakage of perovskites from broken solar cells, the presence of lead in the crystal structure and its very high solubility in water must be considered in the life cycle of perovskite PVs, since hazardous waste disposal would be compulsory rather than landfilling, and this has a much higher cost compared to non-hazardous waste disposal. [59] Alternatively, standardized protocols for their recycling should be established before their introduction into the market, as it was done for CdTe solar cells. [60]

When evaluating the toxicity of a metal or compound, a fundamental factor to consider is the bioavailability, which is a very complex concept that has been defined in many different ways, for instance as an ensemble of processes including the "external bioavailability", which depends on the ability of the metal to be released by the initial compound and its consecutive solubility in water, and the "internal bioavailability" which indicates the ability of the metal to be absorbed and act producing toxicological effects inside defined tissues. [61] Clearly, defining the "absolute bioavailability" for a certain metal is wrong because by definition, this depends on many factors, among them the compound in which the metal is contained when exposed to the environment. For instance, both cadmium and lead are considered toxic, but CdTe, used in solar cells already available in the market, has a much lower solubility in water than PbI_2, the decomposition product of $MAPbI_3$ perovskites when in contact with water, which ensures that, in these conditions, the bioavailability of lead is much higher than that of cadmium. [60] Therefore, it can be misleading to evaluate the toxicity of lead perovskites and of any other metal compounds by looking at data collected for other samples. [62] On the other side, Abate's group carried out an exhaustive study to measure the bioavailability of Pb^{+2} released by $MAPbI_3$ perovskite, where they demonstrated that lead contained in perovskites can enter different plants, and consequently the food

cycle, ten times more effectively than other lead contaminants present in the soil. [63] Moreover, they carried out the same experiment with $MASnI_3$ perovskite and measured that the tin uptake ability by plants in tin perovskite contaminated soil is relatively low, and suggested it as a safer alternative to lead perovskites. However, as previously stressed, the bioavailability and the effect that metals have in the environment are very complex processes to evaluate. Another study demonstrated that SnI_2 in water creates an acidic environment that is more toxic for animals than the one created with the release in water of PbI_2. [57] Finally, carrying out a life cycle assessment methodology, that takes also into account the lower efficiency of tin based perovskite solar cells in comparison with the lead counterpart, other disadvantages emerge, such as the higher cost of tin or its restricted primary production in countries with high political risks. [64] On balance, lead in perovskite solar cells is a real threat for the environment and for human being health and Sn^{+2} perovskites are not a straightforward solution to this problem, even considering that their solar cells reached 15% efficiency, thus being the most efficient lead-free perovskite solar cells so far. [65] By looking at the periodic table, germanium, which is in the same group as tin and lead, has been considered as another candidate to replace lead. However, its higher tendency to undergo oxidation compared to tin and lead motivated part of the scientific community to move their attention towards different alternatives.

1.6 Alternative abundant elements and new perovskite-inspired structures

The search for alternative abundant and non-toxic elements that can replace lead in the perovskite structure and produce a perovskite with suitable properties for PV applications has been the interest of many computational and experimental studies over the last few years. [56, 66–71]

Instead of focusing only on chemical substitution, which limits the metal candidates to those that have a stable +2 oxidation state, dimensional modification of the archetypal perovskite cubic structure was used to design novel perovskite-inspired structures in which elements with oxidation states +1, +3 or +4 can be inserted. Even though computational works help a lot the scientific advances in this field by calculating the bandgaps and optoelectronic properties of new structures, experiments are the only way to verify if the candidate material is stable in air, condition that is commonly not computed or hard to correctly predict, as it happened for the case of $Cs_2InBiBr_6$, which was claimed to be an ideal candidate for replacing lead perovskites in solar cells, but that demonstrated to be highly difficult to synthesize because of the high instability

Table 1.1: Photovoltaic parameters of the best performing lead-free perovskite solar cells, excluding Sn^{+2} and Ge^{+2} perovskite solar cells. Data taken from [74–81]

Perovskites	Device Structure	Jsc (mA cm^{-2})	Voc (V)	FF	PCE (%)	Methods
$Cs_2AgBiBr_6$	FTO/c-TiO_2/$Cs_2AgBiBr_6$ FREA-Y6/PBDB-T/MoO_x/Ag	3.34	1.278	77.50	3.31	Spin coating
H_2-treated-$Cs_2AgBiBr_6$	ITO/SnO_2/$Cs_2AgBiBr_6$/spiro-OMeTAD/Au	11.40	0.92	60.93	6.37	Spin coating + H_2 plasma
Cs_3BiI_9	FTO/c-TiO_2/Cs_3BiI_9/CuI/Au	5.78	0.86	64.38	3.2	Spin coating
$MA_3Bi_2I_9$	FTO/c-TiO_2/m-TiO_2/$MA_3Bi_2I_9$/P3HT/Au	4.02	1.01	78	3.17	Vapor-based
(heterojunction) $Cs_3Bi_2I_9$-$Ag_3Bi_2I_9$	FTO/c-TiO_2/m-TiO_2/$Cs_3Bi_2I_9$-$Ag_3Bi_2I_9$ BHJ/PDBD-T/Au	7.65	0.78	60	3.59	Spin coating
$MASbSI_2$	FTO/BL/m-TiO_2/$MASbSI_2$/PCPD/TBT/PEDOT:PSS/Au	8.12	0.65	58	3.08	Spin coating
(N-Etpy)$SbBr_6$	ITO/c-ITO_2/(N-Etpy)$SbBr_6$/P3ht/Au	5.10	1.29	58	3.80	Spin coating
Cs_2TiBr_6	FTO/TiO_2-C60/Cs_2TiBr_6/P3HT/Au	5.69	1.02	56.4	3.3	Vapor-based

of In^{+1} in air. [72, 73]

Nowadays, the lead-free perovskites that achieved the highest power conversion efficiencies (PCE) in solar cells, not considering Sn^{+2}- and Ge^{+2}- based perovskites, contain silver and bismuth, [74, 75] only bismuth combined with cesium, [76] with methylammonium [77] or in a two perovskites heterojunction, [78] antimony [79,80,82] and titanium. [81] Table 1.1 summarizes the photovoltaic parameters reported for the record solar cells together with the method used to prepare the perovskite film. We did not include in the table Cs_2SnI_6, because its record efficiency is lower than 1%. [83] However, Sn^{+4}, contrary to Sn^{+2}, demonstrated to be toxicologically inactive [58] and therefore a good candidate for lead replacement. Table 1.1 indicates that the PCE difference between all these record solar cells is not very large, but stays between 3% and 6%.

Considering the abundance of metals in the hearth's crust, represented in Figure 1.3, and comparing the life cycle assessment of Ag, Bi, Sb and Ti, we considered titanium based-perovskites to be the most interesting candidate, because of the abundance and the low impact of titanium on the environment and human health. [85, 86]

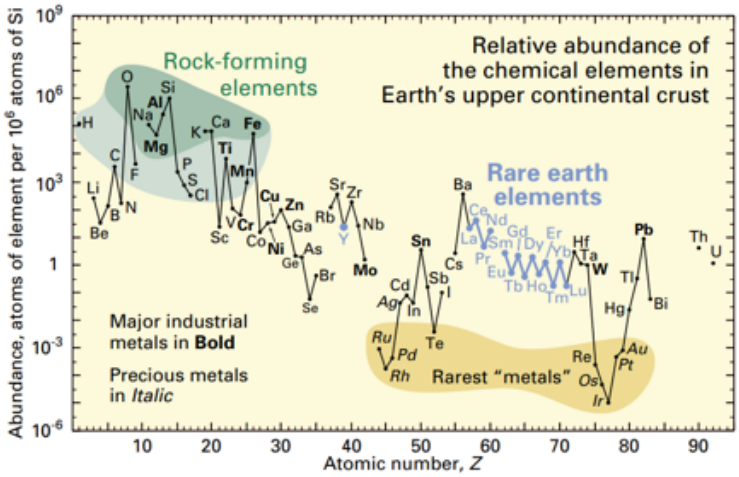

Figure 1.3: Abundance (atom fraction) of the chemical elements in Earth's upper continental crust as a function of atomic number. Figure taken from [84]

1.7 Thesis objective and outline

The solution synthesis of novel environmentally friendly perovskites with PV applications in mind is the core of this thesis. We selected Cs_2TiBr_6 as target material because titanium is an ideal abundant and non-toxic element that might replace lead in perovskites. We chose a solution method as mean to synthesize the material because solution methods do not require high temperatures or high pressures so are less costly, suitable for large-scale production. We selected the colloidal synthesis as synthetic method because, among the different synthesis attempts, it was the only solution method that produced a pure perovskite without any byproduct and also motivated by the fact that perovskite NCs demonstrated to have some superior properties compared to bulk. Finally, we considered the tin analogue because Sn^{+4} and Ti^{+4} have similar atomic radii, ideal condition to mix them in the same structure, Sn^{+4} is toxicologically inactive and tin is relatively abundant in the earth's crust.

Chapter 2 is meant to be an introduction about the crystal structure and the electronic structure of vacancy-ordered double perovskites in comparison with the archetypal ABX_3 cubic structure, and an introduction to the colloidal synthesis principles and the state of the art of the colloidal methods used to prepare perovskite NCs. At the same time, this chapter reports the results of a paper written in collaboration with Sean R. Kavanagh, Dr. Christopher N. Savory, Prof. Aron Walsh and Prof. David O. Scanlon, from the University College London and from the Imperial College London. In this paper, by comparing the computational results with the experimental ones, we claim the need to include van der Waals dispersion interactions when modelling 0D A_2BX_6

systems in order to obtain accurate crystal and electronic structure predictions. The correctness of the computational analysis was confirmed by comparing the calculated absorption spectra with the experimental ones, obtained from the optical measurements of colloidal Cs_2SnX_6 and Cs_2TiX_6 (X = Cl, Br and I) nanocrystal solutions. Finally, we report the colloidal synthesis and the characterization of Cs_2SnCl_6 and Cs_2TiCl_6 NC solutions.

The synthesis of $Cs_2TiBr_{6-x}I_x$ NCs is described in detail in **Chapter 3**. We developed a novel colloidal synthesis to prepare pure and mixed halide titanium perovskites with bandgap tunable from 2.3 eV to 1.2 eV. We characterized the materials with morphological, structural, chemical and optical measurements. Finally, we observed that all these perovskites suffer from high instability in air. Therefore, the next objective of this research was to find a way to stabilize them.

Motivated by the computational results that proved tin perovskites are more thermodinamically stable against oxidation compared with titanium perovskites, we attempted the syntheses of mixed titanium tin perovskite NCs. In **Chapter 4** we show that by partially or completely replacing the titanium with tin, with some adjustments in the synthetic parameters, it is possible to prepare Cs_2SnI_6 and mixed tin titanium $Cs_2Ti_{1-x}Sn_xI_6$ perovskite NCs. For pure Cs_2SnI_6 we studied the influence that different synthetic parameters plays in the purity of the final material and in the NCs' shape. For all the mixtures we carried out a complete characterization since it is the first time that these perovskites are synthesized. We observed that pure tin perovskites are stable in air, while the degradation of mixed tin/titanium perovskites in air is slower than what observed for pure titanium perovskites.

Finally, **Chapter 5** describes an alternative way to stabilize Cs_2TiBr_6 NCs against decomposition in air, by treating the surface of the NCs with tin molecules. We observed a substantial increase in stability, which would finally allow the fabrication of devices with this perovskite.

2

Perovskites: Materials' structure and NCs synthesis

2.1 Crystal structure

2.1.1 ABX_3 perovskites

The term "perovskite" refers to all the materials that possess the same crystal structure as calcium titanate, with chemical formula $CaTiO_3$, which is a mineral that was discovered in 1839 in the Ural mountains and named after the Russian mineralogist Lev Perovski. Their general formula is ABX_3, where A and B are cations, usually with oxidation state +1 and +2 respectively, and X is an anion, most frequently with oxidation state -1. Figure 2.1 illustrates the archetypal cubic crystal structure in which the X components are arranged around the B element forming a corner-sharing octahedral inorganic framework with BX_6 units, while the A component fills the vacancy between the octahedra.

The most studied perovskites for PV applications are those containing Pb^{+2} as B component, any halide (I^-, Br^- or Cl^-) as X component and Cs^{+1} or an organic

cation, such as methylammonium (MA) or formamidinium (FA), as A component. Depending on the size and the nature of the components, the cubic structure can distort to tetragonal and orthorhombic structures at different temperatures, so that, for instance, $MAPbCl_3$ and $MAPbBr_3$ are cubic at room temperature while $MAPbI_3$ is tetragonal. [87]

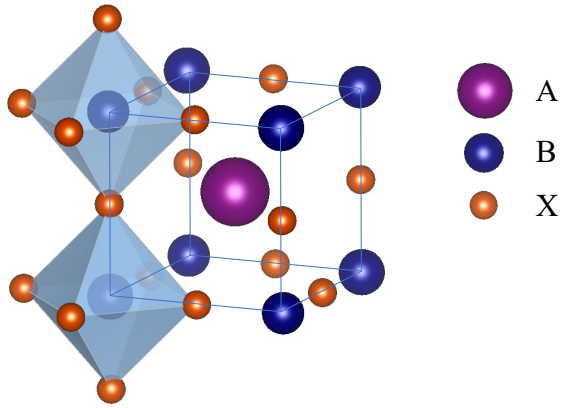

Figure 2.1: Archetypal crystal structure of ABX_3

More importantly, the elements that form the perovskite determine all its chemical and physical properties, giving a huge range of possibilities for the development of novel materials with optimal properties for different applications. For this reason, in the last years, the formability of new perovskites, i.e. the possibility that the combination of 3 components, atoms or molecules, gives rise to a crystal with the perovskite structure, has been the subject of extensive research [88, 89] and has brought to the definition of two important parameters that can predict with good accuracy whether the combination can form a perovskite cubic structure or not. These two factors are the Goldschmidt tolerance factor and the octahedral factor. The Goldschmidt tolerance factor, α, is defined as

$$\alpha = \frac{r_A + r_X}{\sqrt{2}(r_B + r_X)}$$

where r_i is the ionic radius of each component. The optimal α value for cubic perovskite structure is set to be between 0.9 and 1, [90] even though, as said above, this is not a sufficient condition for the formation of the perovskite. On the other hand, the octahedral factor is related only to the octahedra and is equal to the ratio of the B

radius over the X radius, as shown by the equation,

$$\mu = \frac{r_B}{r_X}$$

and its optimal values are predicted to be between 0.414 and 0.732, according to a formability model obtained from an empirical map based on 186 experimental structures. [91]

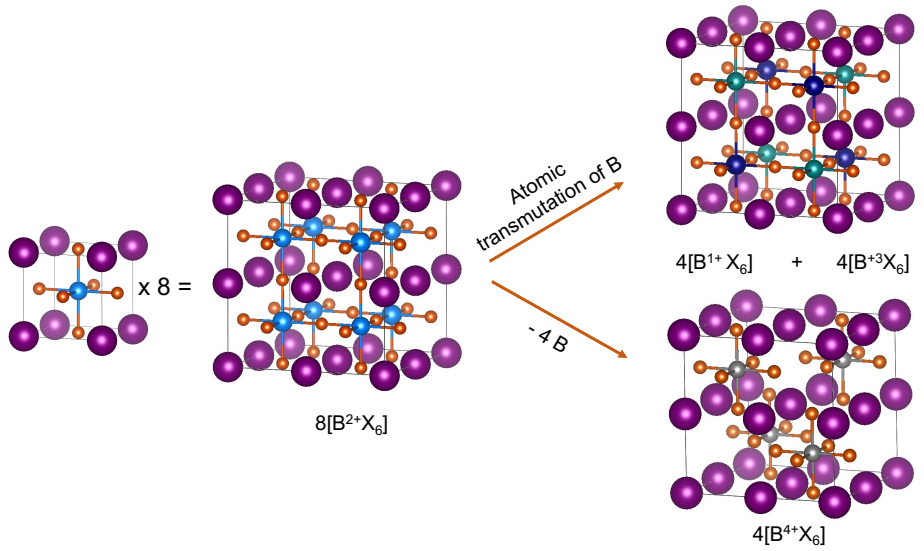

Figure 2.2: Crystal structure of double perovskite (on the top right) and vacancy-ordered double perovskite (on the bottom right), obtained by atomic transmutation or removal of half of B cation, respectively, from the initial archetypal cubic perovskite structure

2.1.2 Double perovskites

The deformation of the archetypal ABX_3 perovskite cubic structure gives rise to several novel structures where other elements can be inserted, some of them showing interesting properties. Among those structures, there are the $A_2BB'X_6$ double perovskites, [72, 92–95] obtained by atomic transmutation of B^{+2} into B^{+1} and B^{+3}, the $A_3B_2X_9$ vacancy-ordered perovskites, [96–98] in which a trivalent B cation is combined with a 1/3 vacancy of the B-site to satisfy neutrality, as well as the A_2BX_6 vacancy-ordered double perovskites, [99–104] which are obtained by the removal of half the B cations in the archetypal perovskite structure, and the use of tetravalent cations instead in

order to balance the charges. Figure 2.2 illustrates how to obtain the double perovskite structure and the vacancy-ordered double perovskite structure, both with space group $Fm\bar{3}m$, from the archetypal cubic ABX_3 perovskite crystal structure, with $Pm\bar{3}m$ space group.

2.1.3 Sn- and Ti- vacancy-ordered double perovskites

Since tin and titanium vacancy-ordered double perovskites are the focus of this thesis, we investigated computationally their crystal and electronic structures. This section collects the main findings regarding the crystal structure.

Table 2.1: Calculated cubic lattice parameters for Cs_2BX_6 (B = Sn, Ti; X = Cl, Br, I) using hybrid DFT including spin-orbit coupling (HSE06+SOC), with and without explicit inclusion of vdW dispersion interactions (D3 correction). Lattice parameter errors (Δa) given with respect to experimental values[a]

	Cs_2SnCl_6	Cs_2SnBr_6	Cs_2SnI_6	Cs_2TiCl_6	Cs_2TiBr_6	Cs_2TiI_6
a_{HSE06}	10.65 Å	11.15 Å	11.95 Å	10.51 Å	10.99 Å	11.76 Å
Δa_{HSE06}	2.8%	3.5%	2.7%	2.6%	2.9%	2.3%
$a_{HSE06+D3}$	10.32 Å	10.78 Å	11.54 Å	10.18 Å	10.62 Å	11.32 Å
$\Delta a_{HSE06+D3}$	- 0.4%	0.1%	-0.9%	-0.6%	-0.6%	-1.5%
a_{Exp}	10.36 Å	10.77 Å	11.64 Å	10.24 Å	10.68 Å	11.5 Å

[a] Experimental values taken from Refs: Cs_2SnCl_6, [105, 106] Cs_2SnBr_6, [106] Cs_2SnI_6, [105, 107–110] Cs_2TiCl_6, [111, 112] Cs_2TiBr_6, [111–113] Cs_2TiI_6, [104] matching with the measured values

A crucial difference between the archetypal perovskite structure and the vacancy-ordered double perovskite structure is the lack of corner-sharing BX_6 octahedra caused by the halving of B component. Consequently, the structure is comprised of isolated octahedra and thus an effective zero-dimensional (0D) framework, with this dramatic reduction in connectivity being a key factor in the properties of this family of materials. Indeed, this change in the connectivity results in the crystal having a "molecular salt" behavior, in the sense that the interactions between the isolated octahedra have similar characteristics to those occurring in molecules, with van der Waals (vdW) forces and London dispersions taking a more important role than in the archetypal cubic ABX_3 structure. This idea is confirmed by the fact that when calculating the lattice parameters upon inclusion of dispersion corrections, the calculated values match the experimental ones with errors $< 1\%$, while when using geometry optimization without including vdW forces the lattice parameters are overestimated by around 3% (Table

2.1). When dispersion corrections are considered, the calculated lattice parameters are smaller and closer to the experimental ones, which indicates that these additional forces cause a shrinking of the structure.

2.2 Electronic structure

2.2.1 ABX_3 perovskites

The success of ABX_3 perovskites in solar cell devices is due to their optimal optoelectronic properties, such as the bandgap in the optimal range for light absorption and the high absorption coefficients, [114] carrier mobilities [115] and diffusion length. [116] All these properties are determined by their electronic structures at the band edges, which have been investigated, by means of computational techniques, and whose main features are summarized below.

- The valence band and the conduction band of ABX_3 perovskites are generated by the interaction of the B and X components, while the A component only influences the bandgap by dictating the spacing and tilting angle of the corner-sharing BX_6 octahedra. [117–119] In particular, the valence band is generated by the anti-bonding interaction of B ns orbitals (for Pb^{+2}, 6s) with X np orbitals, where n depends on the nature of B and X. On the other side, the conduction band is formed by the empty B np orbitals (for Pb^{+2}, 6p) and only in small portion by the X ns orbitals. [120, 121]

- By increasing the electronegativity of the halide X component, going up in the periodic table from iodide to chloride, the bandgap increases (for instance, for $MAPbX_3$, I= 1.55 eV < Br= 2.23 eV < Cl = 3.11 eV). [122, 123] Therefore, the partial or total replacement of the X component with a different halide has become a common method for tuning the bandgap and the emission wavelength. [124]

- The high absorption coefficient of perovskites, in the order of 10^5 cm^{-1}, is due to a direct and parity-allowed transition [114] at the band edges.

- The value of the calculated hole and electron effective masses for $MAPbX_3$ are below 0.34 and 0.32, [123] respectively, while for $CsSnX_3$ are below 0.14 and 0.8. [120] In both cases, these values are small and have been ascribed to the strong dispersion of both bands in reciprocal space, which is consistent with the reports of bipolar electrical conductivity. [107]

- The value of the exciton binding energy for $MAPbI_3$ has been reported between 20 and 50 meV, that is comparable with the thermal energy at RT (κ_BT= 26

meV), [125, 126] which indicates that the excitonic nature of the material does not limit charge separation.

The electronic configuration of Pb^{+2}, which seems to be at the origin of perovskite's success, is

Pb^{+2} = [Xe] $6s^2$ $6p^0$

The filled s orbitals make the material highly polarizable, which leads to large dielectric constants and good screening of charge defects. The empty p orbitals of Pb^{+2} produce a high density of states in the conduction band where the electrons can be excited to, which is going to increase the absorption coefficient.

The same electron configuration is present in all the metals in the same group of the periodic table as Pb, namely Sn and Ge, which indeed have been considered as alternative elements for lead-free perovskites. However, they both have shallower s orbitals than Pb, which makes the ns^2 electrons more ionizable, so that they both show more instability in air due to their propensity to oxidize in the +4 state.

2.2.2 Sn- and Ti- vacancy-ordered double perovskites

As observed for conventional perovskites, also for vacancy-ordered double perovskites the electronic structure at the band edges depends directly on the B and X components, as will be described in this section. However, Sn- and Ti-based vacancy-ordered perovskites present a qualitatively different electronic behavior due to the different electron configurations of atomic titanium and tin. For this reason, a brief description of the main differences between Sn and Ti electron configurations is provided before moving to the analysis of the electronic band structures and absorption spectra for Cs_2TiX_6 and Cs_2SnX_6 perovskites' families.

Sn and Ti electron configuration Referring again to the periodic table, while Sn belongs to group 14^{th} in the p bloc, namely the bloc in which the p orbitals are getting filled, Ti is found in group 4^{th} in the bloc of the transition metals, which all have d orbitals that are not completely filled and consequently play a direct role in their reactivity. The electron configurations of the two metals are

Ti= [Ar] $3d^2$ $4s^2$

Sn= [Kr] $4d^{10}$ $5s^2$ $5p^2$

while when they are in oxidation state +4, the electron configuration becomes:

Ti^{+4}= [Ar] $3d^0$ $4s^0$

Sn^{+4}= [Kr] $4d^{10}$ $5s^0$ $5p^0$

This means that while Sn^{+4} will contribute to the band edges of the perovskite with its p and s orbitals, because its d orbitals are filled, Ti^{+4} will involve its s and d orbitals in the bonding to the halide anions. The crystal field theory describes what happens to the d orbitals of a transition metal when they are perturbated by the interaction with a general "ligand" as depicted in Figure 2.3. Briefly, when examining a metal ion that does not interact with any compound, its d orbitals have all the same energy. However, when six "ligands" approach the metal in an octahedral geometry, as for TiX_6^{-2}, the d orbitals will be perturbated to a different extent, because they all have different symmetries and point to different directions. Those ones that point directly to the direction of the ligands, namely dz^2 and dx^2-y^2, will be excited to higher states, being repelled by the electrons of the ligands, while the others will be stabilized. This behavior is known as crystal field splitting.

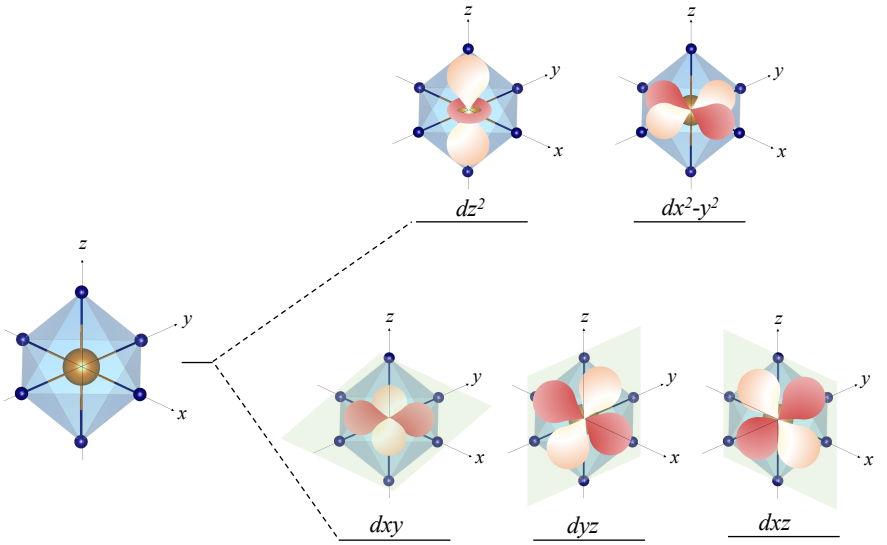

Figure 2.3: d orbitals splitting according to crystal field theory

Cs_2SnX_6 and Cs_2TiX_6 electronic structures. Figure 2.4 shows the electronic band structures of Cs_2TiI_6 (a) and Cs_2SnI_6 (b) calculated using hybrid DFT including spin-orbit coupling (HSE6+SOC). For the Cs_2TiX_6 perovskites, as predicted by the crystal field theory, the dxy, dxz and dyz orbitals have a lower energy than the dz^2 and dx^2-y^2 ones and interact with the X p orbitals making the conduction band minimum with t^*_{2g} symmetry, while dz^2 and dx^2-y^2 orbitals have higher energy above the band edge

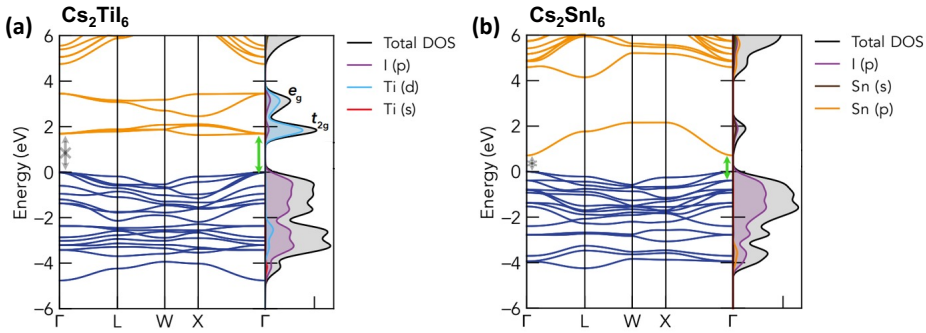

Figure 2.4: Electronic band structure of (a) Cs_2TiI_6 and (b) Cs_2SnI_6 calculated with hybrid DFT including spin-orbit coupling (HSE6+SOC), alongside a vertical plot of the orbital-projected electronic density of states. Fade grey and green arrows indicate the lowest-energy symmetry-forbidden and allowed electronic transition, respectively. Valence band in blue, conduction band in orange, and valence band maximum (VBM) set to 0 eV. Ti d conduction bands are labeled with their crystal field orbital symmetries

and symmetry e^*_g. On the other hand, the valence band maximum is occupied by the non-bonding X p states with t_{2g} symmetry. Due to symmetrical reasons, the transition from the VBM to the CBM is forbidden, because these two levels have the same g, i.e. *gerade*, symmetry, so that the first allowed transition that gives rise to the apparent optical bandgap is the indirect transition from the second-highest valence band at Γ to the CBM at X. However, the direct/indirect gap energy difference is around 0.05 eV for all the Cs_2TiX_6 perovskites according to HSE06+SOC calculations.

With regard to Cs_2SnI_6, the d states are fully occupied and are not involved in the formation of the bands close to the bandgap, so that the conduction band maximum is formed by the interaction between Sn s orbitals and X p orbitals (with symmetry a^*_{1g}) and the VBM is formed by X p non-bonding orbitals (with symmetry t_{2g}). As for Cs_2TiI_6, the first transition is parity forbidden but the transition from the second-highest valence band to the CBM is direct.

The fact that B^{+4} is fully-oxidized means in both cases that the valence band of Cs_2BX_6 is made of non-bonding p orbitals, localized in X, which makes the band less dispersive and thus it yields heavier hole masses, aiding carrier localization, compared to conventional perovskites and other perovskite-inspired materials, whose valence band has both B and X contributions. Interestingly, since Ti is smaller than Sn, the M-X bond length is reduced (for instance, 2.73 Å vs 2.85 Å for the Cs_2BI_6 perovskites), so that the Ti orbitals interact more with the X p orbitals, making the bands more dispersed, and therefore the hole effective masses of Ti perovskites lighter than those of Sn perovskites, as listed in Table 2.2.

Table 2.2: Calculated direct (E_g, Direct) and 'optical' band gaps (E_g, Optical)[a], effective masses (m^*_x)[b], high-frequency dielectric constants (ϵ_∞) and Wannier model exciton binding energies (E_{ex}, Wannier) for Cs_2BX_6 (B = Sn, Ti; X = Cl, Br, I) using hybrid DFT including spin-orbit coupling (HSE06+SOC). Comparison given to experimentally-reported band gap ranges[c]

	Cs_2SnCl_6	**Cs_2SnBr_6**	**Cs_2SnI_6**	**Cs_2TiCl_6**	**Cs_2TiBr_6**	**Cs_2TiI_6**
$E_{g,\ Direct}$	4.1 eV	2.4 eV	0.7 eV	3.7 eV	2.8 eV	1.7 eV
$E_{g,\ Optical}$	4.5 eV	2.9 eV	1.2 eV	4.0 eV	3.0 eV	1.9 eV
$E_{g,\ Exp}$	4.4-4.9 eV	2.7-3.3 eV	1.25-1.3 eV	2.8-3.4 eV	1.8-2.3 eV	1.0-1.2 eV
m^*_e	0.55 m_0	0.38 m_0	0.26 m_0	3.5 m_0	2.7 m_0	1.8 m_0
m^*_h	2.2 m_0	1.3 m_0	0.78 m_0	2.2 m_0	0.90 m_0	0.55 m_0
ε_∞	2.86	3.37	4.54	3.26	3.84	5.08
$E_{ex,\ Wannier}$	0.73 eV	0.35 eV	0.13 eV	2.23 eV	0.62 eV	0.22 eV

[a] "Optical band gaps" determined from Tauc fits of the calculated absorption, assuming direct bandgaps

[b] m^*_x are computed from the harmonic mean over directions and light/heavy bands for the effective masses. Values greater than 1 are given to 1 decimal place

[c] Experimental band gap values taken from Refs: Cs_2SnCl_6, [105, 106, 127, 128] Cs_2SnBr_6, [106, 108, 127–129] Cs_2SnI_6, [99, 105, 106, 108, 127, 130, 131] Cs_2TiCl_6, [111, 112] Cs_2TiBr_6, [81, 104, 112, 113, 132–134] Cs_2TiI_6 [104, 132]

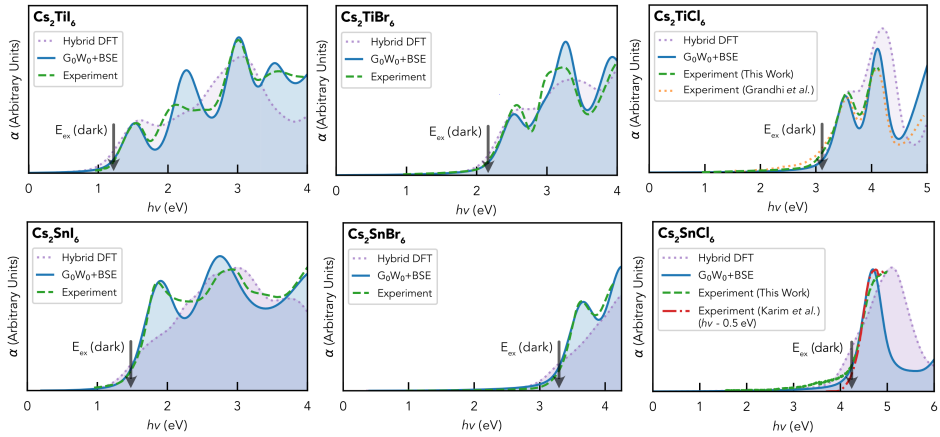

Figure 2.5: Absorption spectra of Cs_2TiX_6 and Cs_2SnX_6, calculated with both hybrid DFT and the G_0W_0 + BSE method, alongside the experimental data from UV-Vis spectroscopy. Calculated curves have been rigidly shifted to match the experimental absorption onset

Table 2.2 also collects the computed data for the electron effective masses, the high-frequency dielectric constants, the Wannier-Mott excitonic binding energy and the values of the experimental and calculated bandgaps. Regarding the electron effective masses, they are lower for Cs_2SnX_6 than for Cs_2TiX_6 because, as observable in Figure 2.4, the CB is due to a strong mixing and delocalization of the Sn s and X p states, while in Cs_2TiX_6 the conduction band has flat bands due to the weak Ti d – X p mixing and localized, isolated Ti d states.

Regarding the values of the bandgaps, we observed that they follow the common trend E_g Cl > Br > I, observed in cubic ABX_3 perovskites.

The values tabulated in Table 2.2 related to the Wannier-Mott exciton binding energies are higher for titanium perovskites than for tin perovskites. This fact, in addition to the highly-localized d orbitals of titanium, suggests that this class of perovskites most probably have strongly-bound excitons. This means that the electron-hole interactions play a fundamental role in the electronic structure of these perovskites and should be considered in the computational methods, which is done by including these interactions via the Bethe-Salpeter equation (BSE). The hypothesis of strong excitons was confirmed by comparing the experimental absorption spectra obtained for all the Sn and Ti perovskites with the calculated spectra using DFT and G_0W_0 + BSE methods, as shown in Figure 2.5. As expected, all the experimental absorption spectra are in better agreement with the G_0W_0 + BSE calculated spectra than with the DFT calculations.

The low-energy peaks in the absorption spectra of Cs_2TiX_6 are excitonic and are, as

expected, due to the transition from the second- and from the third-highest valence bands to the CBM, because the transition from the VBM is forbidden. The excitons responsible for these peaks are called "charge-transfer" Frenkel excitons, with the electron in Ti t_{2g} d orbitals and the hole around the p orbitals of X. This form of exciton is most commonly witnessed in organic and molecular crystals, such as other $3d^0$ transition metal halides. Interestingly, the experimental spectra of $TiBr_6^{-2}$ and $TiCl_6^{-2}$ salts reported by Brisdon et al. [135] closely resemble the theoretical and experimental results for Cs_2TiBr_6 and Cs_2TiCl_6, evidencing the conclusion of molecular crystal behavior. Regarding the Cs_2SnX_6, the peaks are also excitonic but only weakly-bond excitons are calculated.

The last interesting difference between titanium and tin perovskites' absorption spectra is that the bandgap increase in the tin family going from iodide to chloride is greater than the one observed in the titanium family. This can be ascribed again to the different electron configurations of Sn and Ti and their different way of contributing to the band edges of the perovskite.

The experimental spectra depicted in Figure 2.5 are those of the colloidal solutions that were prepared following the procedures reported in this thesis. The colloidal syntheses of Cs_2SnCl_6 and Cs_2TiCl_6 NCs are described in section 4 of this chapter. The syntheses of Cs_2TiBr_6 and Cs_2TiI_6 NCs are reported in Chapter 3, while the syntheses of Cs_2SnI_6 and Cs_2SnBr_6 NCs are described in Chapter 4 and Chapter 5, respectively.

2.2.3 Other double perovskites

Similar behaviour as the one observed in Ti^{+4} perovskites is expected for all the A_2BX_6 compounds with isoelectronic (d0) B^{+4} cations. Indeed, strong excitonic interactions have been reported in Cs_2ZrX_6 [136] and Cs_2HfCl_6 [137,138] perovskites. Moreover, also the $A_2BB'X_6$ double perovskites showed this kind of excitonic behaviour, [139–141] because despite their greater structural connectivity, they exhibit a low "effective" electronic dimensionality due to orbital mismatch between the B-site cations. [142,143] Also, it was observed for Cs_2AgBiX_6 that the bandgap is indirect and that the first direct parity-allowed transition is at more than 0.5 eV above it, which causes a relatively low absorption. [142]

2.3 Solution synthesis of perovskite nanocrystals

2.3.1 Introduction

One of the key attractions of perovskites is that they can be easily prepared as films using different methods, from solution-based to vapor-phase, involving either one step or two steps of precursor's deposition. The synthesis method plays a primary role in the final properties and morphology of the perovskite film, so that for each perovskite and for different application is key to determine the optimal synthetic parameters to achieve the best performing material or specific unique properties. In most cases, perovskite films can be prepared starting from their salt components, i.e. AX and BX_2. These can be either deposited by evaporation at low pressure and high temperature, or dissolved in Lewis base solvents, such as dimethylsulfoxide (DMSO) or dimethylformamide (DMF) or a mix of them, and subsequently spin coated on a substrate, which is the so-called "precipitation from solution" method. The morphology of the resultant film depends on many factors, including the precursors, the solvents, the concentration of the solution, the washing and treatment of the substrate in order to modify its surface chemistry, and the spin coating conditions, for instance the speed and time of rotation. Moreover, an additional annealing step can also have an effect on the morphology and properties of the film.

In 2015, perovskites were synthesized for the first time as NCs. [29] From that moment, their outstanding properties as NCs have been documented when applied in several devices, such as solar cells, [144–146] light emitting diodes, [147, 148] photodetectors [149] and lasers. [150] For the synthesis of the perovskites discussed in this thesis, we used the colloidal synthesis, also due to the difficulty found when attempting more direct methods such as the "precipitation from solution" method, as will be commented in the introduction of Chapter 3.

The next sections describe the hot injection method, which is the method used to synthesize the colloidal perovskite NCs, the washing procedure to obtain a pure product after the colloidal synthesis and the state of the art of the hot injection method applied in perovskite NCs synthesis.

2.3.2 Colloidal synthesis

A common method to prepare nanostructured semiconductors is by means of the colloidal synthesis. A colloidal suspension is a mixture in which one substance, in this case the NCs, are dispersed in a continuous phase, usually an organic solvent. For the NCs to remain dispersed throughout the solvent and do not precipitate or aggregate,

they need to be surrounded by the so-called ligands, which are surfactants that lower the surface tension between the two phases of the colloidal solution, thanks to their chemical structure that consists of a hydrophilic head, more polar and that attaches to the surface of the NCs, and a hydrophobic tail, which interacts with the organic solvent. In order for the nanoparticles to be well dispersed into the solvent, many parameters must be optimized, among them the choice of the solvents, of the ligands, the size of the NCs and their concentration.

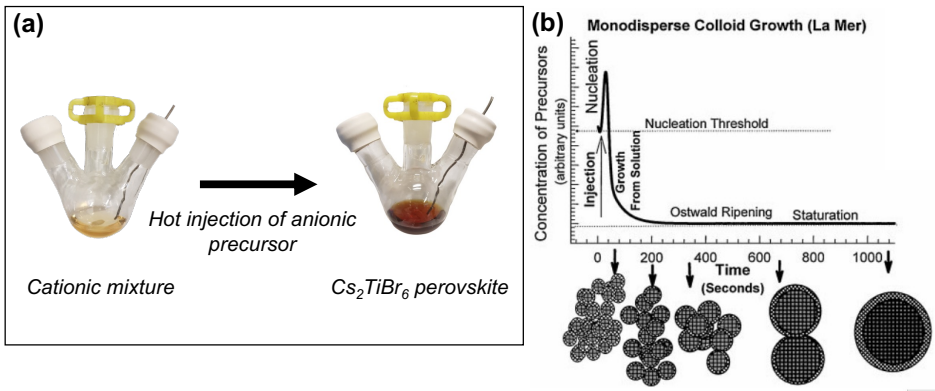

Figure 2.6: (a) Representation of color change after the hot injection of the X precursor. (b) "Cartoon depicting the stages of nucleation and growth for the preparation of monodisperse NCs in the framework of the La Mer model. As NCs grow with time, a size series of NCs may be isolated by periodically removing aliquots from the reaction vessel". Figure b and caption b taken from [151]

The hot injection method is used to prepare NCs with good control over their shape and size, in order to obtain a "monodisperse" solution, [152] and it was first reported by Bawendi et al. in 1993. [35] This kind of reaction is usually carried out under inert atmosphere, in order to avoid any side reaction with water and oxygen present in the air. For this purpose, the synthesis is performed in a Schlenk line, which is a chemistry apparatus connected to an inert gas line and to a vacuum pump, in which vacuum and inert gas atmosphere can be easily interchanged. Three components are essential for the hot-injection synthesis: a high-boiling point solvent, capable of holding high temperatures without evaporating during the synthesis neither under vacuum, the ligands and the precursors, that must be soluble in the high-boiling point solvent. [151]

For perovskites, two of the three precursors are dissolved in the solvent with the ligands, then the solution is heated up and the third precursor is injected at high temperature. After the injection, the solution changes color, indicating that the product has been

synthesized, as shown in Figure 2.6(a) for the synthesis of Cs_2TiBr_6. The reaction is stopped, i.e. quenched, after few seconds to avoid further growth of the NCs, using an ice bath to decrease the temperature or by diluting the solution with the addition of solvent.

The mechanism of the hot-injection reaction has been studied by de La Mer [153] and it consists of three steps: Burst nucleation, diffusion-controlled growth and Ostwald ripening. The fast addition of the third precursor through the hot injection raises the precursors' concentration above the nucleation threshold (scheme in Figure 2.6 (b)), which is the critical concentration above which the nuclei form, where nuclei are very small particles made of few atoms. After the nucleation burst, the number of precursors decreases below the nucleation threshold, so that no more new nuclei form. The diffusion-controlled growth is the step that follows the nucleation step, in which the precursors react directly with the nuclei, enlarging the size of the NCs. A second possible growth mechanism, the so-called "Ostwald-ripening", called after the scientist that described it in 1896, can also occur and it consists in the smaller particles redissolving in solution because of their high surface energy and redepositing on the surface of the bigger NCs.

2.3.3 Washing

After the synthesis, the NCs are washed in order to remove possible byproducts and the excess of ligands. Moreover, this step can be used to narrow down the size distribution of the NCs, by size-selective precipitation. [154] The washing procedure consists in centrifuging the solution obtained from the synthesis in order to separate the nanoparticles, that will precipitate, from the rest of the solution (Scheme in Figure 2.7). If the nanoparticles are stable in the crude solution, it is necessary to add an antisolvent, namely a solvent in which the nanoparticles are not stable. The precipitated nanoparticles are then redispersed in an organic solvent, which for perovskite NCs is usually toluene or octane. The centrifugation is usually carried out more than once, using different centrifugation speeds and antisolvents in order to obtain the purest and most stable solution. Perovskite nanocrystals have been found to be very sensitive to the washing procedure, so that a high centrifugation speed or a strong antisolvent may destroy them or damage their surface. [44, 155]

2.3.4 Hot injection method for perovskites

Several perovskite NCs and quantum dots have been synthesized using the hot-injection method and some works reported the studies of the effects of the synthetic parameters

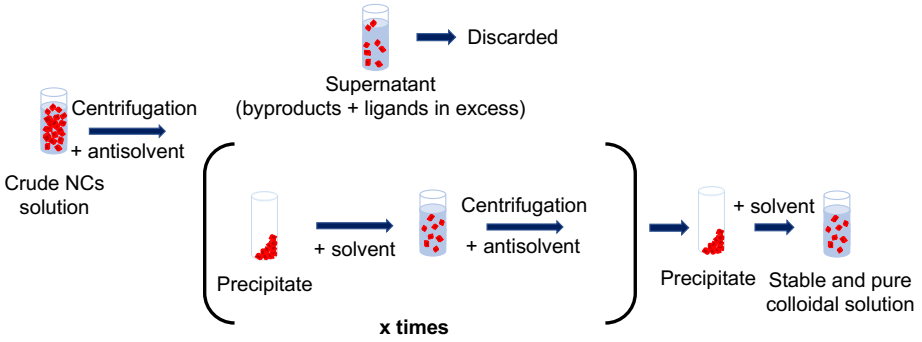

Figure 2.7: Scheme of common washing procedure

on the purity, the size and the shape of the NCs.

In some syntheses, the temperature of injection had an influence on the size of the NCs, with higher temperatures resulting in bigger NCs, [29] while in other cases tuning the temperature affected the shape of the NCs. [156] Other times, the shape of the NCs was controlled by tuning the reaction time, [157] namely the time between the injection of the third reactant and the quenching of the reaction, even though for $CsPbX_3$, it was observed that crystal growth occurs within few seconds after the hot injection. [29]

Other parameters to control are the concentration of precursors, their ratios, since the stoichiometric ratio of the precursors could favor the formation of one or more byproducts, [68] and their reactivity. Initially, the common synthesis, [41, 158–160] developed by Protesescu et al., [29] consisted in injecting cesium oleate at high temperature in a mixture of octadecene, oleic acid, oleylamine and BX_2 salts, which were employed as both B and X precursors. The limitation of this method was that it did not allow to independently tune the B and X amounts, while it was soon observed that regulating the amount of X precursor could lead to improved stability and optical properties of the NCs. [161–163] Later this problem was overcome by the use of A and B organic salts, such as acetate or oleate ones, and the injection of alkylammonium halide salts, such as oleylammonium iodide [164] and octadecylammonium bromide [165] at high temperatures. However, these precursors are not very reactive, so only few perovskites could be synthesized with this method. Finally, Creutz et al. [68] and Imran et al. [166] used trimethylsilyl halide and benzoyl halide precursors, both very reactive chemicals, which paved the way for the synthesis of many novel perovskite NCs.

Finally, it has been demonstrated that the use of different ligands can lead to perovskite nanoparticles with different shapes. [42] In general, the common ligands used in the synthesis of perovskite nanoparticles are oleic acid (OA) and oleylamine (OLAm),

though other combinations of amines and fatty acids are also common. However, their bond to the perovskite surface is highly dynamic, and therefore they easily desorb from the surface of the nanoparticles during the washing procedure, causing NCs aggregation. [167] For cesium lead halide perovskites, it has been shown that zwitterionic molecules, which are molecules that contain both a positively-charged and a negatively-charged functional groups, can stabilize better the nanoparticles thanks to their chelate effect. [168] Figure 2.8 illustrates the most common organic molecules used in perovskite NCs synthesis.

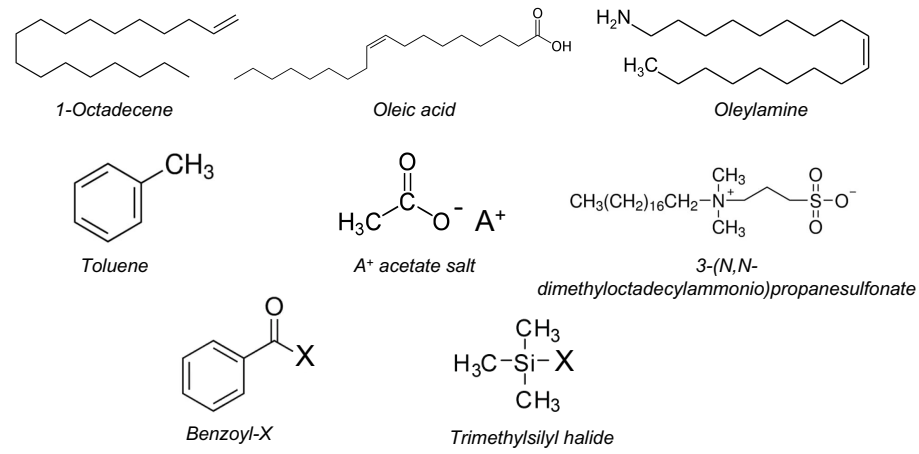

Figure 2.8: Representation of some common molecules used in the colloidal synthesis of perovskite NCs

2.3.5 Deposition of thin films from NCs solution

The preparation of NC thin films for the fabrication of devices consists in depositing the NCs from solution through methods such as spin-coating, while the insulating long-chain ligands must be replaced with short ligands that do not hinder the conductivity. The so-called "ligand exchange" is a process that consists in the replacement of the long chain ligands with smaller ligands, and it can be carried out in solution or when the NCs are already deposited on a substrate. Usually, for perovskites, the second method is the most effective one, as it is very hard to maintain the NCs in solution after the ligand exchange, and a solution that is not well-dispersed will not produce homogenous films. Generally for perovskites, the solid-state ligand exchange is carried out using precursor salts, such as Pb acetate, $Pb(NO_3)_2$, formamidinium iodide (FAI), or sometimes only methylacetate. [41, 48–51]

2.4 Synthesis and characterization of Cs_2SnCl_6 and Cs_2TiCl_6

The synthesis of Cs_2SnX_6 and Cs_2TiX_6, where X= I, Br or Cl, were carried out in order to measure the absorption spectra shown in Figure 2.5. While the iodide and bromide analogue perovskite syntheses are described in the next chapters, Cs_2SnCl_6 and Cs_2TiCl_6 were prepared on purpose for the computational study reported in Section 2.2 and their synthesis and characterization are described here.

Both syntheses were carried out using the hot-injection method. The solvent used in the syntheses was 1-octadecene (ODE), and the ligands OA, for the case of Cs_2TiCl_6, and OA and 3-(N,N-dimethyloctadecylammonio)propanesulfonate (DMOP), which is a zwitterionic bidentate ligand, for the synthesis of Cs_2SnCl_6. In both syntheses trimethylsilyl chloride (TMSCl) was injected at 140°C to a solution of cesium oleate and the B component precursor.

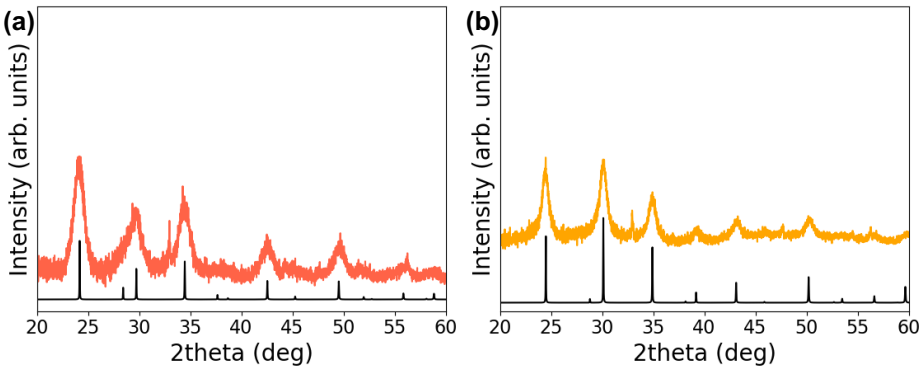

Figure 2.9: XRD patterns of (a) pure Cs_2SnCl_6 prepared with ratio 2:2:9 with the reference pattern and (b) pure Cs_2TiCl_6 prepared with ratio 2:2.5:60 with the reference pattern. The narrow peak at 32.97 degrees originates from the silicon substrate

The synthesis of Cs_2SnCl_6 was carried out using tin acetate as tin precursor. The ratio of precursors used was Cs:Sn:Cl =2:2:9 because when using lower amounts of Cl and Sn precursors the product shown CsCl contamination in the X-Ray Diffraction (XRD) pattern. Figure 2.9(a) shows the XRD pattern of the pure sample. Rietveld refinement yields a lattice parameter of 10.381(6) Å, close to the values found in the literature. [105, 106]

For the synthesis of Cs_2TiCl_6, titanium oleate was used as Ti precursor. The precursors' ratio used was Cs:Ti:Cl =2:2.5:60, because lower amount of chloride precursor did not

lead to the perovskite. From the XRD pattern, shown in Figure 2.9(b), a lattice parameter of 10.253(13) Å was determined from Rietveld refinement, in agreement with reported data in the literature. [111, 112]

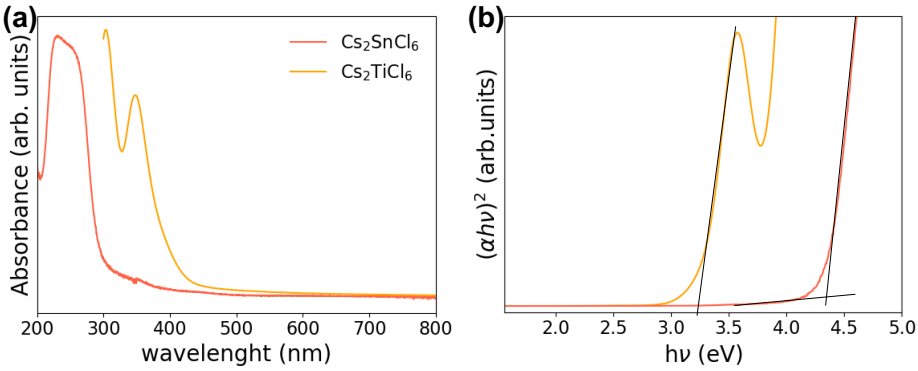

Figure 2.10: (a) Absorption spectra and (b) Tauc plots of Cs_2TiCl_6 and Cs_2SnCl_6 NCs

Interestingly, Cs_2TiCl_6 is the only titanium(IV) perovskite that was found to be stable in air. Indeed, opposite to the bromide and iodide analogues, its XRD pattern could be taken in air instead of using a sample holder filled with nitrogen.

After the perovskites were characterized structurally, the absorption spectra were measured and are shown in Figure 2.10(a). From the Tauc plots, depicted in Figure 2.10(b), a bandgap of 3.25 eV was extracted for Cs_2TiCl_6 and a larger one of 4.4 eV was extracted for Cs_2SnCl_6. Both values are close to those found in the literature. [105, 106, 111, 112]

2.5 Conclusions

In conclusion, it was verified, by comparison of computational with experimental studies, the importance of including vdW dispersion interactions when modelling 0D A_2BX_6 systems in order to obtain accurate crystal and electronic structure predictions. Experimentally, it was demonstrated that Cs_2SnX_6 and Cs_2TiX_6 (where X = Cl, Br and I) NCs can all be prepared using the hot-injection method. In particular, Cs_2SnCl_6 and Cs_2TiCl_6 were prepared as NCs and their characterization was carried out through XRD analysis and absorption measurements. It was observed that an excess of halide precursor is needed to obtain pure products and that the synthesized NCs have lattice parameters close to those reported in the literature and bandgaps of 3.25 eV for

Cs_2TiCl_6 and 4.4 eV for Cs_2SnCl_6. Finally, both chloride perovskites were found to be stable when exposed to air.

3

$Cs_2TiBr_{6-x}I_x$ vacancy-ordered perovskites

3.1 Introduction

Over the last 5 years, vacancy-ordered perovskites containing tin, [101, 157] palladium, [102] tellurium, [103] zirconium [136] and titanium [81, 132] have been synthesized and characterized. Among them, cesium titanium bromide perovskite stands out as a promising candidate for lead-free perovskite solar cells in view of its favourable bandgap for PV applications and its reported solar cell with PCE of 3.3%. [81] To date, Cs_2TiBr_6 perovskite has been synthesized with different methods, none of which is a low temperature and easily scalable solution method that leads to stock solutions suitable for making low-cost thin films for optoelectronic devices. [81, 111, 132] While Cs_2TiBr_6 with a bandgap of 1.8 eV has been grown via vapor deposition at high temperatures, [81] $Cs_2TiBr_{6-x}I_x$ that offer bandgap tunability down to 1.2 eV have only been grown by melt-crystallization at high temperatures [132] yielding crystal powders and preventing their application to devices. A solution method had yet to be reported due to the difficulty in finding a solvent in which both CsBr/CsI and $TiBr_4/TiI_4$ are soluble, since cesium halides dissolve only in highly polar solvents while titanium halides react with them. In this chapter, we present a new approach for the

synthesis of Cs_2TiBr_6 and mixed bromide/iodide $Cs_2TiBr_{6-x}I_x$ NCs, which consists on performing a colloidal synthesis using the hot-injection method. With this method, we were able to synthesize stable solutions of mixed bromide/iodide $Cs_2TiBr_{6-x}I_x$ NCs that can be easily deposited as thin films. The chemical, structural and optical characterization of this class of perovskites is reported together with the study of the influence of synthetic parameters on the purity and shape of the NCs.

3.2 Synthesis and characterization of Cs_2TiBr_6

This section deals with the synthesis and characterization of pure bromide Cs_2TiBr_6. Moreover, the influence of the precursor's ratio, the ligands, and other synthetic parameters such as the reaction temperature and the quenching method on the purity of the final product and on the shape of the NCs was investigated. The second part of this section resumes the effect of these parameters one by one.

3.2.1 Colloidal synthesis

For the synthesis of Cs_2TiBr_6 NCs, cesium acetate and a solution of titanium oleate were loaded in a flask together with OA, DMOP and ODE. After 3 cycles of argon and vacuum to remove water and oxygen inside the flask, the solution was heated at 110 °C and left under vacuum for 30 minutes to dissolve all the powdered precursors. Afterwards, the temperature was increased at 140 °C and bromotrimethylsilane (TMSBr) was swiftly injected under argon. After few seconds the reaction was quenched by diluting the nanocrystals in toluene while lowering the temperature. After the injection, the solution changed color from pale orange to dark red. The optimal precursors' ratio was found to be Cs:Ti:Br = 2:2.5:13.5.

The cations' precursors were cesium acetate and titanium (IV) isopropoxide. The latter is very sensitive to air, which is the reason why it was preferred to use a solution of titanium oleate, prepared by mixing the titanium precursor with a large excess of oleic acid over night at high temperature.

3.2.2 Characterization

Figure 3.1 shows the XRD pattern of the as-synthesized nanoparticles and the simulated XRD pattern of Cs_2TiBr_6, which indicates that the crystal possesses $Fm\bar{3}m$ space group symmetry. Rietveld refinement yields a lattice constant of 10.706(3) Å, very close to the values reported in the literature for bulk Cs_2TiBr_6. [111, 113, 132]

The morphological characterization of Cs_2TiBr_6 perovskite nanoparticles was done by

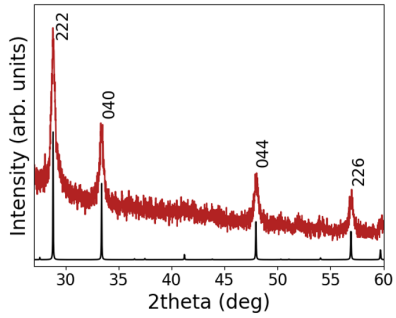

Figure 3.1: XRD pattern of Cs_2TiBr_6 NCs with the corresponding simulated reflections for Cs_2TiBr_6 with the same lattice parameter

carrying out a Transmission Electron Microscopy (TEM) analysis. Figure 3.2 shows that the synthesis produces well-dispersed nanoparticles with a controlled size distribution, with an average diameter of 12.9 nm, a size deviation of ±1.7 nm and symmetrical shape.

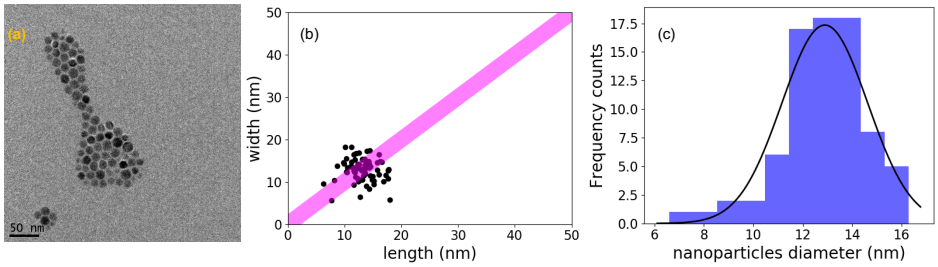

Figure 3.2: (a) TEM image from where the size distribution and symmetry analysis was carried out. (b) Plot of the width vs the length of the nanoparticles, which indicates the nanoparticles are close to the symmetry. (c) Histogram of the NCs diameters, calculated from the area of the NCs, indicating an average NC diameter of 12.9 nm, with a standard deviation of ± 1.7 nm

Figure 3.3 is a High Resolution TEM (HRTEM) image of the same sample from where d-spacings can be extracted through a Fast Fourier Transform (FFT) of the image, represented in the inset of the figure. The d-spacings calculated from the image match those ones obtained considering a lattice parameter of 10.71 Å, inferred from the XRD pattern.

The elemental analysis was conducted using energy-dispersive X-ray spectroscopy (EDS) analysis operated in a scanning transmission electron microscope (STEM) and inductively coupled plasma - optical emission spectroscopy (ICP-OES). STEM-EDS analysis performed on ensembles of NCs detected the presence of Cs, Ti and Br (Figure 3.4), however, this analysis could not be considered quantitative due to the overlapping of

Ti and Cs peaks.

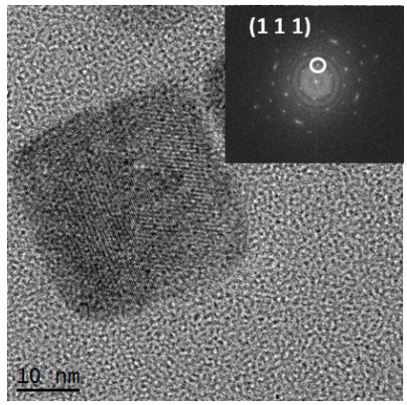

Figure 3.3: HRTEM image of Cs_2TiBr_6 NCs. In the inset, the FFT of the image, from where the d-spacings were extracted

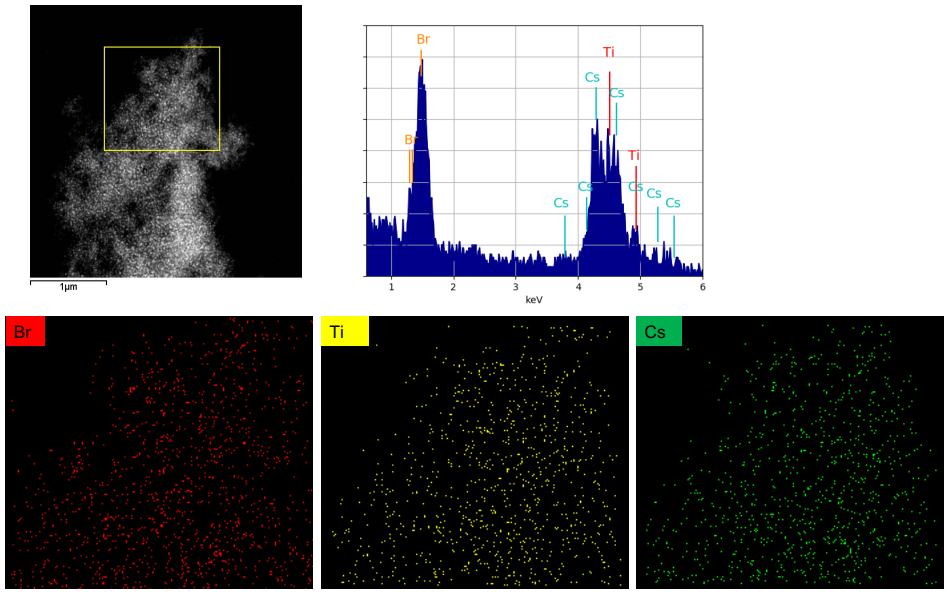

Figure 3.4: High-angle annular dark-field (HAADF) image and STEM-EDS analysis of Cs_2TiBr_6 NCs with the corresponding atomic maps

Therefore, we performed ICP-OES measurements that confirmed the ratio Cs/Ti is very close to 2, i.e. 2.1, as expected from the chemical formula of the perovskite (Table 3.1)).

To investigate the optical properties of the Cs_2TiBr_6 colloidal solution, absorption

and emission of the washed solution were measured and are shown in Figure 3.5(a). Taking into account the quasi-direct bandgap nature calculated for Cs_2TiBr_6, the optical bandgap was extracted from the Tauc plots, considering both direct and indirect bandgaps, and it is equal to 2.3 eV and 2 eV respectively (Figure 3.5 (b) and (c)), around 0.5 eV higher than the values reported for bulk Cs_2TiBr_6. [81, 113, 132] The absorption spectrum has the same shape observed for the bulk material, with two peaks at 390 nm and 483 nm representing two excitonic transitions. The emission peak falls at 580 nm (2.1 eV) and the PLQY, measured at the excitation wavelength of 480 nm using Rhodamine 6G in absolute ethanol as reference, is far below 1%. The large Stokes shift, broad peak and low emission intensity is a result of localized photogenerated bound excitons, as well as strong exciton-phonon coupling, that yield emissive self-trapped exciton (STE) states. The method used to calculate the relative PLQY value is described in Appendix E.

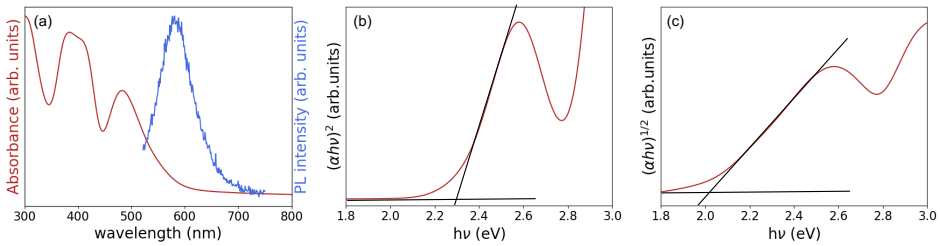

Figure 3.5: (a) Absorption and PL spectra of washed Cs_2TiBr_6 NCs diluted in toluene. (b) Tauc plot of Cs_2TiBr_6, considering direct bandgap and (c) indirect bandgap

3.2.3 Study of the influence of different precursors' ratios

The first and most important parameter to optimize was the precursors' ratio. The influence of this parameter on the purity of the final product was investigated using XRD because it was observed that the absorption spectrum of the product appeared the same regardless of the presence of byproducts. The first attempt was carried out using a precursors' ratio equal to the stoichiometric ratio, which means Cs:Ti:Br = 2:1:6. The solution looked dark red, as supposed for Cs_2TiBr_6, but the XRD pattern showed only CsBr peaks (Figure 3.6).

Therefore, the precursors' ratio was tuned considering that the formation of CsBr was favoured when the ratio of cesium over the other precursors was stoichiometric. Figure 3.7 shows the XRD patterns of the products of different reactions with increasing amounts of titanium and bromide precursors. When using a ratio of 2:2:9, the Cs_2TiBr_6 diffraction peaks appear but the three diffraction peaks coming from CsBr contamination are still visible, while when increasing the amount of bromide precur-

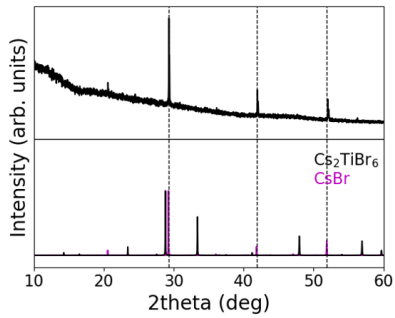

Figure 3.6: XRD pattern of the first attempt to synthesize Cs_2TiBr_6 using a precursors' ratio equal to Cs:Ti:Br = 2:1:6

sor injected into the solution up to a ratio of 2:2.5:13.5, these peaks are not present anymore. Therefore, we set this as standard precursors' ratio for the other parameters' optimization.

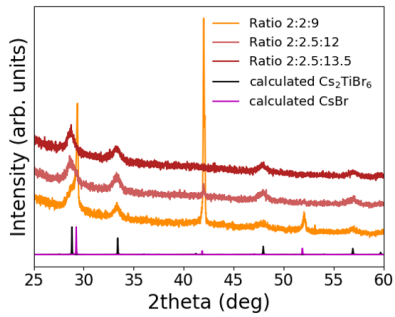

Figure 3.7: XRD patterns of Cs_2TiBr_6 nanocrystals synthesized using three different precursors' ratio (2:2:9, 2:2.5:12, 2:2.5:13.5)

Finally, the XRD of titanium (IV) bromide was also measured to ensure that its diffraction pattern does not overlap with the Cs_2TiBr_6 pattern, so that we could neglect the chance that this possible byproduct was present in the final product (Figure 3.8).

3.2.4 Study of the ligands

The most common ligands used for the colloidal synthesis of perovskite nanocrystals are long-chain organic acids and amines and usually a combination of both is used. However, in this case we noticed that when carrying out the reaction with OA and two commonly used amines, namely oleylamine and octylamine, after the TMSBr injection the solution turned dark red, as expected, but few seconds later it changed again color into milky. Moreover, from XRD measurements, CsBr was detected. Interestingly, the

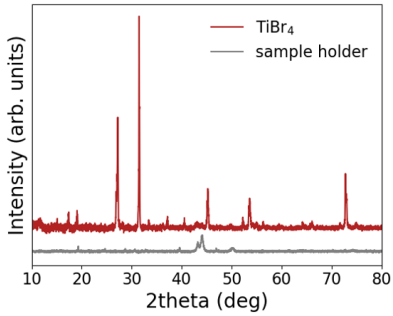

Figure 3.8: XRD pattern of $TiBr_4$ powder, taken using an air-sensitive sample holder to avoid decomposition due to air exposure

production of CsBr as byproduct and the change of color from dark red to milky can be suppressed to a certain extent when the temperature of TMSBr injection is lowered or when the amine ligand is added after the synthesis at room temperature (Figure 3.9).

To understand the reactivity of these amines with Cs_2TiBr_6, we mixed different ligands with a solution of $TiBr_4$ dissolved in toluene, and observed that amines with the lone pair in the nitrogen atom available reacted with $TiBr_4$ producing a white powder, while quaternary amines or organic acids did not produce any change in the color of the $TiBr_4$ solution (Figure 3.10). From these experimental observations, we hypothesized that the strong electrophilic nature of titanium in oxidation state +4 combined with the nucleophilicity of primary amines, could give rise to adducts of amines and $Ti(IV)Br_4$, as already observed in literature for $Ti(IV)Cl_4$. [169]

For this reason, at the beginning only OA was used in the reaction. Later, we added to the reaction DMOP because it made the final solution more colloidally stable and robust during the washing steps.

3-(N,N-Dimethyloctadecylammonio) propanesulfonate belongs to the family of the zwitterionic molecules, which are neutral molecules that contain an equal number of positively- and negatively-charged functional group. In particular, this compound contains a negatively-charged sulfonate group and a positively-charged quaternary aminic group, so that the possible secondary reaction with $TiBr_4$ would be avoided; moreover, both functional groups can act as ligand, thus the overall molecule behaves as a chelating ligand. Indeed, this ligand demonstrated to stabilize perovskite NC solutions better than the common OA/OLam system. [168]

This zwitterionic ligand (DMOP) is used in the synthesis in order to stabilize the nanoparticles during the washing procedure but it does not play a crucial role in controlling the morphology of the nanoparticles. Indeed, the first attempts to synthesize

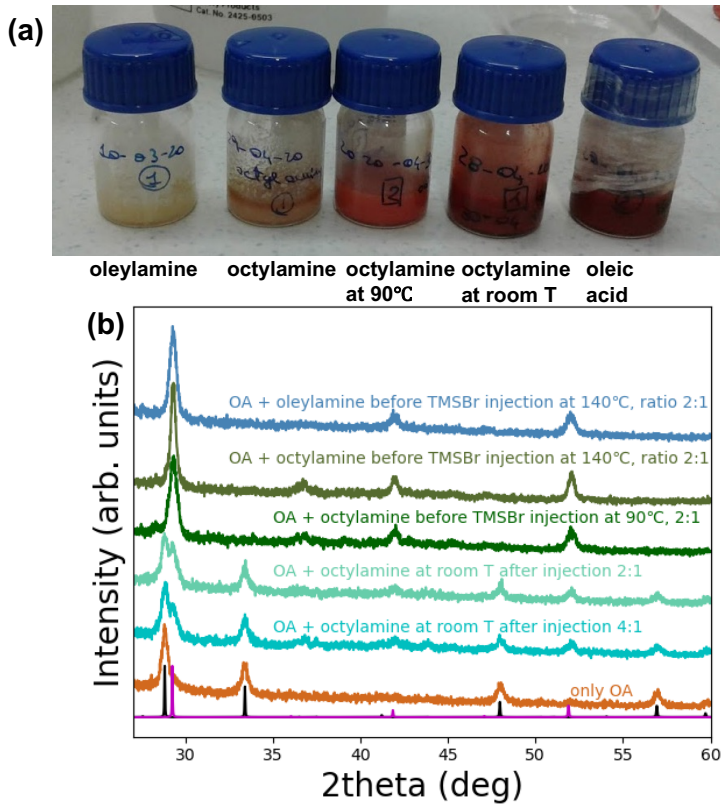

Figure 3.9: Comparison of solutions prepared adding oleylamine and octylamine in different amounts (indicated as ratio oleic acid/amine) and at different temperatures. The black pattern is the Cs_2TiBr_6 reference and the purple one the CsBr reference

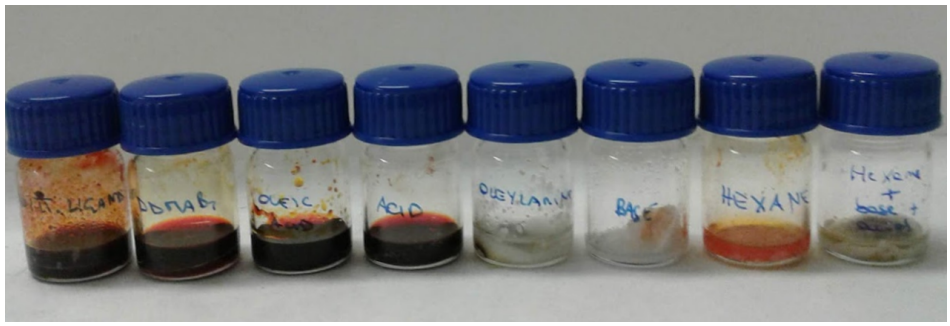

Figure 3.10: Comparison of the effect of adding different ligands into a solution of $TiBr_4$ dissolved in toluene. In order, DMOP, didodecyldimethylammonium bromide, oleic acid, propionic acid, oleylamine, butylamine, hexane and hexane with propionic acid and butylamine

Cs_2TiBr_6 NCs, when only OA was used as ligand, produced very similarly shaped nanoparticles with a homogeneous size distribution (Figure 3.11). However, the as-prepared nanoparticles were very sensitive to any antisolvent used during the washing step. On the contrary, with the use of the zwitterionic ligand the nanoparticles are stabilized so that can be precipitated with acetone and then easily redispersed in toluene.

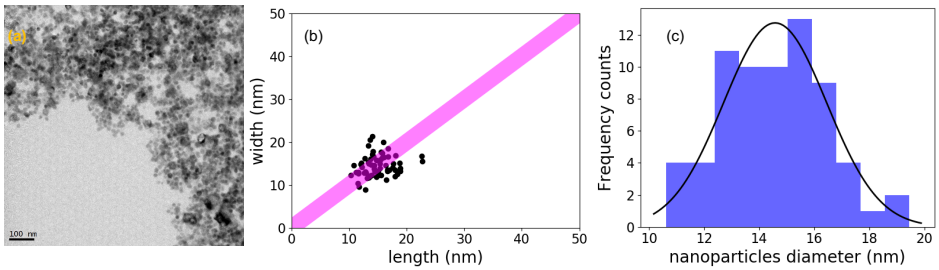

Figure 3.11: (a) TEM image of Cs_2TiBr_6 nanoparticles prepared using only oleic acid and quenching the reaction by diluting the solution with toluene. (b) Plot of the width vs the length of the nanoparticles, which indicates the nanoparticles are close to the symmetry. (c) Histogram of the NCs diameters, calculated from the area of the NCs, indicating an average NC diameter of 14.7 nm, with a standard deviation of around 1.9 nm

3.2.5 Study of the effect of the quenching method and of the injecting temperature on the shape of the NCs

The common quenching method used in the colloidal synthesis of perovskite nanocrystals consists in a ice/water bath. After the synthesis at high temperature, the solution is cooled down to room temperature by dipping the flask into a container filled with water or ice/water and in this way the reaction, i.e. the growth of the nanocrystals, is interrupted. However, we observed that when quenching the reaction with this method, the nanocrystals grow with the irregular shape of big rods, both when using only oleic acid and when adding the zwitterionic ligand (Figure 3.12 a and c). Therefore, a new method was explored, consisting in diluting the solution with toluene, which quenches fast the reaction because it decreases the temperature and dilutes the precursors simultaneously, preventing further growth of the NCs. With this method, only the NCs grown at high temperature, which are the most symmetrical ones, are produced (Figure 3.12 b and d).

In order to understand why the traditional quenching method was not effective, lower reaction temperatures were tested, and it was observed that the material forms even

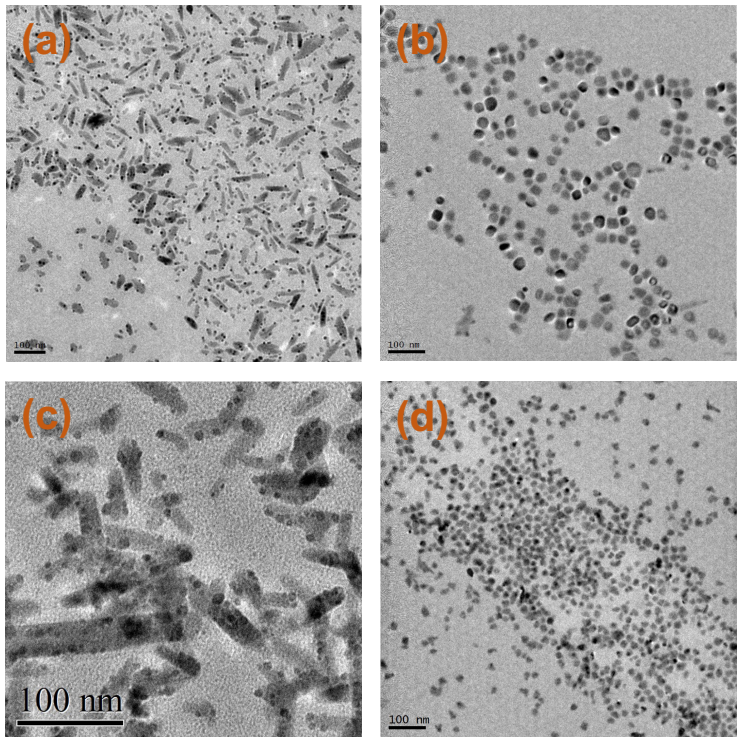

Figure 3.12: Effect of the different quenching method. TEM image of Cs_2TiBr_6 NCs prepared with oleic acid and the zwitterionic ligand using (a) the water bath and (b) the dilution in toluene to quench the reaction. TEM image of Cs_2TiBr_6 NCs prepared only with oleic acid and using (c) the water bath and (d) the dilution in toluene to quench the reaction

in these conditions, as demonstrated by XRD (Figure 3.13), but the NCs grow with less symmetrical shapes (Figure 3.14).

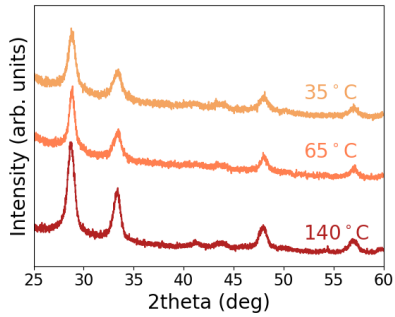

Figure 3.13: XRD patterns of Cs_2TiBr_6 prepared at different temperatures

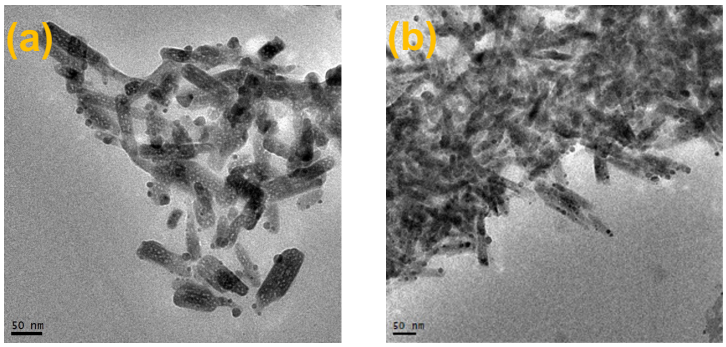

Figure 3.14: TEM images of Cs_2TiBr_6 NCs prepared at (a) 35°C and (b) 65°C

3.3 Synthesis and characterization of $Cs_2TiBr_{6-x}I_x$

3.3.1 Colloidal synthesis

Once the synthesis of Cs_2TiBr_6 NCs was optimized, we used the same colloidal method to attempt the synthesis of pure Cs_2TiI_6 and mixed-halide $Cs_2TiBr_{6-x}I_x$ NCs, by partially or fully replacing TMSBr with TMSI. The synthetic conditions were kept the same as for the pure bromide perovskite, except that the ratio of the iodide precursor over the cation precursors must be doubled, compared to the bromide case, in order to produce the pure iodide perovskite and avoid the formation of byproducts. This means that when referring to 0.5 ratio* of bromide/iodide precursors, it signifies that we used half of the TMSBr moles used in the Cs_2TiBr_6 synthesis and half of the TMSI moles used in the Cs_2TiI_6 synthesis, even though the synthesis required twice TMSI than TMSBr. The optimization of the precursors' ratio used in the Cs_2TiI_6 synthesis is discussed in Chapter 4.

3.3.2 Characterization

Figure 3.15(a) illustrates the XRD patterns of pure bromide Cs_2TiBr_6, pure iodide Cs_2TiI_6 and of the mixed-halide species. All crystals possess $Fm\bar{3}m$ space group symmetry and, as expected, the diffraction angles decrease going from the pure bromide to the pure iodide perovskite, indicating an increase in the unit cell parameter, from 10.706(3) Å to 11.468(5) Å for Cs_2TiI_6 (Figure 3.15(b)). Using Vegard's law, we calculated the amount of iodide inserted for each different precursors' ratio, and the results are shown in Figure 3.16.

As for Cs_2TiBr_6, we checked that the XRD pattern of the titanium halide, in this case TiI_4, does not overlap with the diffraction pattern of the perovskite, in order to discard the presence of this byproduct (Figure 3.17).

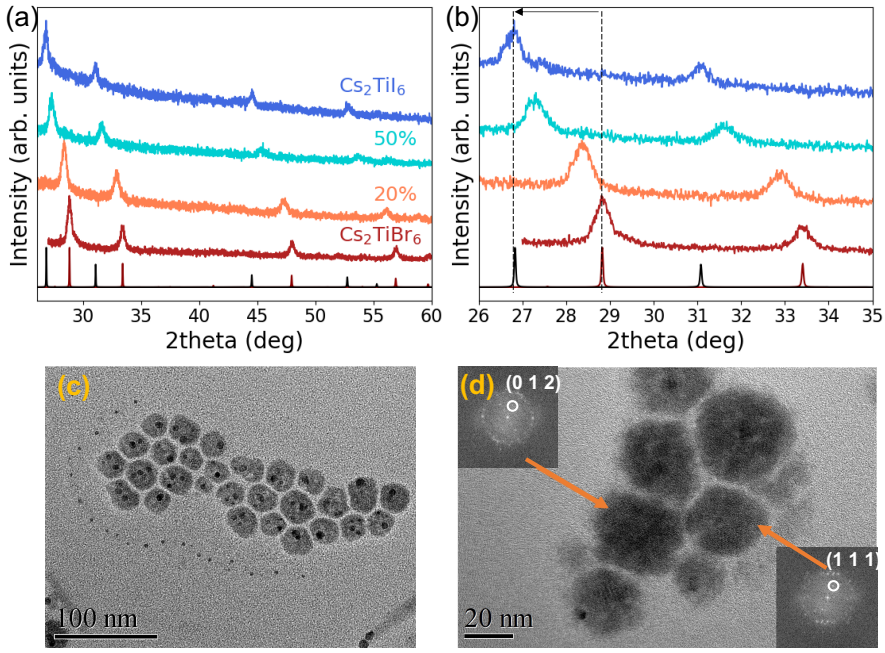

Figure 3.15: (a) XRD patterns of mixed halide $Cs_2TiBr_{6-x}I_x$ NCs with the corresponding standards of pure bromide (bordeaux) and pure iodide (black) perovskites. (b) Expanded XRD patterns. (c) TEM image of $Cs_2TiBr_{6-x}I_x$ NCs prepared using TMSI and TMSBr in ratio 0.7. (d) HRTEM image of Cs_2TiI_6 NCs. In the two insets of (d), FFT images of two NCs

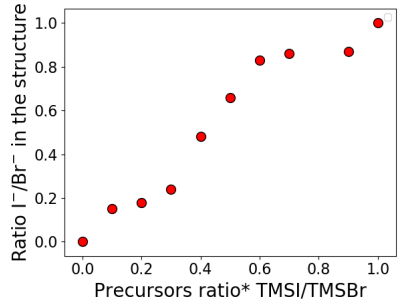

Figure 3.16: Ratio iodide/bromide in the structure of the perovskite (calculated from Vegard's law) vs precursors' ratio*, which is the ratio of the precursors considering the optimal X moles for the two pure halide perovskites' syntheses

TEM images of the mixed-halide perovskites and of the pure iodide perovskite illustrate the synthesis produces polydispersed NCs with less regular shapes than the bromide NCs (Figure 3.15(c) and Figure 3.18). A HRTEM image of pure iodide Cs_2TiI_6 perovskite shows d-spacings matching the lattice parameter extracted from the XRD pattern (Figure 3.15(d)).

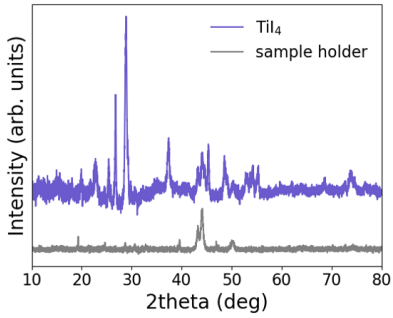

Figure 3.17: XRD pattern of TiI_4 powder, taken using an air-sensitive sample holder to avoid decomposition due to air exposure

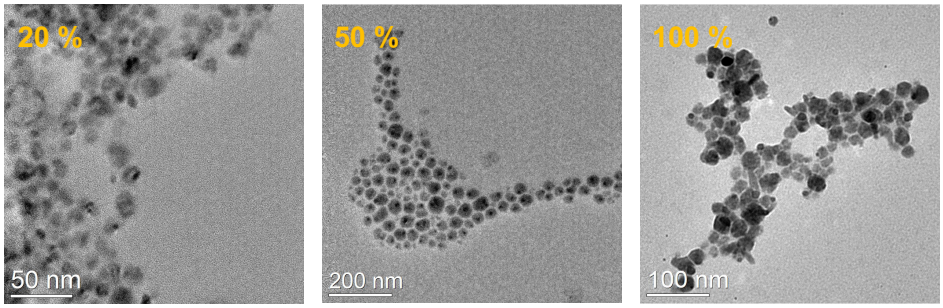

Figure 3.18: TEM images for two mixed halides and pure iodide $Cs_2TiBr_{6-x}I_x$ NCs

The elemental analysis was carried out using the STEM-EDS analysis on pure iodide and mixed-halide samples, which confirmed the presence of Cs, Ti and both Br and I (Figure 3.19 and Figure 3.20).

Table 3.1: Elemental content of Cs_2TiBr_6, Cs_2TiI_6 and $Cs_2TiBr_3I_3$ obtained from ICP-OES measurements

	Ti (mmol)	Cs (mmol)	Cs/Ti
Cs_2TiBr_6	0.027	0.057	2.1
Cs_2TiI_6	0.010	0.021	2.1
$Cs_2TiBr_3I_3$	0.030	0.060	2

Moreover, the quantitative analysis of the ratio Cs/Ti was obtained from ICP-OES, which confirmed a value of 2.1 for Cs_2TiI_6 and a value of 2 for $Cs_2TiBr_3I_3$, as summarized in Table 3.1.

Figure 3.21(a) shows the absorption spectra of the mixed-halide perovskite solutions. When increasing the amount of iodide in the structure, the absorption onset shifts towards longer wavelengths, and two characteristic peaks at around 570 nm and 790

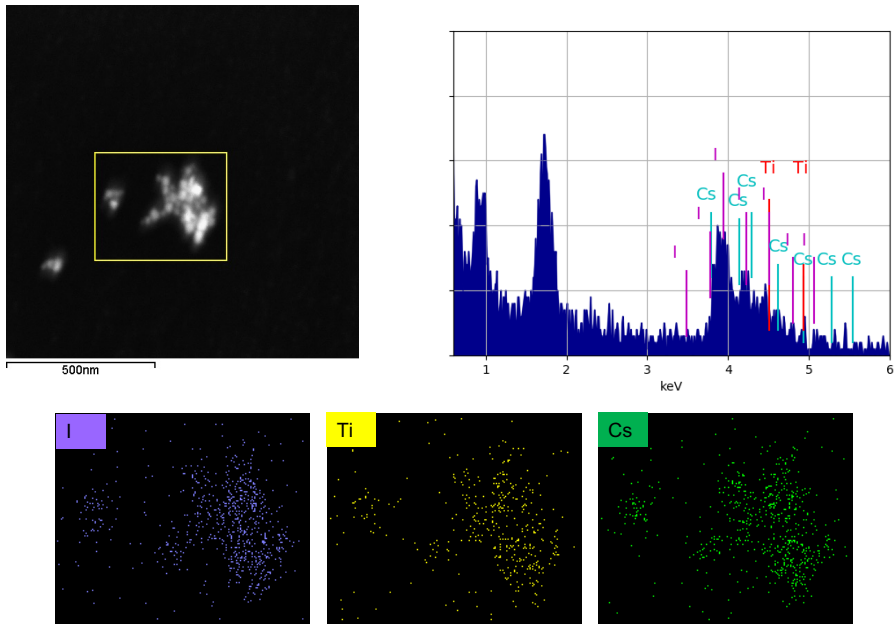

Figure 3.19: HAADF image and STEM-EDS analysis of Cs_2TiI_6 NCs with the corresponding atomic maps. In the spectrum, the peaks at 0.93 and 1.74 keV are due to copper of the TEM grid and silicon contamination coming from the Si(Li) detector, respectively

nm appear. This redshift of the absorption onset is visible to the naked eye already when just 24% of bromide has been replaced by iodide, as this material appears dark brown (3.21(b)).

The direct bandgaps for all the combinations were extracted from Tauc plots (Figure 3.22) and plotted against the ratio of iodide and bromide in the structure, calculated from Vegard's law, (Figure 3.21(c)). It is possible to tune the bandgap from 2.3 eV to 1.2 eV when 87% of bromide is replaced by iodide. The bandgap decreases until 87% replacement but then increases to 1.3 eV for pure iodide perovskite. This trend is in agreement with previously reported theoretical values, [132] plotted in Figure 3.21(c), and is ascribed likely to bandgap reduction from Urbach tailing due to anionic disorder in the crystal structure.

3.4 Stability

In the literature there are contradictory results about the stability of Cs_2TiBr_6 in air. Some studies claim that this material is intrinsically and environmentally stable, [81, 111, 132] while others found that it decomposes fast in air, producing CsBr and

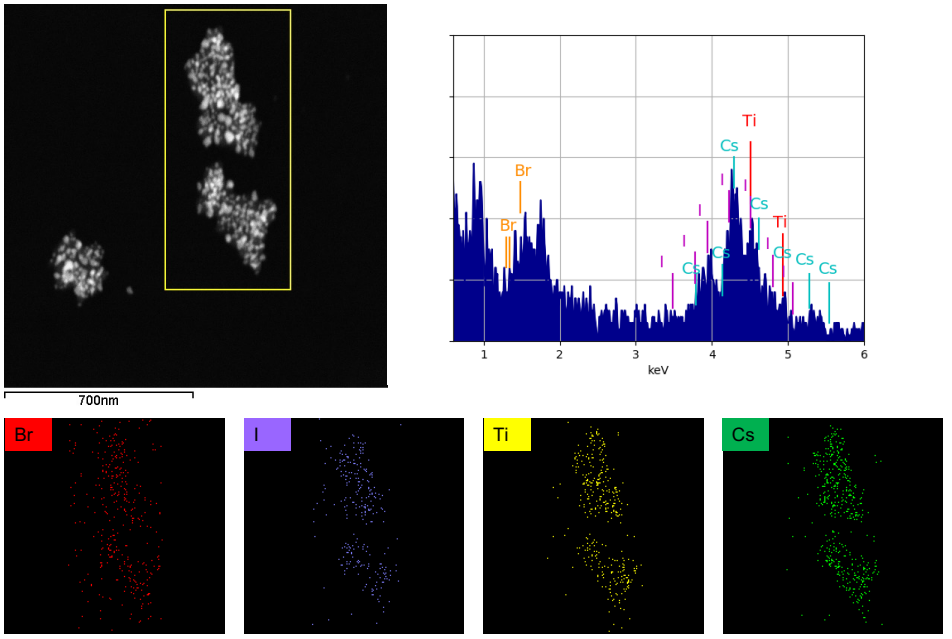

Figure 3.20: HAADF image and STEM-EDS analysis of the mixed-halide $Cs_2TiBr_{6-x}I_x$ sample prepared with 0.5 ratio* of bromide and iodide precursors (50% sample) with the corresponding atomic maps. In the spectrum, the peaks at 0.93 and 1.74 keV are due to copper of the TEM grid and silicon contamination coming from the Si(Li) detector, respectively

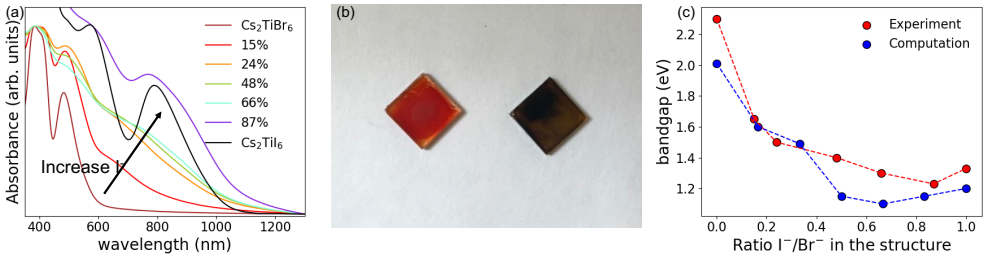

Figure 3.21: (a) Absorption spectra of $Cs_2TiBr_{6-x}I_x$ NC solutions. (b) Picture of Cs_2TiBr_6 and $Cs_2TiBr_{4.5}I_{1.5}$ films prepared from the colloidal solutions. (c) Comparison between experimental bandgaps and computed bandgaps of a series of $Cs_2TiBr_{6-x}I_x$ perovskites. The theoretically predicted values were taken from the literature [132]

amorphous titanium oxide. [112, 113, 133, 134]

In this work, the colloidal Cs_2TiBr_6 NC solution and films prepared by dropcasting the solution on silicon or glass substrates are stable for weeks when prepared and stored under nitrogen atmosphere. However, we observed fast degradation of the films into

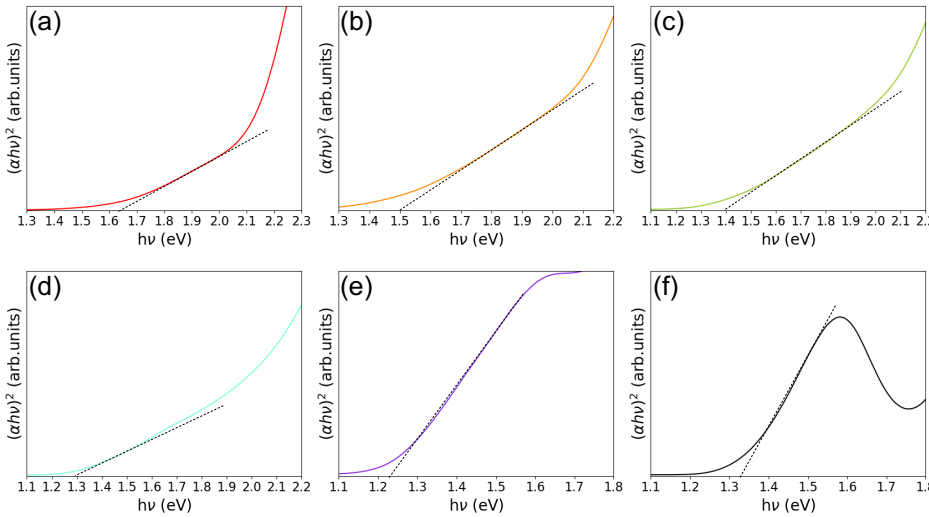

Figure 3.22: Tauc plots of $Cs_2TiBr_{6-x}I_x$ NCs with a) 15%, b) 24%, c) 48%, d) 66%, e) 87% and f) 100% iodide in the structure

CsBr when exposing them to air (Figure 3.23 and Figure 3.24).

Figure 3.23: Decomposition in air of a film prepared from a solution of Cs_2TiBr_6 drop-casted on glass in the glovebox after 5 and 10 minutes

Such a fast decomposition probably occurs because the nanoparticles possess a much bigger surface to volume ratio compared to the bulk, and therefore are more susceptible to decomposition due to the interaction with humidity and oxygen. To further investigate the stability of Cs_2TiBr_6 NC films under environmental conditions, we exposed them to UV-light and heat under nitrogen atmosphere. The NC films are stable after 4 hours under UV light at 395 nm with power density of 15 mW/m^2, and for 1 hour at 100°C (Figure 3.24).

The stability at higher temperatures was also studied. We heated the films for 1 hour at increasing temperatures and observed a partial degradation at 150°C, and a complete degradation into CsBr and most probably into amorphous titanium oxide at 300°C

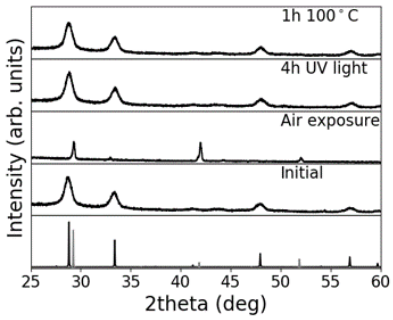

Figure 3.24: Stability of Cs_2TiBr_6 NCs films under different conditions together with the standard XRD patterns of Cs_2TiBr_6 (in black) and CsBr (in grey)

(Figure 3.25).

Regarding the mixed halide $Cs_2TiBr_{6-x}I_x$ NCs, it was observed that they are all intrinsically stable, namely they are stable when stored inside the glovebox, but they all decompose into CsI, CsBr and the amorphous titanium compound when exposed to air.

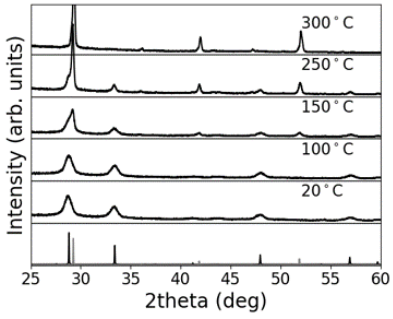

Figure 3.25: XRD of Cs_2TiBr_6 films after heating at different temperatures under nitrogen atmosphere for 1 hour

3.5 Conclusions

In summary, we have reported the first colloidal route to synthesize Cs_2TiBr_6 vacancy-ordered perovskite NCs with control over their size distribution and shape, showing a bandgap of 2.3 eV and an emission peak at 580 nm. Moreover, we demonstrated that by partially or fully replacing the bromide precursor with the corresponding iodide precursor, it is possible to synthesize mixed- and pure-halide $Cs_2TiBr_{6-x}I_x$ NCs, with tunable bandgap between 1.2 eV and 2.3 eV. All the NCs show the expected cubic crystal structure, with the lattice parameter increasing from pure bromide to pure

iodide. Additionally, we have observed that in all the syntheses, it is important to use a large excess of halide precursor to obtain a pure product and that the primary amines commonly used for the colloidal synthesis of perovskite NCs react with the titanium perovskites. Therefore, we used either only OA or a combination of OA and DMOP. Furthermore, we observed that the method used to quench the reaction plays a fundamental role in determining the shape of the NCs, while the role of the zwitterionic ligand is important in stabilizing the nanoparticles during the washing step but does not affect their shape. Finally, the Cs_2TiBr_6 NC films decompose quickly in air, while they are stable for 1 hour at 100 °C and for 4 hours under UV light in a nitrogen atmosphere. For all the other mixed-halide $Cs_2TiBr_{6-x}I_x$ NCs and for pure Cs_2TiI_6 NCs, we also observed fast decomposition in air.

4

$Cs_2Ti_{1-x}Sn_xI_6$ vacancy-ordered perovskites

4.1 Introduction

In 2014, Cs_2SnI_6 vacancy-ordered perovskite was applied for the first time as hole-transport layer in a dye-sensitized solar cell, with reported PCE of 4.7%. [99] Few years later, in 2017, the same group led by Prof. Kanatzidis, reported its preparation from spontaneous oxidation in air of $CsSnI_3$, and its application as solar cell light absorber with PCE near 1%. [83] Contrary to $CsSnI_3$, Cs_2SnI_6 is stable in air, it contains tin that is toxicologically inactive, [58] due to its higher oxidation state, while at the same time it possesses a relatively narrow bandgap, between 1.2 and 1.6 eV. [99, 101, 105, 106, 108, 127, 130, 131]

Motivated by its reported solar cell applications, its narrow bandgap and its superior stability in air, and supported by the comparable size of Sn^{+4} and Ti^{+4}, [170] we hypothesized that tin and titanium could combine in the same vacancy-ordered perovskite structure. Indeed, in the literature there are several examples of mixed B-cations perovskites that have been synthesized either by cation exchange or by direct synthesis. [171–177] Sometimes they only demonstrated bandgap tunability while in other cases they showed superior properties compared to the respective pure B-cation

perovskites, such as higher stability [173] and higher PLQY. [174] Due to the higher stability of the pure tin perovskite compared to the titanium one, our purpose was to verify if adding tin to the structure could be a mean to increase the stability of titanium perovskites.

We carried out a computational study on all the Cs_2SnX_6 and Cs_2TiX_6 systems and indeed we observed that Ti/Sn alloys have very low mixing energies, which indicates that they can combine very easily in the same crystal structure. Moreover, stability studies based on thermodynamic analyses confirmed that all these perovskites are intrinsically stable and that the tin ones are more stable against oxidation compared with the titanium ones.

Experimentally, we first attempted the synthesis of Cs_2SnI_6, using the same method reported for the synthesis of Cs_2TiX_6 in Chapter 3, with the purpose of eventually combine Sn and Ti in the same crystal structure by carrying out the direct colloidal synthesis using both Sn and Ti precursors. While the colloidal synthesis of Cs_2SnI_6 was already reported by different groups, they always used the same hot-injection method consisting in the injection to a solution of SnI_4 in ODE of a cesium precursor, either cesium oleate [157,178,179] or cesium carbonate dissolved in oleylamine. [180] In this chapter, we present a new synthetic method to prepare Cs_2SnI_6, starting from cesium oleate and tin(IV) acetate and injecting at high temperature trimethylsilyl iodide. Moreover, we show that with this method it is possible to tune the size of the NCs just by increasing the injection temperature of the iodide precursor. The evidence that Cs_2SnI_6 can be prepared using the same method as Cs_2TiX_6 was the starting point to attempt the synthesis of mixed $Cs_2Ti_{1-x}Sn_xI_6$ perovskites.

In this chapter, we report for the first time the synthesis of mixed tin-titanium $Cs_2Ti_{1-x}Sn_xI_6$ perovskite NCs and their chemical, structural, morphological and optical characterization.

4.2 Preliminary computational evidences

From calculations, it was observed that the mixing energies for the Sn/Ti alloys are extremely low (Figure 4.1(a)). This result was expected because the vacancy-ordered structure consists of isolated octahedra, so that the interactions between different B elements are very weak and thus the alloys behave almost like “ideal mixtures”.

Figure 4.1(b) shows that the calculated lattice constants of $Cs_2Ti_{1-x}Sn_xI_6$ perovskites with x between 0 and 1 follow a linear behavior, perfectly obeying Vegard’s law, which again confirms the low interactions between B elements, due to the 0D structure.

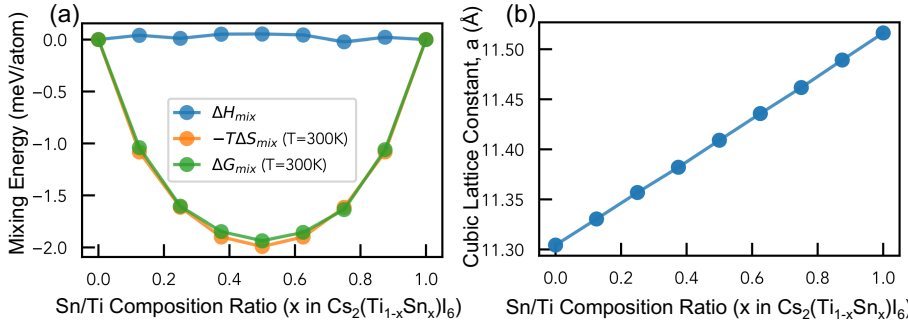

Figure 4.1: (a) Calculated mixing energies and (b) lattice constants for different $Cs_2Ti_{1-x}Sn_xI_6$ perovskites

The intrinsic stabilities and competing phases of all the halide Cs_2BX_6 perovskites, with B = Sn or Ti were calculated and it was observed that all the materials are intrinsically stable, as they all have positive decomposition energies (Table 4.1). The decomposition energy is the energy needed to separate the compound into the lowest energy intrinsic competing phases in the same Cs-B-X chemical space, i.e. for Cs_2SnI_6, the competing phases are CsI_3, SnI_4, CsI_4, CsI, I and $CsSnI_3$. A negative value would mean spontaneous decomposition while the more positive is the value, the more intrinsically stable the material is with respect to the competing phases.

Table 4.1: Calculated decomposition energies, using dispersion corrections, for Cs_2BX_6, B = Sn, Ti , X = Cl, Br or I

	Cs_2SnI_6	Cs_2SnBr_6	Cs_2SnCl_6	Cs_2TiI_6	Cs_2TiBr_6	Cs_2TiCl_6
Hybrid DFT + vdW Decomposition Energy (eV)	56 meV	129 meV	174 meV	75 meV	120 meV	162 meV

From Figure 4.2, surprisingly, it is observed that all the titanium perovskites are stable over much wider Ti and halide chemical potential ranges than the Sn compounds, driven by a significantly greater stability of fully-oxidized Ti^{4+} than Sn^{4+} in the Cs_2BX_6 crystal structure, [127] as well as the lack of stable competing phases with Ti^{2+}, contrary to the case of Sn, with $CsSnI_3$, $CsSn_2Br_5$, $CsSn_2Cl_5$ competing phases.

However, when it comes to exposure to oxygen the picture gets opposite with titanium perovskites being more unstable than tin. This situation was studied by calculating the external decomposition energies of the compounds, considering the following reactions in the presence of O_2:

- $Cs_2SnI_6 + O_2 \rightarrow SnO_2 + CsI_3$

- $Cs_2TiI_6 + O_2 \rightarrow TiO_2 + CsI_3$

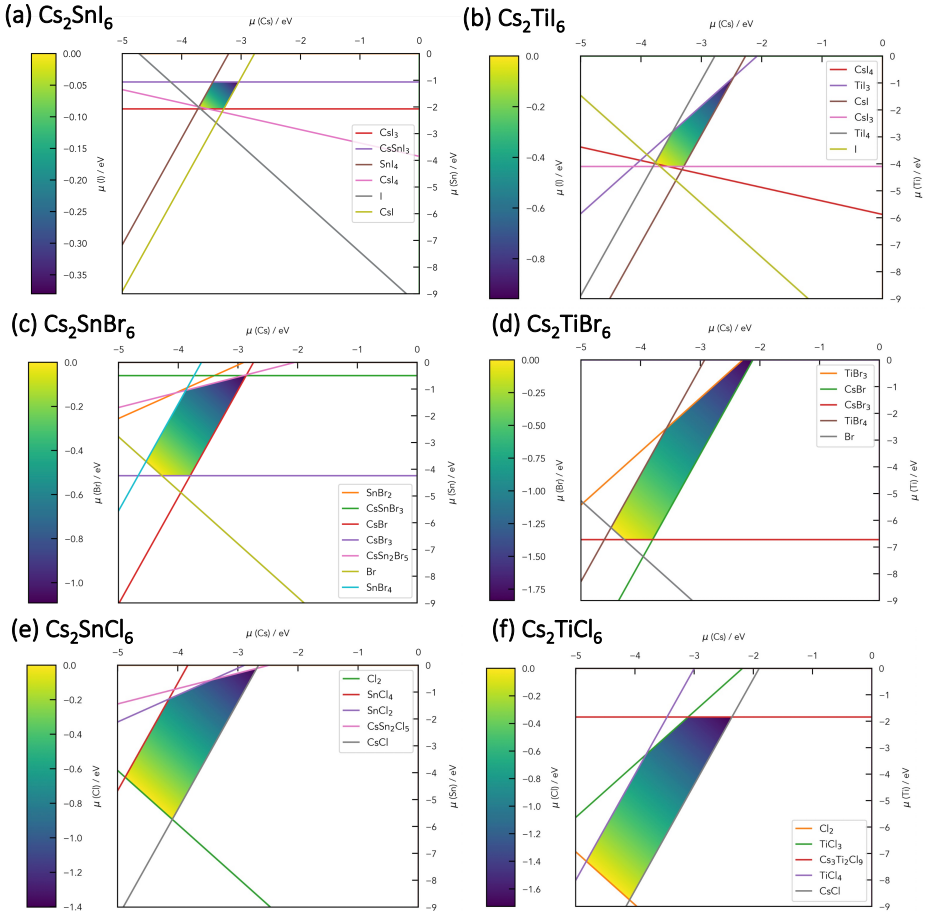

Figure 4.2: Allowed values of Cs, Ti/Sn and I/Br/Cl chemical potentials (coloured area), which defines the thermodynamic stability of the perovskites

- $Cs_2SnBr_6 + O_2 \rightarrow SnO_2 + CsBr_3$

- $Cs_2TiBr_6 + O_2 \rightarrow TiO_2 + CsBr_3$

- $Cs_2SnCl_6 + O_2 \rightarrow SnO_2 + ClO_2 + CsClO_4$

- $Cs_2TiCl_6 + O_2 \rightarrow TiO_2 + ClO_2 + CsClO_4$

As experimentally observed, all the titanium perovskites are more thermodynamically unstable than the tin perovskites when exposed to oxygen, due to the very high stability of the decomposition product TiO_2 compared with SnO_2. Moreover, as observed in Table 4.2, that summarizes these results, the iodide perovskites are more unstable than the bromide ones, and the chloride ones are the only ones with a positive decomposition energy, indicating they thermodynamically do not tend to decompose into the oxidized

compounds. This agrees with what we observed in Chapter 2, namely that Cs_2TiCl_6 is the only titanium(IV) perovskite to be stable in air. Lastly, it is important to remember that all these calculations do not consider the kinetics of the oxidation reactions, meaning that if their activation energy is high enough the oxidation reaction is suppressed even when the decomposition energies are negative.

These preliminary computational results confirmed our hypotheses and motivated us even more to attempt the synthesis of mixed titanium/tin perovskite NCs.

Table 4.2: Data of the decomposition energy of Cs_2BX_6 when reacting with oxygen

	Cs_2SnI_6	Cs_2SnBr_6	Cs_2SnCl_6	Cs_2TiI_6	Cs_2TiBr_6	Cs_2TiCl_6
O_2 Decomposition Energy	-2.47 eV	-0.31 eV	+14.1 eV	-4.54 eV	-1.91 eV	+12.92 eV

4.3 Synthesis of $Cs_2Ti_{1-x}Sn_xI_6$ NCs

The syntheses of mixed titanium-tin cesium iodide perovskite NCs were carried out using the same method described in the previous chapter for the synthesis of pure titanium halide perovskites, with some modifications. As for the synthesis of the titanium halide perovskite nanocrystals, the cations' precursors were loaded in a three-neck flask, ODE was used as solvent while OA and DMOP were used as ligands. Moreover, the halide precursor was injected at high temperature in the degassed solution and the reaction was quenched by cooling down and diluting the solution with toluene.

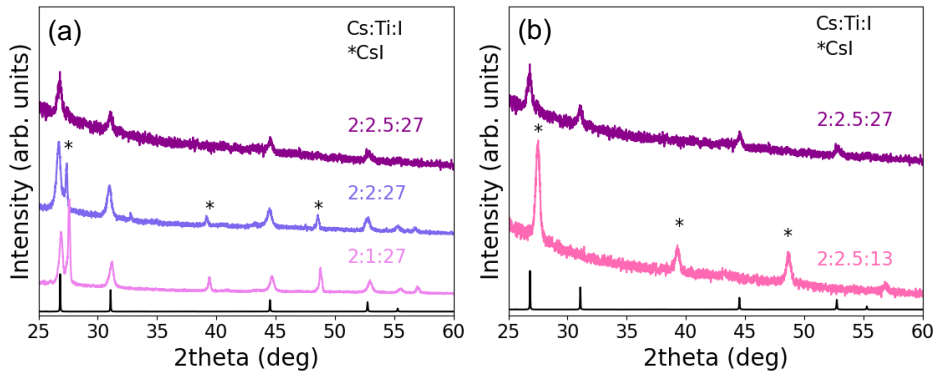

Figure 4.3: (a) XRD patterns of samples prepared with different Cs:Ti ratios. (b) XRD patterns of samples prepared with different Cs:I ratios. In both plots, the black pattern is the VESTA calculated Cs_2TiI_6 pattern with the same lattice parameter as the experimental samples.

However, the preparation of these new NCs was carried out with some differences.

First of all, cesium oleate was used instead of cesium acetate and for its preparation we followed a procedure taken from the literature. [181] Secondly, in the washing step, methylacetate was used instead of acetone. The reason for this change is that it was observed that acetone is chemically more aggressive than methylacetate as antisolvent, in the sense that it needs to be added very slowly to the solution to avoid the aggregation of the NCs. The same carefulness is needed when using methylacetate but to a lower extent. In general, the iodide perovskites demonstrated more sensitivity to the antisolvent than the bromide ones.

Finally, the main parameters to optimize in the synthesis were the precursors' ratios. For the synthesis of pure titanium Cs_2TiI_6, the optimized precursors' ratio was Cs:Ti:I = 2:2.5:27, because a lower amount of titanium or iodide leads to the production of CsI as byproduct, as shown in Figure 4.3.

For the synthesis of Cs_2SnI_6, the stoichiometric ratio Cs:Sn:I = 2:1:6 is sufficient to produce pure nanocrystals. Nonetheless, it was observed that a higher amount of iodide or titanium precursors in the synthesis does not affect the purity of the final product (Figure 4.4).

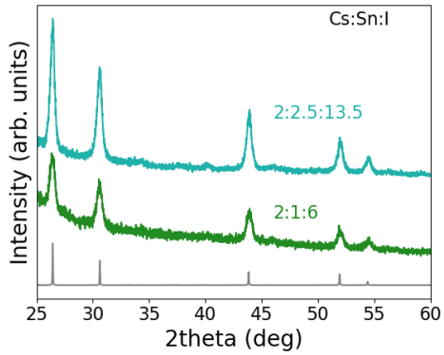

Figure 4.4: XRD patterns of Cs_2SnI_6 synthesized using two different precursors' ratios

For the syntheses of mixed titanium-tin cesium iodide perovskite NCs, the ratio of cesium and iodide precursors was important in order to avoid the formation of byproducts, while the ratio of titanium and tin precursors was modulated in order to understand how to obtain the desired titanium-tin ratio. It was observed that, similar to what reported for the case of mixed bromide-iodide titanium perovskites, the optimal ratio of tin and titanium precursors in the syntheses is related to the amounts used in the optimized syntheses of the respective pure perovskites. An example is depicted in Figure 4.5(a), in which the XRD patterns of the products from three different syntheses made to obtain the $Cs_2Ti_{0.5}Sn_{0.5}I_6$ sample are represented.

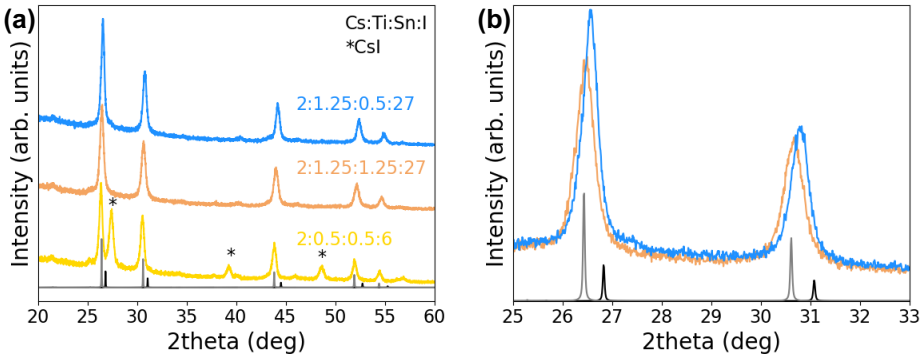

Figure 4.5: (a) XRD patterns of the products of three different reactions in which different precursors' ratios were used, indicated as Cs:Ti:Sn:I. The black pattern is the calculated XRD pattern of Cs_2TiI_6, while the grey pattern represents the calculated XRD pattern of Cs_2SnI_6. (b) Zoom of XRD patterns illustrating the shift of position to lower angles for the precursors' ratio Cs:Ti:Sn:I = 2:1.25:1.25:27, in orange, and Cs:Ti:Sn:I = 2:1.25:0.5:27, in blue

The yellow pattern represents the XRD pattern of the product of the synthesis carried out using a precursors' ratio of 2:1:6, and mixing half moles of tin precursor and half moles of titanium precursor. From XRD, the final product of this synthesis shows pure tin perovskite Cs_2SnI_6 and the byproduct CsI, while we also expect the formation of an amorphous titanium compound, such as TiO_2, not observable with this technique. Therefore, in the next synthesis a higher amount of all the precursors except cesium oleate was used in order to prevent the formation of CsI. In this synthesis the moles of tin and titanium precursors are kept the same, 50% each, but the overall precursors' ratio is 2:2.5:27, as in the optimized synthesis of pure titanium Cs_2TiI_6. In this case, XRD pattern of the product, in orange in Figure 4.5(a), does not show any CsI peak. The diffraction peaks of the perovskite were all slightly shifted to higher angles compared with the previous sample, as visible in Figure 4.5(b), indicating that in this case a certain amount of titanium is inside the structure. A lattice parameter of 11.627(7) Å was extracted and using Vegard's law, it was calculated that around 76% of the B component in the structure was tin.

To obtain a perovskite with a higher amount of titanium in the structure, half of the amounts used in the respective pure titanium and pure tin perovskite syntheses were used, that means that the precursors' ratio was 2:1.25:0.5:27. In this case, the XRD of the product shows a pure perovskite structure containing approximately 50% of tin, calculated using Vegard's law (lattice parameter = 11.5730(14) Å, obtained from Rietveld refinement), even though more specific ICP-OES measurements show the amount of tin in the structure corresponds to 64% of the total B component.

The same strategy, i.e. referring to the ratios of tin and titanium precursors used for the syntheses of pure tin and pure titanium perovskites respectively, was used to synthesize all the other $Cs_2Ti_{1-x}Sn_xI_6$ alloys. A recap of these ratios is summarized in Table 4.3.

Table 4.3: Summary of the precursors' ratio used to synthesise $Cs_2Ti_{1-x}Sn_xI_6$ alloys

Sample name	Cs	Sn	Ti	I
Cs_2TiI_6	2	0	2.5	27
25% Sn	2	0.25	1.875	27
50% Sn	2	0.5	1.25	27
75% Sn	2	0.75	0.625	27
Cs_2SnI_6	2	1	0	6

4.4 Characterization of $Cs_2Ti_{1-x}Sn_xI_6$ NCs

4.4.1 Structural characterization

The structural characterization of $Cs_2Ti_{1-x}Sn_xI_6$ NCs was carried out using XRD.

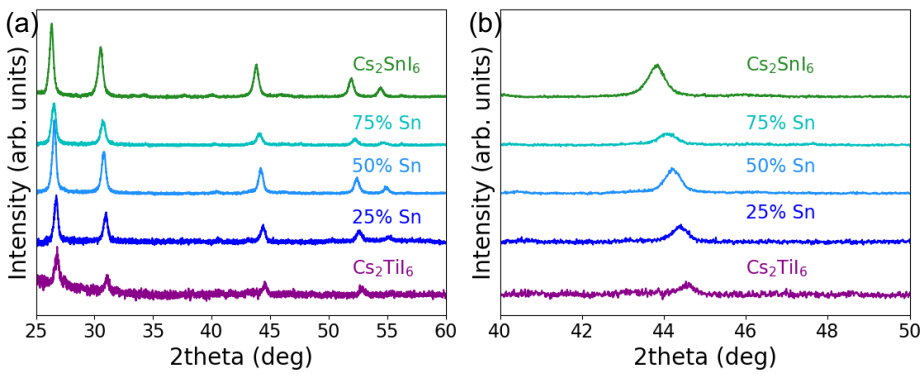

Figure 4.6: (a) XRD patterns of Cs_2TiI_6, Cs_2SnI_6, 25%, 50% and 75% Sn samples. (b) Zoom in the range 40-50 degrees to observe the peaks' shift

Figure 4.6(a) depicts the XRD patterns between 25 and 60 degrees for all the samples. From Rietveld refinement of the diffraction patterns, the lattice parameter of Cs_2TiI_6 is equal to 11.468(5) Å while the lattice parameter of Cs_2SnI_6 is 11.6786(10) Å. The difference in lattice parameter is relatively small, which is the reason why the ratio Sn/(Sn+Ti) calculated from XRD through Vegard's law and collected in Table 4.4 are very approximate and different from the ones measured with ICP-OES, whose results

are reported in the next section. However, the trend is clear, namely when increasing the amount of tin in the structure the diffraction angles decrease, as depicted in Figure 4.6(b).

Table 4.4: X-ray, Rietveld refined lattice parameters and x values calculated using Vegard's law for all the $Cs_2Ti_{1-x}Sn_xI_6$ NC samples

Sample name	Lattice par. (Å)	x
Cs_2TiI_6	11.468(5)	0
25% Sn	11.537(4)	0.33
50% Sn	11.5730(14)	0.50
75% Sn	11.594(5)	0.60
Cs_2SnI_6	11.6786(10)	1

4.4.2 Morphological study of Cs_2SnI_6 NCs

For Cs_2SnI_6 NCs, the effect of reaction temperature, quenching method and amount of iodide precursor on the final shape and size of the nanoparticles was investigated.

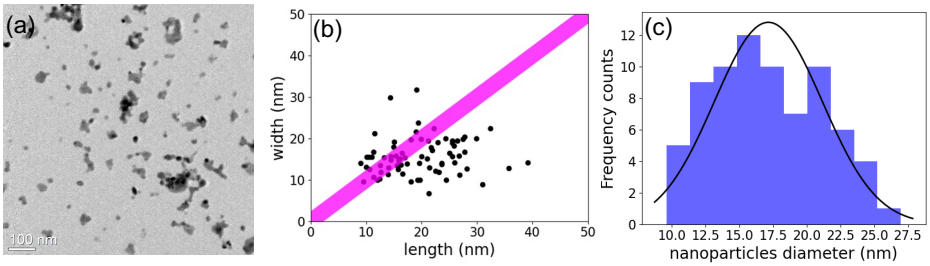

Figure 4.7: (a) TEM image of Cs_2SnI_6 NCs prepared at 75 °C. (b) Plot of the width vs the length of the nanoparticles, which shows the nanoparticles prepared at this temperature are very asymmetric. (c) Histogram of the NCs diameters, calculated from the area of the NCs, indicating an average NC diameter of 17.2 nm, with a standard deviation of 4.0 nm (23%)

To study the influence that the temperature of TMSI injection has on the final morphology of the perovskite NCs, the temperature was tuned from 75°C to 200°C, while the quenching method (dilution in toluene) and the precursors' ratio (Cs:Sn:I = 2:1:6) were kept unmodified. For the size distribution analysis, the areas of 150 NCs per sample were calculated. Figure 4.7(a) shows a TEM image of the NCs prepared at 75 °C. The NCs prepared at this temperature have an anisotropic shape, as depicted in Figure 4.7 (b), and show a broad size distribution with average size of around 17 nm, and standard deviation of 23% (Figure 4.7 (c)). Such a big standard deviation indicates that at this temperature the control on the size of the NCs is not achieved.

A clear increase in symmetry is already visible in the product of the reaction carried out at 100 °C (Figure 4.8). The nanoparticles prepared at this temperature have an average size of around 16.3 nm, with a standard deviation of around 2.5 nm, corresponding to 15%.

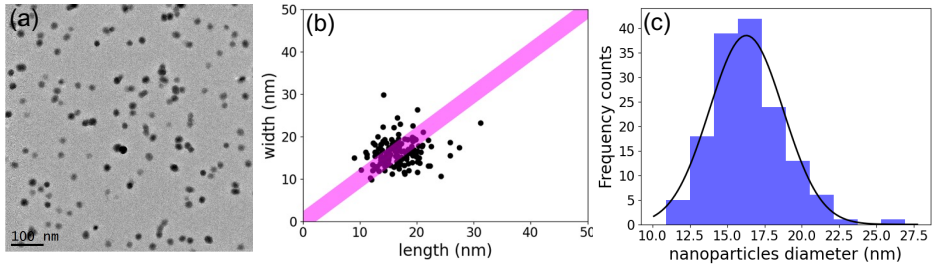

Figure 4.8: (a) TEM image of Cs_2SnI_6 NCs prepared at 100 °C. (b) Plot of the width vs the length of the NCs. (c) Histogram of the NCs diameters, calculated from the area of the NCs, indicating an average NC diameter of 16.3 nm, with a standard deviation of around 2.5 nm

The NCs prepared at 140 °C, shown in Figure 4.9, are slightly smaller, namely 15.9 nm, and appear more cuboid-shaped. Moreover, the size distribution is narrower, i.e. 2.0 nm (12.6%), demonstrating that at this temperature there is a better control on the nanocrystals' growth.

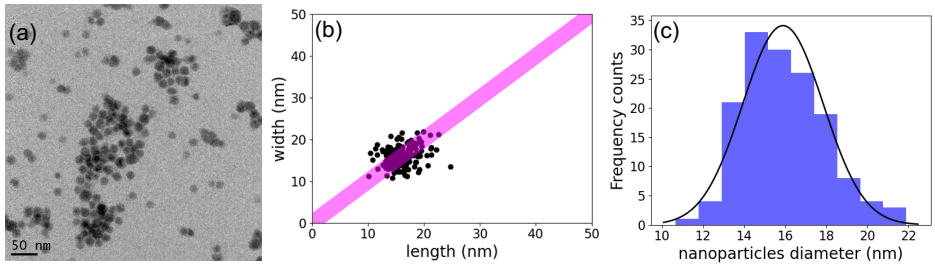

Figure 4.9: (a) TEM image of Cs_2SnI_6 NCs prepared at 140 °C. (b) Plot of the width vs the length of the NCs. (c) Histogram of the NCs diameters, calculated from the area of the NCs, indicating an average NC diameter of 15.9 nm, with a standard deviation of around 2.0 nm.

When carrying out the reaction at 170 °C, the nanocrystals are visibly bigger and with a broader size distribution, as shown in Figure 4.10. The NCs have similar shapes to the ones prepared at 140 °C, and an average size of 28.7 nm, with standard deviation of 3.8 nm (13.2%).

This trend, namely the increase of the NCs size with temperature increase is confirmed

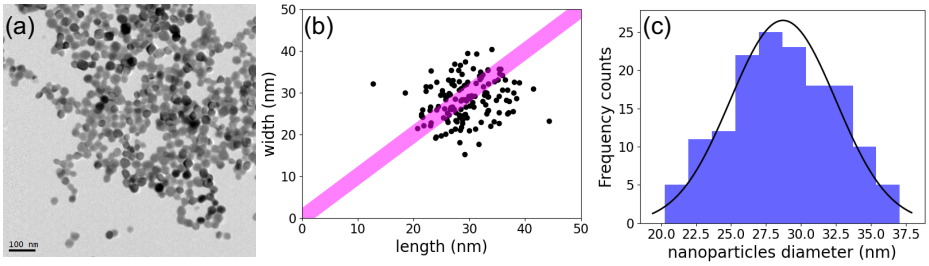

Figure 4.10: (a) TEM image of Cs_2SnI_6 NCs prepared at 170 °C. (b) Plot of the width vs the length of the NCs. (c) Histogram of the NCs diameters, calculated from the area of the NCs, indicating an average NC diameter of 28.7 nm, with a standard deviation of around 3.8 nm

by the last experiment, carried out at 200 °C, whose results are shown in Figure 4.11. The NCs diameter measures 30.6±6.3 nm (18.2%), even though in this case, it was harder to measure the size of the single NCs because they tend to coalesce.

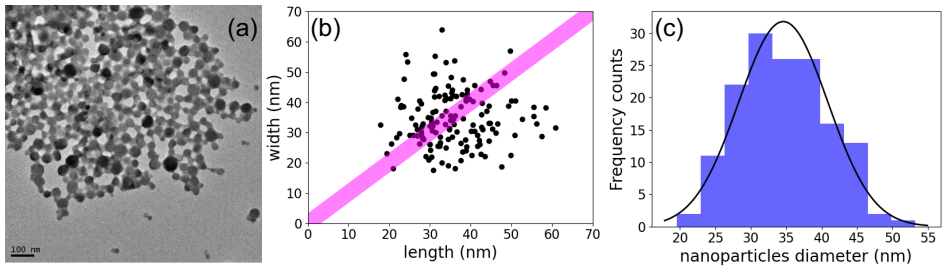

Figure 4.11: (a) TEM image of Cs_2SnI_6 NCs prepared at 200 °C. (b) Plot of the width vs the length of the NCs. (c) Histogram of the NCs diameters, calculated from the area of the NCs, indicating an average NC diameter of 30.6 nm, with a standard deviation of around 6.3 nm

The average sizes and standard deviations of the NCs prepared at different reaction temperature are summarized in Table 4.5.

Table 4.5: Average length and standard deviation of the NCs synthesized at different temperatures

Temperature (°C)	Average length (nm)	Standard deviation nm (%)
75	17.2	4.0 (23%)
100	16.3	2.5 (15.2%)
140	15.9	2.0 (12.6%)
170	28.7	3.8 (13.2%)
200	30.6	6.3 (18.2%)

The main conclusions of this study are that:

- The size of the NCs increases with the temperature at which they are prepared from 140 °C to 200 °C

- The size distribution improves with the temperature increase until 140°C, while beyond this temperature it worsens,

- At 200 °C the NCs tend to coalesce,

- 140 °C is the optimal temperature for achieving the best symmetry and the highest control on the NCs size.

In Chapter 3, it was reported that the quenching method has a big influence on Cs_2TiBr_6 NCs' morphology. Indeed, it was observed that only when diluting the NCs in toluene is it possible to stop the reaction and obtain NCs with similar size and shape, while when quenching the reaction with a water bath the NCs continue to grow at low temperature forming bigger crystals with irregular shapes and different sizes. Therefore, the dilution in toluene was used as the standard quenching method for the preparation of all the NCs described in this chapter. However, it was observed that for Cs_2SnI_6 perovskite NCs, the water bath is also an effective method for quenching the growth of the NCs. Figure 4.12 shows the TEM image of Cs_2SnI_6 NCs prepared at 140°C and using the water bath quenching method. The NCs appear relatively symmetrical and their size distribution is very close to the one obtained when using the "dilution in toluene" quenching method, with an average value of 17.5 nm and a standard deviation of 1.9 nm (10.8%).

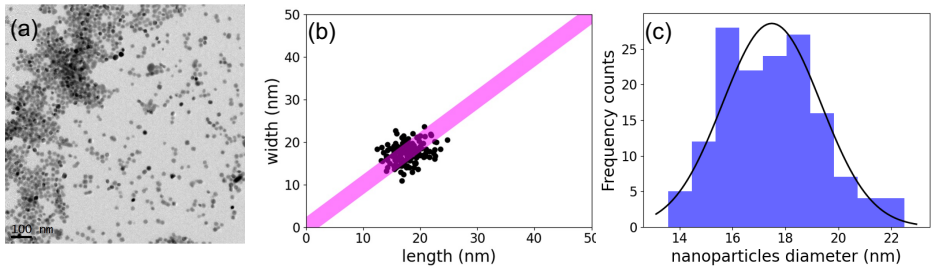

Figure 4.12: (a) TEM images of Cs_2SnI_6 NCs prepared quenching the reaction with a water bath. (b) Plot of the width vs the length of the NCs. (c) Histogram of the NCs diameters, calculated from the area of the NCs, indicating an average NC diameter of 17.5 ±1.9 nm

The last systematic morphological study carried out for Cs_2SnI_6 NCs consisted in observing the influence that the amount of iodide precursor used in the synthesis has

on the morphology of the NCs. The temperature of the reactions was kept at 140°C and the quenching method used was always the "dilution in toluene".

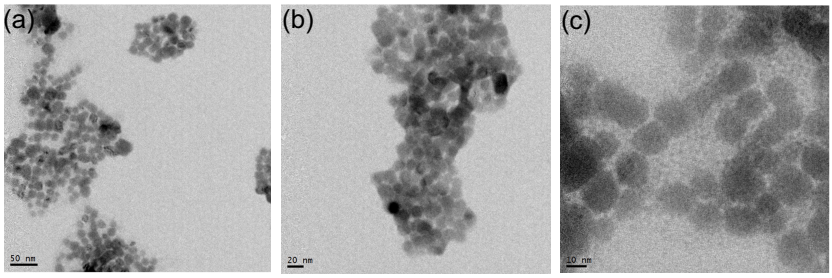

Figure 4.13: TEM images of Cs_2SnI_6 NCs prepared using Cs:Sn:I = 2:1:13 ratio

When using a precursors' ratio equal to Cs:Sn:I = 2:1:13, the shape and size of the NCs is not significantly changed, but the NCs look more agglomerated, even though still detached ones from the others, as visible in Figure 4.13. This is not the case when increasing even more the amount of iodide precursor, up to a ratio of 2:1:27, which is the ratio Cs:I used for Cs_2TiI_6 NCs. In this case, the NCs, shown in Figure 4.14, coalesce producing bigger structures in which the initial NCs are still visible.

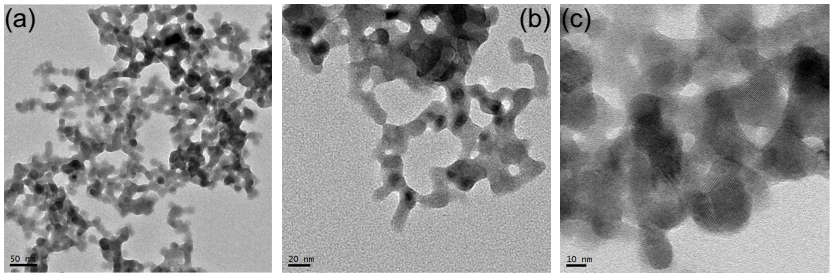

Figure 4.14: TEM images of Cs_2SnI_6 NCs prepared using 2:1:27 ratio

In summary, it was observed that the NCs size depends on the temperature of reaction while the quenching method does not affect the shape of Cs_2SnI_6 NCs, as it was observed for Cs_2TiBr_6. Moreover, it was shown that the higher is the amount of iodide precursor used in the synthesis, the more the NCs coalesce forming bigger structures.

4.4.3 Morphological characterization of $Cs_2Ti_{1-x}Sn_xI_6$ NCs

The TEM images of mixed tin-titanium $Cs_2Ti_{1-x}Sn_xI_6$ perovskite NCs are shown in Figure 4.15. All these samples were prepared using a large excess of iodide precursor, as described in the experimental section. The results from the study regarding the

influence of the amount of iodide precursor on the morphology of the Cs_2SnI_6 NCs suggest that the large excess of iodide needed to prepare $Cs_2Ti_{1-x}Sn_xI_6$ perovskites is probable the origin of the coalescence observed for all these NCs. However, opposite to Cs_2SnI_6, the high amount of iodide precursor used in the synthesis is necessary to avoid the production of CsI.

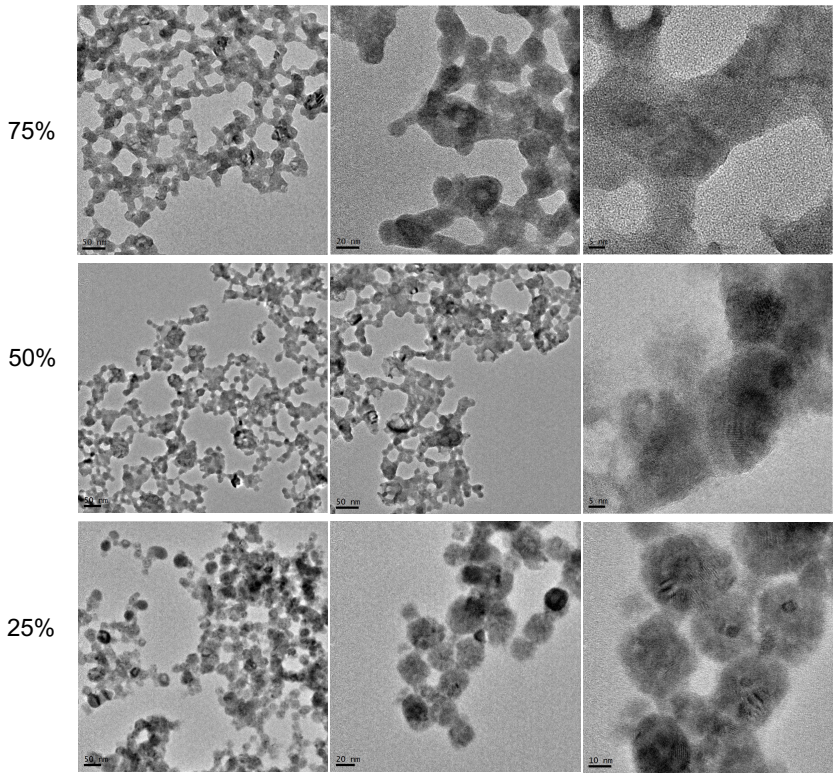

Figure 4.15: TEM images of 25% Sn, 50% Sn and 75% Sn samples

4.4.4 Chemical characterization

The chemical characterization of $Cs_2Ti_{1-x}Sn_xI_6$ NCs was carried out using ICP-OES and EDX. The first technique was used to obtain quantitative information about the ratio of metals in the samples, i.e. the ratio of Cs, Sn and Ti.

Table 4.6 summarizes the ICP-OES analysis, which indicates that Cs_2SnI_6, Cs_2TiI_6 and the 25% sample have a ratio Cs:(Ti+Sn) very close to the stoichiometric one, while in the 50% and 75% samples, the ratio of cesium over the overall B component is lower, which might be due to a different stoichiometry with an excess of B component on the surface of the NCs. Moreover, ICP-OES analysis reveals that for all the mixed B

cation samples, the amount of tin in the structure is higher than what calculated using Vegard's equation from XRD data.

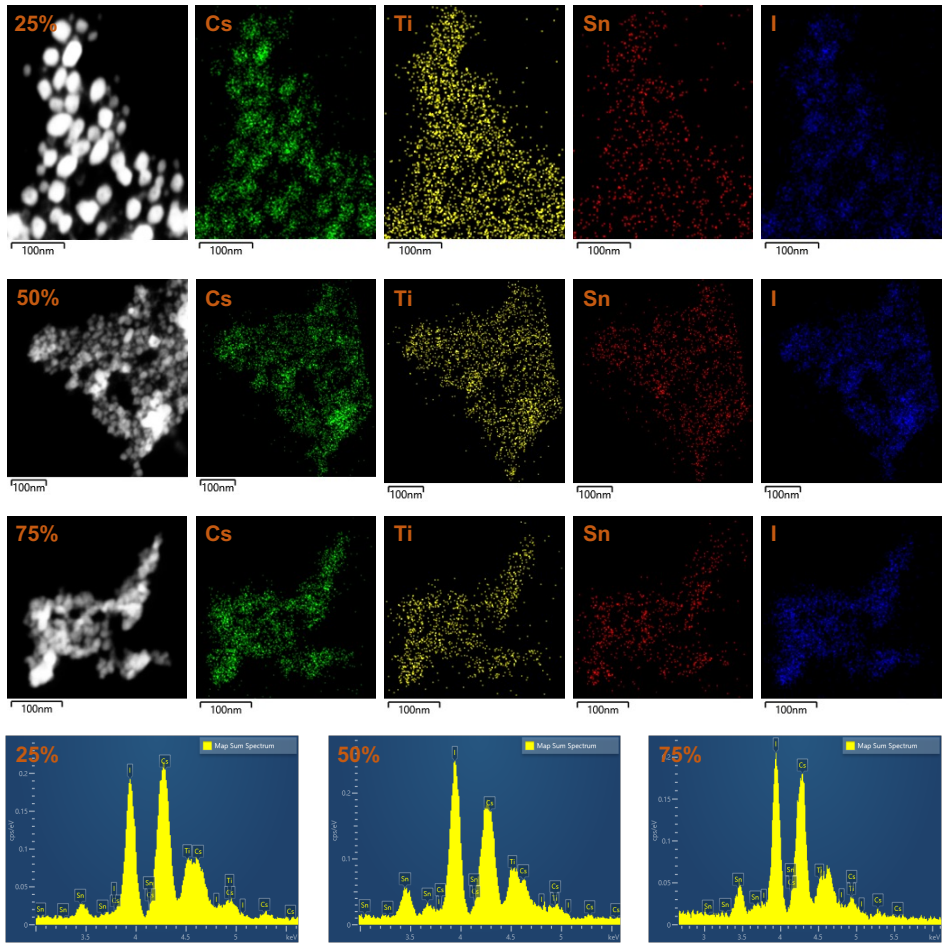

Figure 4.16: High-angle annular dark-field (HAADF) images and STEM-EDX analyses of 25%, 50% and 75% Sn samples with the corresponding atomic maps

Table 4.6: Ratio of precursors used for each synthesis with the corresponding ratio of cations inside the products, measured with ICP-OES

Sample name	Cs:Ti:Sn precursors	Cs/(Ti+Sn)	Sn%
Cs_2TiI_6	2:2.5:0	2.1	0%
25% Sn	2:1.875:0.25	1.95	43%
50% Sn	2:1.25:0.5	1.82	64%
75% Sn	2:0.625:0.75	1.64	82%
Cs_2SnI_6	2:0:1	2	100%

EDX mapping was carried out to verify that the elements were homogenously distributed over the entire sample and that no rich-Sn or rich-Ti regions were visible. The data are shown in Figure 4.16 and no quantification is shown because, as visible from the map sum spectra, the peaks of Cs, Ti and Sn overlap, so the quantification could not be trusted, as in Chapter 3. From the atomic maps, it appears that all the elements are homogenously distributed, even though the spatial resolution of this measurement in the instrument used is not high enough to observe the elemental distribution in each NC. However, from computational results, the mixing energy of Sn and Ti should be very low and therefore homogenous distributions of Sn and Ti are expected.

4.4.5 Optical characterization

The optical characterization of the NCs was carried out in solution to avoid oxidation of the NCs in air when deposited as films. We also measured the photoluminescence of the NC solutions, but no emission was observed when exciting at different wavelengths above the bandgap. The absorption spectra of the NC solutions are shown in Figure 4.17. Interestingly, the shape of all the absorption spectra of the alloys resembles that of pure titanium perovskite.

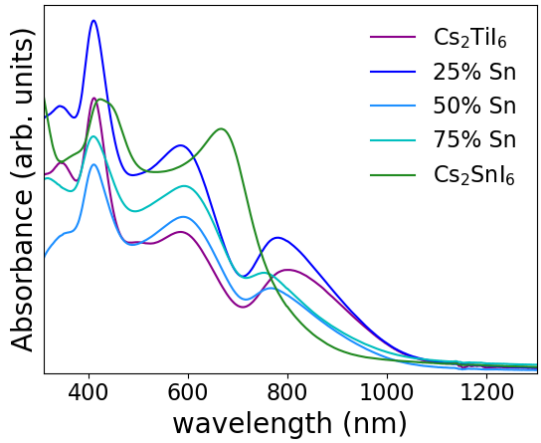

Figure 4.17: Absorption spectra of $Cs_2Ti_{1-x}Sn_xI_6$ NC solutions

In Figure 4.18 the Tauc plots of the spectra are depicted in order to determine the values of the bandgaps. We considered direct bandgap because computational studies demonstrate all these materials have quasi-direct bandgap. Cs_2SnI_6 has a bandgap at around 1.54 eV just 0.24 eV higher than Cs_2TiI_6 bandgap, which is 1.3 eV. All the mixtures have bandgaps between these two values, namely 1.33 eV, 1.36 eV and 1.4 eV, by increasing the amount of tin in the structure.

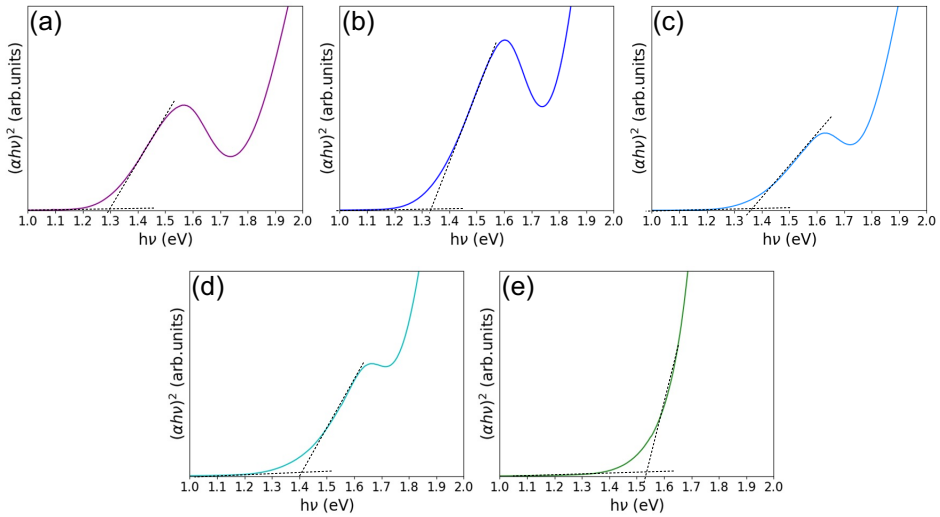

Figure 4.18: Tauc plots of $Cs_2Ti_{1-x}Sn_xI_6$ NCs with a) 0%, b) 43%, c) 64%, d) 82% and e) 100% tin in the structure

Figure 4.19(a) illustrates how the bandgap changes by increasing the percentage of tin in the structure, where the percentage is the ratio of tin over the entire amount of B component (Sn+Ti) multiplied by 100. The relation is not linear, with the mixtures having lower bandgaps than those expected in a linear behavior. This can be ascribed to the weak Sn-Ti interactions in these systems, so that Sn- and Ti- related absorption peaks do no shift significantly in energy in the mixtures. This hypothesis was confirmed by calculating the absorption spectra for the mixtures, that indeed match with the experimentally observed ones (Figure 4.19(b)).

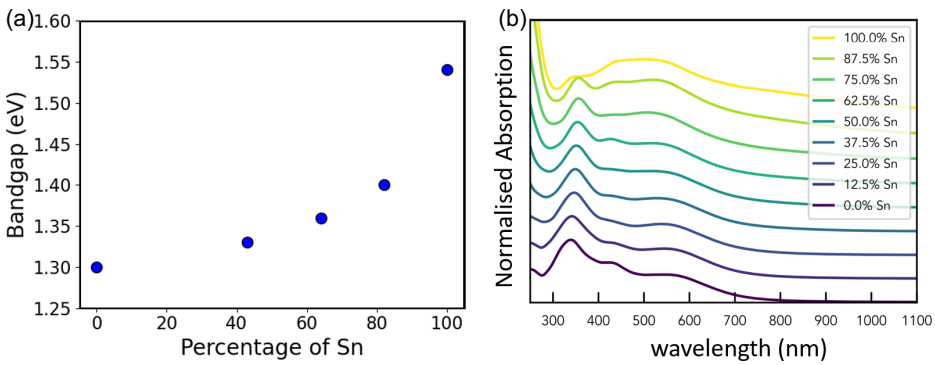

Figure 4.19: (a) Percentage of Sn in the structure vs bandgap. (b) Calculated normalized absorption spectra of $Cs_2Ti_{1-x}Sn_xI_6$ structures

4.5 Stability

The stability of the samples was investigated by examining the evolution of the diffraction peaks when the samples were exposed to air. Figure 4.20(a) shows the XRD pattern of Cs_2SnI_6 when exposed to air for days, demonstrating its high stability to oxygen exposure. On the other side, Figure 4.20(b) shows the extreme instability of Cs_2TiI_6 when exposed to air for 5 minutes in comparison with its XRD pattern under nitrogen. As expected from computational calculations, the tin perovskite is more stable in air than the titanium one.

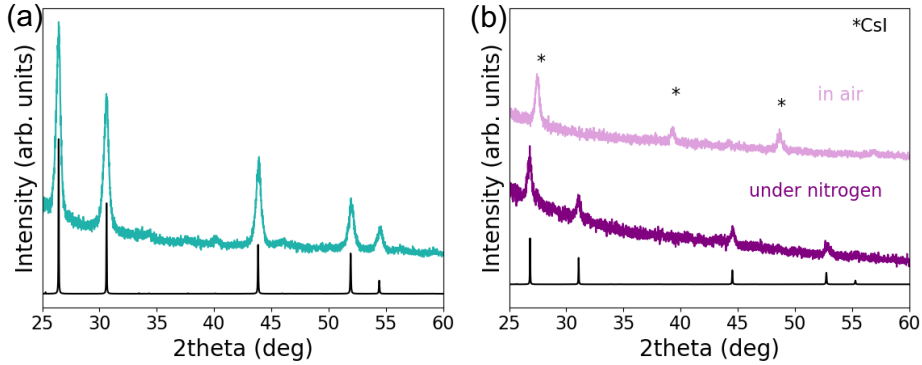

Figure 4.20: (a) XRD pattern of Cs_2SnI_6 sample when exposed to air. (b) XRD patterns of Cs_2TiI_6 under nitrogen and when exposed to air

Figure 4.21 shows the XRD patterns of the 25%, 50% and 75% Sn samples under nitrogen and when exposed to air. After few minutes in air, both samples 25% and 50% decompose and CsI diffraction peaks are visible in the pattern. In both cases, the perovskite peaks are still visible, due to the presence of stable Cs_2SnI_6 inside the sample. This indicates that these samples are not stabilized through Sn addition to the structure, or at least that the small improvement in stability cannot be observed from XRD analysis. On the other hand, Figure 4.21(c) shows the pattern of the 75% sample (corresponding to 82% from ICP-OES), which maintains some stability in air for the first 10/30 minutes, even though after 1 hour in air CsI peaks are visible. As expected, the perovskite with Sn and Ti in the structure is more stable than the one with only titanium, even though this is experimentally observed with XRD only when 82% of Ti is replaced by Sn.

Interestingly, the diffraction peaks slightly shift to lower values during decomposition in air, which indicates that the contribution of Ti in the crystal structure has decreased after air exposure (Figure 4.22).

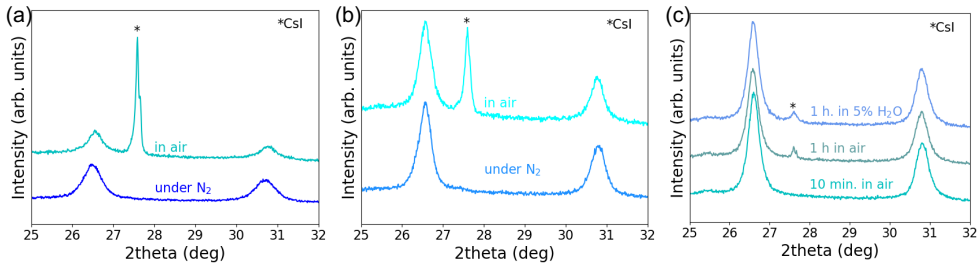

Figure 4.21: Stability in air of (a) 25% sample, (b) 50% sample and (c) 75% sample. In (c) also the stability in the 5% humidity-controlled box is showed for the 75% sample after 1 hour.

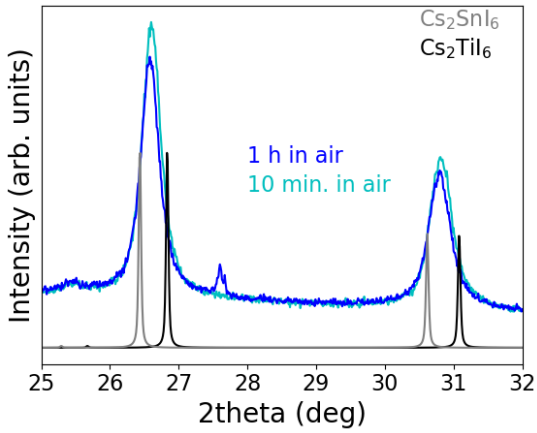

Figure 4.22: Zoom of the XRD of the 75% sample to observe the shift of the peaks after decomposition in air towards lower angles, indicative of a higher contribution of Sn in the perovskite structure

For the three samples, we followed the evolution of the perovskite peak and of the CsI peak over time from 5 minutes to 20 hours in air, taking as reference the intensity at 26.6 degrees for the perovskite peak (222) reflection and the intensity at 27.6 degrees for the CsI peak (110) reflection. Figure 4.23 illustrates the results, which indeed indicate higher stability when the percentage of tin in the structure is higher. For the 25% sample, the CsI peak is found from the first minutes of air exposure to be much more intense than the perovskite peak. The latter appears almost constant in intensity over time, suggesting the transformation of the alloy into pure tin perovskite occurred almost completely during the first minutes of air exposure. Different is the evolution of the 50% sample, which starts with CsI peak and the perovskite peak with almost the same intensity, while a fast decomposition over time can be observed. Finally, the 75% sample is the only one that does not show any CsI peak at the beginning, but still undergoes a steady decomposition.

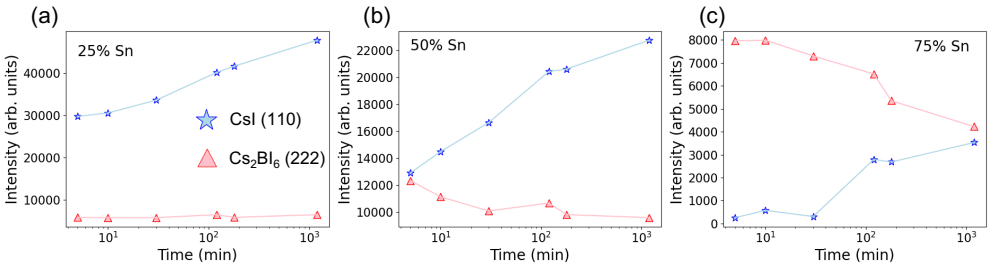

Figure 4.23: Evolution of Cs_2BI_6 (222), pink triangles, and CsI (110), blue stars, peak intensities over time in ambient atmosphere from 5 minutes to 20 hours of samples (a) 25% Sn, (b) 50% Sn and (c) 75% Sn

4.6 Conclusions

Titanium might be a suitable alternative element to replace lead in perovskites, because it is not toxic, it is an abundant element and its perovskites exist and are intrinsically stable. However, as shown in Chapter 3, cesium titanium halide perovskites suffer from high instability in air. For this reason, we searched for methods to stabilize them and we hypothesized that inserting tin in the structure could increase their stability. In this chapter, we have verified this hypothesis.

From computational studies, tin vacancy-ordered halide perovskites proved to be thermodynamically more stable than titanium vacancy-ordered perovskites under oxygen exposure. Moreover, negative free energies of mixing at room temperature were predicted for all Sn/Ti and halide compositions, which means Sn/Ti perovskites mixing is energetically favourable at room temperature.

Motivated by these computational results, we have synthesized and characterized $Cs_2Ti_{1-x}Sn_xI_6$ NCs. We observed that in order to prepare the mixtures it is important to consider the precursors' ratio used in the pure tin and pure titanium perovskite syntheses. From XRD, we have observed that the lattice parameter increases with tin addition in the structure, while mantaining the same space group symmetry.

We have studied how the morphology of Cs_2SnI_6 NCs depends on the reaction temperature, the quenching method and the amount of iodide precursor. We observed that the NCs size increases by rising the temperature of reaction from 140 °C to 200 °C and that, opposite to what observed in Chapter 3 for Cs_2TiBr_6, the quenching method does not affect the shape of Cs_2SnI_6 NCs. On the other hand, we observed that the higher is the amount of halide precursor used in the synthesis, the more the NCs coalesce forming bigger structures. Regarding the morphology of the mixtures, which are all prepared using a higher amount of iodide precursor, we observed that indeed the NCs coalesce.

Moreover, we measured a bandgap between 1.3 and 1.6 eV, going from pure titanium to pure tin perovskite. The bandgap does not change linearly with increasing amount of tin in the structure, and this behavior was confirmed computationally and it is due to the low interaction between the two B components in the 0D structure. From XRD measurements, we have observed that Cs_2SnI_6 NCs are stable in air while Cs_2TiI_6 NCs are very unstable. Moreover, by following the evolution of the diffraction peaks over time, we observed that by increasing the amount of tin in the structure, the perovskite becomes more stable.

5

Stabilization of Cs_2TiBr_6 with tin salts

5.1 Introduction

In Chapter 3 we experimentally observed that Cs_2TiBr_6 perovskite is very unstable in air. The same instability was observed by different groups in the last few years [112, 113, 133, 134, 182] and it is likely the factor that has hindered the development to more efficient PV devices based on this perovskite since 2018, when a solar cell with 3.3% efficiency was reported. [81] In the last three years, different methods, even the same used in the record efficiency paper, have been reported to prepare Cs_2TiBr_6, both as NCs and as bulk material, but in all cases the material was found to be unstable in air. Even though this indicates that the instability that we observed is not due to the larger surface area exposed to air in the NCs compared to bulk, we believe that this factor accelerates its degradation. On the other hand, the high surface area to volume ratio characterizing the NCs can be used as an advantage when it comes to improve the material's properties and stabilities through chemical treatments.

While a facile method to protect perovskite NCs from oxidation consists in embedding them in polymer matrices [183] or insulating coatings, [184, 185] these shielding materials completely block the charge transfer and therefore would not allow the application

of the NCs in PV devices. On the contrary, the functionalization of the surface with the use of short ligands, or the growth of a coating around the NCs to produce the so-called "core-shell" structure, can preserve the charge transfer while stabilizing the surface. Core-shell structures of perovskites already demonstrated increased stability in air and passivation of surface defects. [186, 187]

In Chapter 4, we reported a higher stability for the alloys of Sn and Ti iodide vacancy-ordered double perovskites. In this chapter we first present the same approach as Chapter 4 but for bromide titanium perovskites. After observing a higher stability for the mixed structures, we demonstrate a post-synthetic surface treatment with $SnBr_4$ that produces perovskite NCs with comparable stabilities.

5.2 Synthesis and characterization of Cs_2SnBr_6

Following the same procedure as in Chapter 4 for the case of $Cs_2Ti_{1-x}Sn_xI_6$, before attempting the syntheses of the bromide alloys we tried to synthesize Cs_2SnBr_6 NCs using the same method used for the preparation of Cs_2TiBr_6 NCs.

Figure 5.1 collects the characterization of the product, namely the XRD pattern to determine its structure, a TEM image to observe the morphology of the NCs, the absorption and PL spectra for the optical characterization and the X-ray Photoelectron (XPS) spectra for the elemental analysis. From XRD we observed pure Cs_2SnBr_6 without any contamination, stable in air, showing $Fm\bar{3}m$ space group symmetry, as all the vacancy-ordered double perovskites. Moreover, a lattice parameter of 10.840(3) Å was determined from Rietveld refinement. From the analysis of the TEM images, the NCs show an average length of 12 ± 2 nm. Figure 5.1(c) shows the absorption spectrum, with a peak below 350 nm, resembling the one reported in the literature, with small differences in values. From Tauc plot, which is shown later in Figure 5.4, a direct bandgap of around 3.4 eV was extracted, which falls in the range of values reported in the literature, between 2.85 and 3.78 eV. [106, 108, 127–129, 188, 189] Furthermore, an emission peak at around 400 nm was observed when exciting the sample at 320 nm. Interestingly, contrary to what reported in the literature, where either no PL or a PL peak at longer wavelengths, namely 600nm, was found for Cs_2SnBr_6, [188, 189] we measured a peak at energy just below the bandgap.

Finally, the high-resolution XPS spectra, plotted in Figure 5.1(d), indicate all the species are in the expected oxidation state, namely Cs^{+1}, Sn^{+4} and Br^{-1}. [190] From quantitative XPS analysis we calculated a ratio of Cs:Sn:Br equal to 2:1.3:5.7, close to the one of the formula. The small differences can be due to the fact that we did not consider in the calculations the different mean free passes of the electrons emitted by

the different atoms through the material.

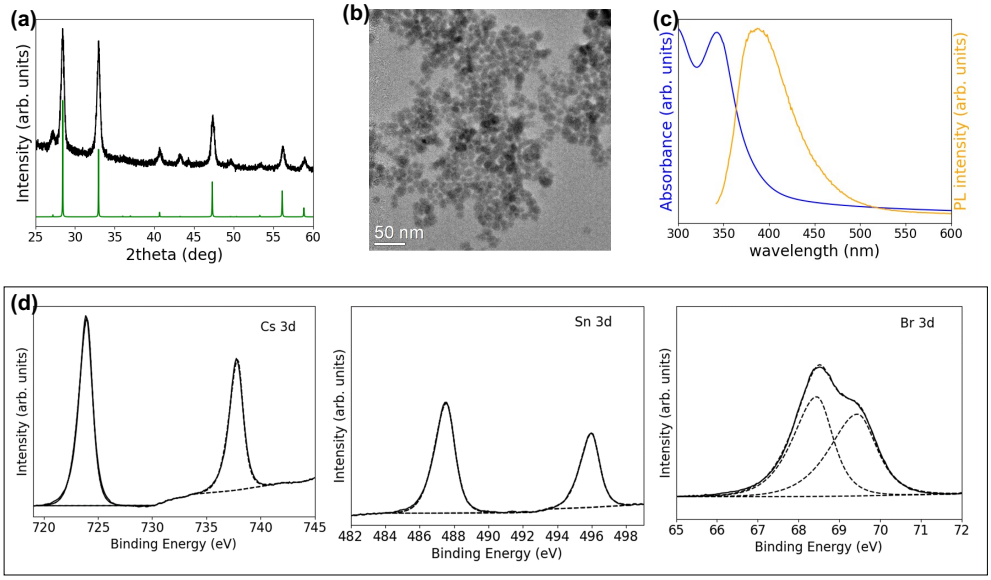

Figure 5.1: (a) XRD pattern of Cs_2SnBr_6 sample in comparison with the reference pattern, (b) TEM image of Cs_2SnBr_6 NCs, (c) absorption and PL spectra of Cs_2SnBr_6 solution and (d) high-resolution XPS spectra in the regions Cs 3d, Sn 3d and Br 3d

5.3 Synthesis and characterization of $Cs_2Ti_{1-x}Sn_xBr_6$ alloys

The syntheses of $Cs_2Ti_{1-x}Sn_xBr_6$ NCs were carried out starting from cesium oleate and different ratios of titanium (IV) isopropoxide and tin (IV) acetate dissolved in ODE and OA together with DMOP, and injecting TMSBr at 140°C. Figure 5.2 shows the XRD patterns of the products obtained from different syntheses carried out replacing different percentages of titanium precursor with tin precursor. As expected, due to the larger ionic radius of tin compared to titanium, [170] the higher the amount of tin acetate added to the precursors' solution the larger the lattice parameters, therefore the smaller the diffraction angles. The lattice parameters of all the alloys were determined from Rietveld refinement of the diffraction patterns and are reported in Table 5.1. As for the iodide case, it is evident that Sn inserts in the structure more efficiently than Ti, so that when only 50% of the titanium precursor is replaced by tin acetate, the XRD indicates that almost pure Cs_2SnBr_6 formed. As commented in Chapter 4, for the quantification of the percentage of tin in the structure, we considered the results obtained from ICP-OES analysis more reliable than those extracted from the XRD

patterns. The results, collected in Table 5.1, show that the percentage of tin replacing titanium in the structure is 90% in the 50% sample, 60% in the 30% sample, 44% in the 20% sample and 23% in the 10% sample.

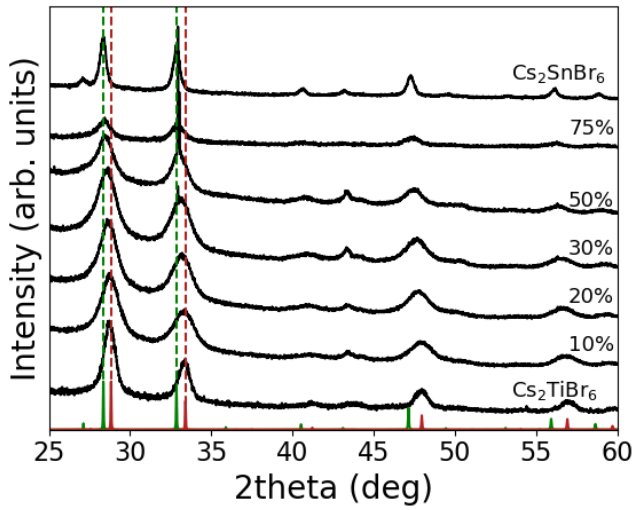

Figure 5.2: XRD patterns of pure Cs_2TiBr_6, pure Cs_2SnBr_6 and different $Cs_2Ti_{1-x}Sn_xBr_6$ alloys. The green and red patterns represent the calculated Cs_2SnBr_6 and Cs_2TiBr_6 XRD patterns, respectively, using the experimental lattice parameters

Table 5.1: X-ray, Rietveld refined lattice parameters, values of Sn% extracted from XRD using Vegard's law and measured with ICP-OES for $Cs_2Ti_{1-x}Sn_xBr_6$ alloys

Sample name	Lattice par. (Å)	XRD Sn%	ICP-OES Sn%
50%	10.831(4)	95	90
30%	10.819(6)	86	60
20%	10.800(2)	71	44
10%	10.761(5)	43	23

Figure 5.3 shows the absorption spectra of these solutions. By inserting Sn in the structure, the absorption spectra initially do not show evident differences except that the intensity of the two characteristic excitonic peaks of Cs_2TiBr_6 decrease in intensity till they completely disappear in the spectrum of the 50% sample, that, as expected, shows the characteristic peak of pure Cs_2SnBr_6 perovskite at 340 nm, which emerged already in the 30% sample.

From Tauc plots, in Figure 5.4, we observed that the bandgap virtually does not change when tuning the percentage of Sn in the sample from 0 to 60% (samples 10%, 20% and

30%), while the samples prepared with 50% and 75% of Sn precursor have bandgaps close to 3.4 eV, as expected for pure Cs_2SnBr_6.

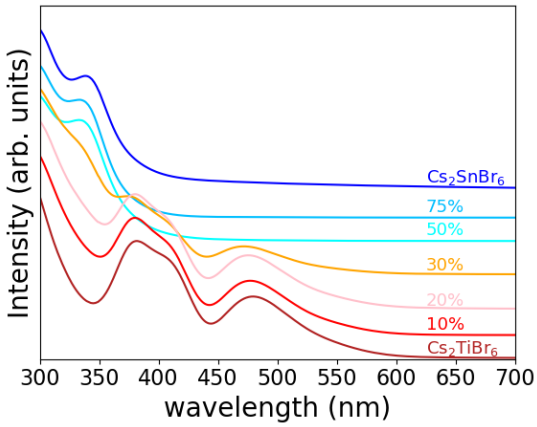

Figure 5.3: Absorption spectra of $Cs_2Ti_{1-x}Sn_xBr_6$, where the percentage on the right represent the percentage of tin that replaced titanium in the synthesis

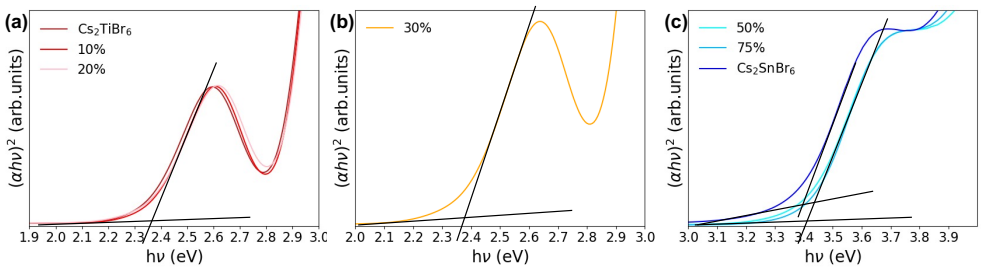

Figure 5.4: Tauc plots of $Cs_2Ti_{1-x}Sn_xBr_6$ considering direct bandgap

This non-linear behavior in the bandgap tuning when going from pure titanium to pure tin perovskite was further investigated computationally. Figure 5.5 shows the calculated absorption spectra and as observed experimentally, the low-energy absorption peaks are visible in all the samples containing titanium and just decrease in intensity the lower is its percentage in the sample. This behavior can be rationalized with the fact that in these materials the BX_6^{2-} octahedra are isolated, and therefore the B cations do not interact and, as a consequence, they maintain their distinct absorption features, as observed in Chapter 4 for $Cs_2Ti_{1-x}Sn_xI_6$ alloys. Moreover, from calculations the Ti compounds are found to have much stronger absorption intensity, which would explain the fact that the Cs_2TiBr_6 excitonic peaks are still visible in the absorption spectra of the compounds containing very low percentages of Ti.

For the alloys, we observed a very weak PL peak, close to that of Cs_2TiBr_6, at around

600 nm, which is shown in Figure 5.6 for the case of the 30% sample together with its absorption spectrum.

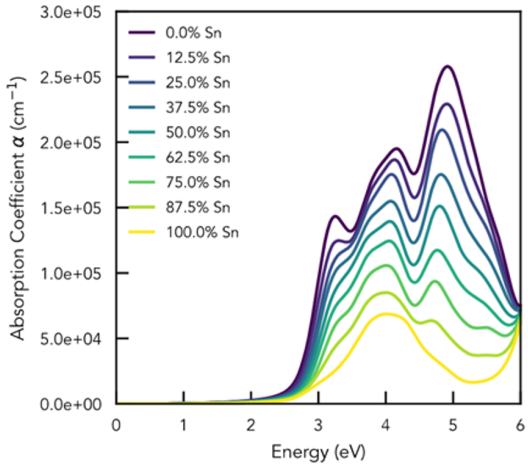

Figure 5.5: Calculated absorption spectra of $Cs_2Ti_{1-x}Sn_xBr_6$ alloys using hybrid DFT+SOC

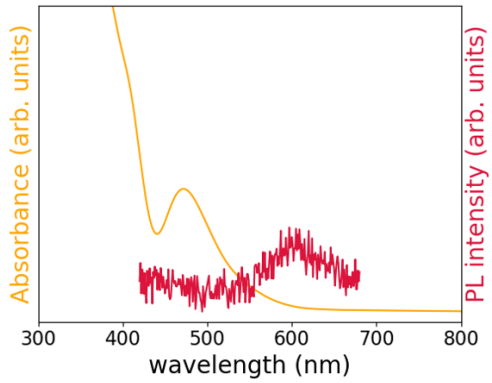

Figure 5.6: Absorption and PL spectra of the 30% alloy

After the structural and optical characterizations, we investigated the stability in air of the alloys containing up to 60% Sn. Figure 5.7 shows the decomposition of 10% and 20% alloys in air, occurring during the first minutes of air exposure. For this plot and for the next ones of this chapter, the green reference represents the positions of the diffraction peaks of Cs_2SnBr_6, the red reference those of Cs_2TiBr_6 while the grey peaks are those of the byproduct CsBr. As for the case of the $Cs_2Ti_{1-x}Sn_xI_6$ alloys, when adding small percentages of tin precursor to the initial solution, the products are unstable in air, CsBr is produced but the perovskite peaks are still visible. Due to the

small difference in lattice parameters between Sn and Ti perovskite, i.e. 10.84 Å and 10.71 Å, it is hard from XRD to evaluate if, after the decomposition, the remaining perovskite still contains some Ti in the structure or it contains only Sn while all the titanium decomposed into an amorphous compound not visible from XRD.

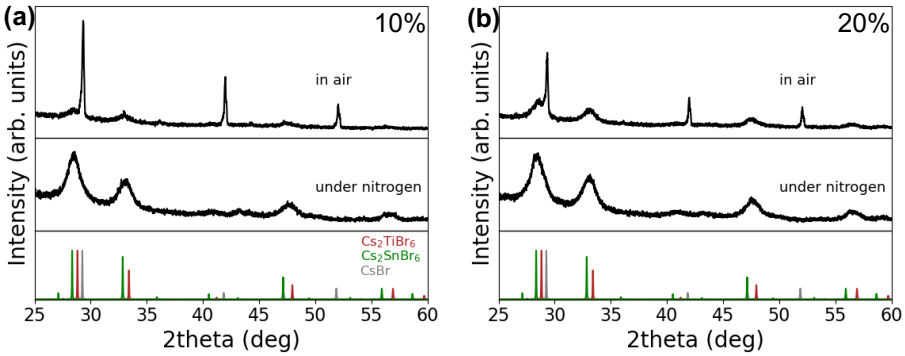

Figure 5.7: XRD patterns of 10% and 20% blends under nitrogen and in air, showing fast decomposition into CsBr in air

For the case of the alloy containing 60% Sn, a much higher stability in air was found, as shown in Figure 5.8(a). This sample is stable for several hours in air, even though we observed that the time of degradation depended on the day because of humidity variation. Therefore, in order to carry out a reproducible and comparable stability measurement we used a desiccator with 5% controlled humidity to store the samples and we observed that in these conditions this sample is stable for approximately 1 week (Figure 5.8(b)) even though after 2 weeks we could observe CsBr peaks in its diffraction pattern.

In conclusion, from these experiments we observed that adding around 60% of tin in the Cs_2TiBr_6 structure maintains a bandgap close to the one of pure titanium bromide perovskite while improving its stability. The increase in stability is very high, relative to the very low stability of Cs_2TiBr_6. Based on the knowledge that some tin in the structure stabilizes the perovskite while retaining its original bandgap, we attempted a different strategy to insert Sn in the structure. Considering that Cs_2SnBr_6 is much more stable in air than Cs_2TiBr_6, covering Cs_2TiBr_6 NCs with a Cs_2SnBr_6 layer instead of mixing the two perovskites into an alloy is supposed to be a more effective strategy in order to obtain a stable material in air. Therefore, we attempted the stabilization of Cs_2TiBr_6 NCs through surface treatment with $SnBr_4$.

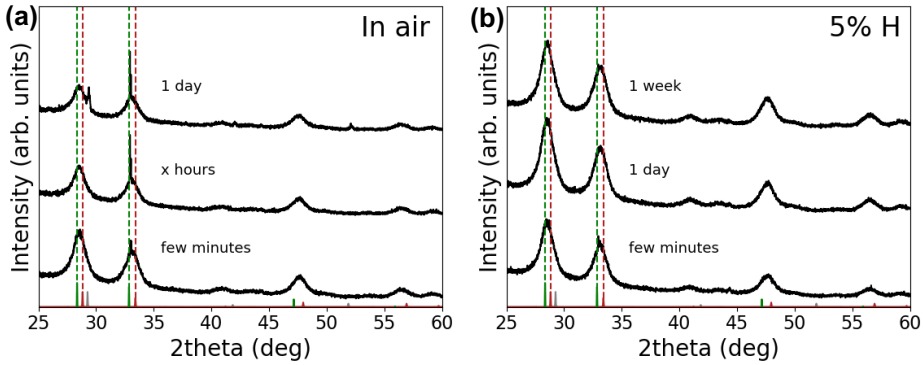

Figure 5.8: (a) XRD patterns of the 30% alloy after exposure to air and (b) its evolution when stored in a desiccator with 5% humidity (H). The narrow peak at 32.97 degrees originates from the silicon substrate

5.4 Surface treatment with $SnBr_4$

The treatment with $SnBr_4$ was carried out in the crude solution of Cs_2TiBr_6, by adding $SnBr_4$ dissolved in toluene at room temperature. The procedure was optimized in order to achieve the highest stability, by tuning the amount of $SnBr_4$ added to the solution and the time of stirring before washing the solution. The best stabilities were obtained by carrying out the reaction for 30 minutes and using 6 times the amount of $SnBr_4$ compared to the titanium contained in the treated NCs.

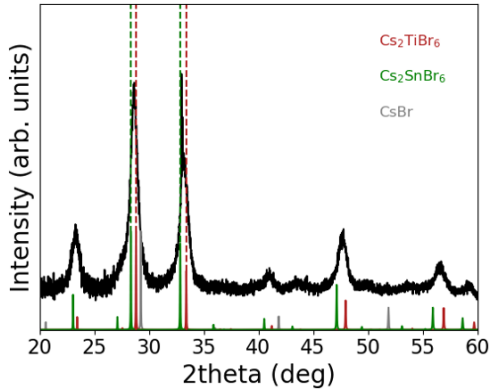

Figure 5.9: XRD pattern of $SnBr_4$-treated Cs_2TiBr_6 NCs. The narrow peak at 32.97 degrees, which overlaps with the perovskite peak, originates from the silicon substrate

Figure 5.9 shows the XRD pattern of the $SnBr_4$-treated Cs_2TiBr_6 sample, which possesses $Fm\bar{3}m$ space group symmetry, and diffraction peaks between those of Cs_2TiBr_6 and those of Cs_2SnBr_6, indicating that during the treatment Sn inserted in the structure. A lattice parameter of 10.805(4) Å is determined from Rietveld refinement of the

diffraction pattern.

Table 5.2: ICP-OES results for $SnBr_4$-treated Cs_2TiBr_6

Element	weight (mg)	atomic weight (g/mol)	mmols
Cs	5.54	132.90	0.042
Ti	0.64	47.87	0.013
Sn	1.20	118.71	0.01

ICP-OES data, listed in Table 5.2, indicate 43% of Sn and 57% of Ti, while the ratio Cs/(Sn+Ti) is 1.83, close to the expected atomic ratio in the perovskite, which is 2. This lower ratio suggests the surface is rich in B component.

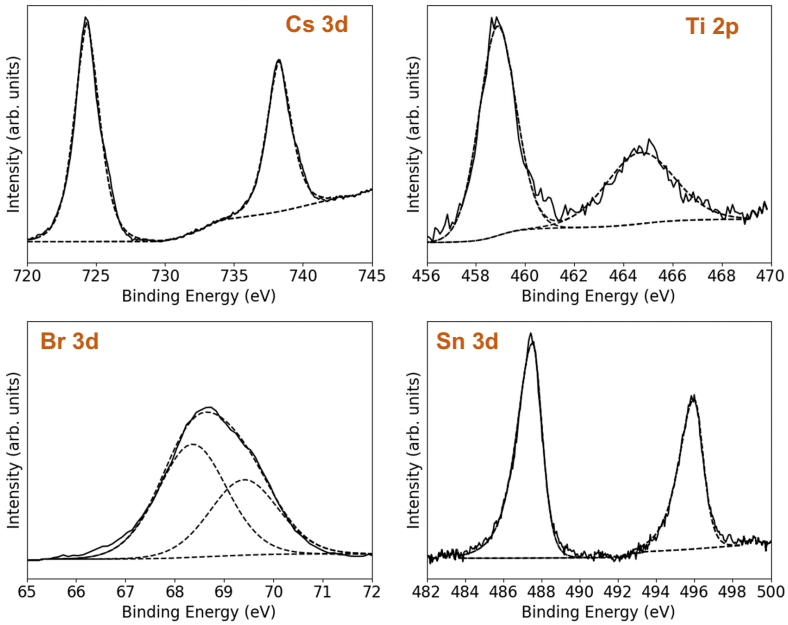

Figure 5.10: High-resolution XPS spectra of $SnBr_4$-treated Cs_2TiBr_6 sample in the region Cs 3d, Ti 2p, Br 3d and Sn 3d

XPS analysis was performed to complete the elemental analysis. The high-resolution spectra, plotted in Figure 5.10, indicate all the species are in the expected oxidation state, namely Cs^{+1}, Ti^{+4}, Sn^{+4} and Br^{-1}. Moreover, quantitative XPS analysis resulted in a ratio of Cs:Ti:Sn:Br equal to 2:1.09:0.63:5.74, indicating a slightly higher amount of titanium compared with the ICP-OES results. However, the ICP-OES data are more reliable as the XPS calculations are done without taking into account the different mean free passes of the electrons inside the material.

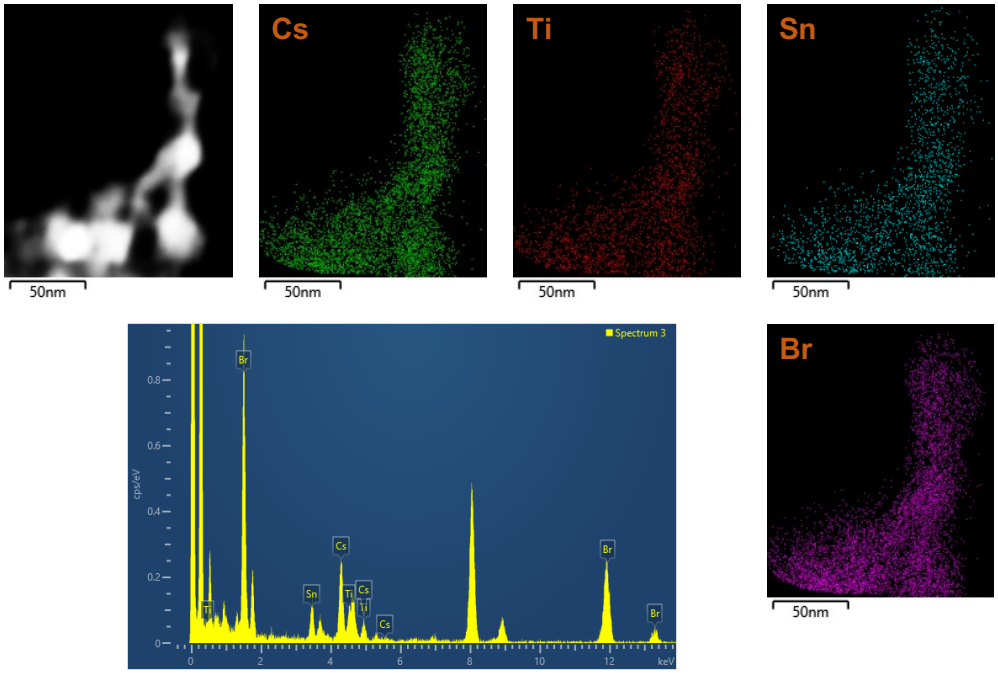

Figure 5.11: EDX High-angle annular dark-field (HAADF) image and STEM-EDX analysis of $SnBr_4$-treated Cs_2TiBr_6 NCs with the corresponding atomic maps

EDX mapping was carried out to verify the distribution of the elements in the NCs, and the results are depicted in Figure 5.11. The atomic maps show all the elements are homogenously distributed and no Sn-rich or Ti-rich regions are visible.

TEM images were taken before and after the surface treatment and are shown in Figure 5.12(a) and (d). It was observed that after the treatment the average size of the NCs increases from 9.6 nm to 11.9 nm. This treatment is carried out in the Cs_2TiBr_6 solution before washing it, so we hypothesized that this increase in radius might be due to a shell formation from $SnBr_4$ added into the solution and the Cs oleate solution left from the reaction.

Figure 5.13(a) shows the absorption of the treated NCs in solution plotted together with the absorption spectra of Cs_2TiBr_6 and Cs_2SnBr_6 in order to compare them. The spectrum of the treated sample reminds both the other two spectra, as it has a steep increase in intensity at short wavelengths, as in Cs_2SnBr_6 spectrum, but it still shows the excitonic peak of Cs_2TiBr_6 at 480 nm, more visible in Figure 5.13(b). From Tauc plot, in Figure 5.13(c), a bandgap of 2.2 eV was extracted, very close to the one of the untreated perovskite.

The photoluminescence of the $SnBr_4$-treated NC solution was also measured and is

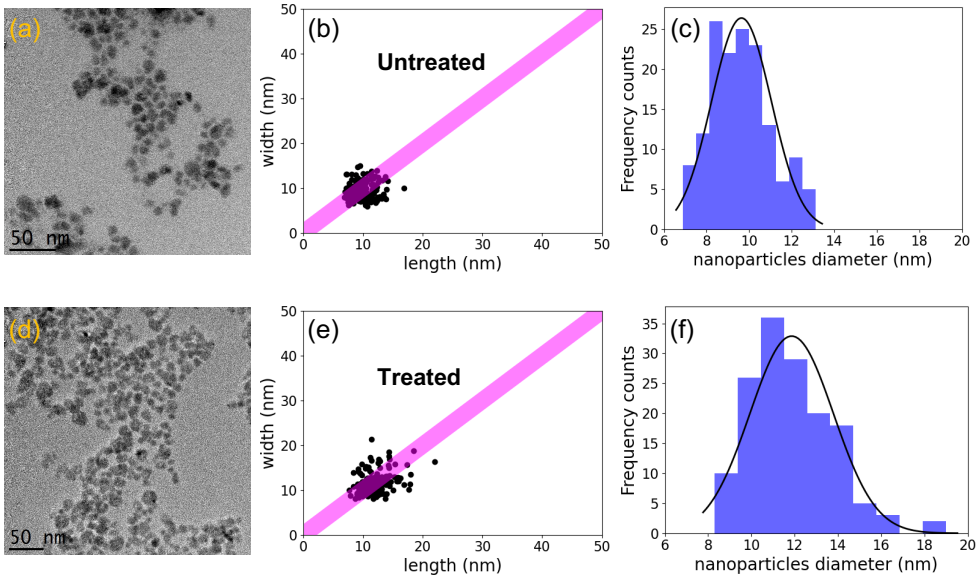

Figure 5.12: TEM images of Cs_2TiBr_6 before (a) and after (d) $SnBr_4$-treatment. (b) and (e), plots of the width vs the length of the nanoparticles, which indicate the nanoparticles are close to the symmetry. (c) and (f), histograms of the NCs diameters, calculated from the area of the NCs, indicating for the untreated sample (c) an average NC diameter of 9.6 nm, with a standard deviation of ± 1.4 nm; for the $SnBr_4$-treated sample, an average NC diameter of 11.9 nm, with a standard deviation of ± 1.9 nm

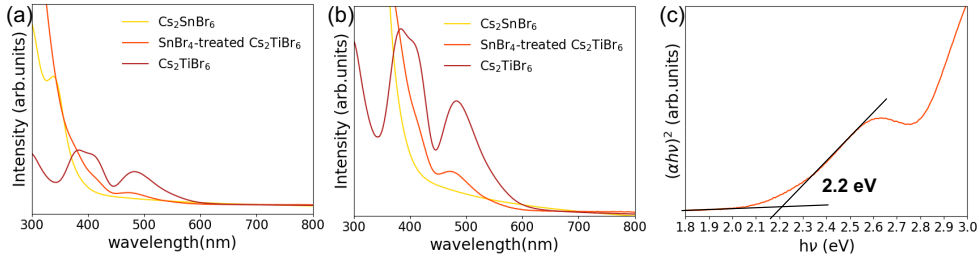

Figure 5.13: (a) Absorption spectra of $SnBr_4$-treated Cs_2TiBr_6 (orange), Cs_2TiBr_6 (bordeaux) and Cs_2SnBr_6 (yellow). (b) Zoom of (a) to observe the shape of the spectra between 400 nm and 600 nm. (c) Tauc plot of $SnBr_4$-treated Cs_2TiBr_6 absorption spectrum

plotted together with the absorption spectrum in Figure 5.14. As for the case of pure Cs_2TiBr_6, the intensity of the emission was extremely low. The peak is centered at 594 nm, very close to the peak of untreated Cs_2TiBr_6 that was found at 580 nm, but at lower energy.

The stability of the sample was investigated by monitoring the evolution of the XRD peaks when the samples were exposed to air and when stored in a desiccator with

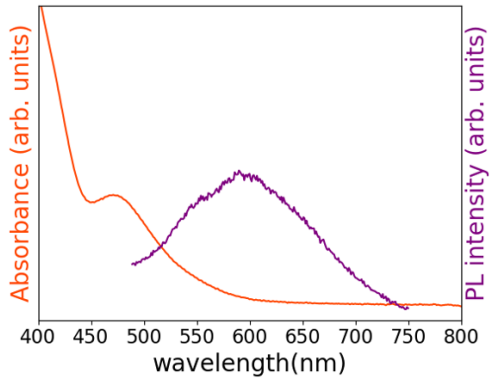

Figure 5.14: Absorption spectrum (in orange) and PL emission (in purple) of $SnBr_4$-treated Cs_2TiBr_6 NC solution

controlled 5% humidity, as for the 30% alloy. Figure 5.15(a) shows the perovskite is stable for some hours in air while after 1 day the CsBr peak at 29.3 degrees already emerges in the diffraction pattern. On the other hand, when storing it in the desiccator (Figure 5.15(b)), the sample is stable for 1 week, as observed for the 30% alloy, while after 2 weeks CsBr peaks were observed in the diffraction pattern.

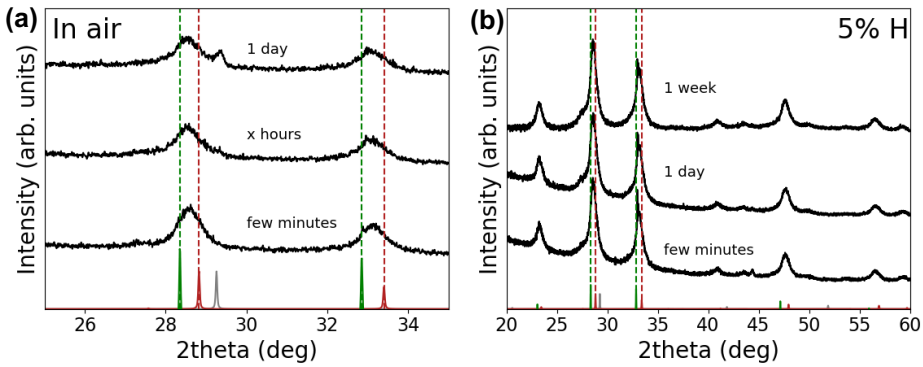

Figure 5.15: Evolution of the XRD pattern of the $SnBr_4$-treated Cs_2TiBr_6 sample (a) after exposure to air and (b) when stored in a desiccator with 5% humidity (H). The narrow peak at 32.97 degrees, which overlaps with the perovskite peak in (b) originates from the silicon substrate

By comparing the XRD of this sample with the ones of the alloys, we observe that the treated sample has a stability comparable to that of the 30% sample but contains a lower amount of tin, closer to that of the 20% sample, which on the contrary was unstable in air. Therefore we hypothesized that the treated NCs have a kind of core-shell structure in which the Sn content gradually decreases going from the surface to the center of the NC.

In order to verify this hypothesis, EDX mapping with a spatial resolution high enough to observe the position of the atoms in the NCs should be used. Another option would be to calculate the exact mean free passes of the electrons of each atom and then compare the XPS results with the ICP-OES ones.

5.5 Conclusions

In this chapter we have investigated two different methods to increase the stability of Cs_2TiBr_6 NCs with tin addition in the structure. The first one is the synthesis of alloyed structures with formula $Cs_2Ti_{1-x}Sn_xBr_6$, and the second one is the surface treatment of Cs_2TiBr_6 with $SnBr_4$.

First, we have demonstrated that Cs_2SnBr_6 can be prepared using a similar hot-injection method as the one developed for Cs_2TiBr_6. For its characterization, we performed a structural, morphological, optical and elemental analysis.

Secondly, we have achieved the syntheses of the alloys containing tin and titanium in different ratios. We have observed that tin inserts in the structure more easily that titanium so that when mixing tin and titanium precursors in the same concentration, only tin is found in the structure from XRD measurements. Moreover, we have compared the experimental absorption spectra with the computed ones and found that they are in agreement. Finally, we have observed that a certain percentage of tin, above 60%, in the structure increases the stability of the perovskite in air, and that the stability is even higher when storing the samples in a desiccator.

In the last part of the chapter, we have demonstrated that a room temperature treatment of Cs_2TiBr_6 NCs with $SnBr_4$ produces a structure that contains around 43% of tin and that shows a stability in air comparable to that of the alloy with 60% of tin in its structure. We have carried out a full characterization of this product and hypothesized that the tin is not distributed homogenously in this NC structure but that its concentration gradually decreases from the surface to the center of the NC. This would explain its stability in air, which is comparable to that of the alloys composed by a higher amount of tin.

6

Summary

Perovskites are the only solution-processed materials that outperformed multicrystalline and thin-film silicon when applied in solar cells and for this reason are considered one of the most interesting materials in the world of new generation PVs. However, they contain lead that hinders their commercialization because it is considered a threat for the environment and for human beings due to its toxicity. Titanium is an abundant element in the earth's crust, it is nontoxic and its perovskites are intrinsically stable so it is a potential alternative element to replace lead in the perovskite structure.

In this thesis, we investigated the properties of titanium perovskites and developed a novel solution process to synthesize them. Moreover, we replaced partially and fully the titanium with tin in the structure and studied the properties of these alloys.

In **Chapter 2**, the differences between the 3D structure of archetypal perovskites and the 0D structure of the vacancy-ordered double perovskites containing tin and titanium have been outlined. By comparing experiments with computational results, we found that, contrary to common perovskites, dispersion interactions play a fundamental role in these materials. Moreover, we demonstrated that Cs_2SnCl_6 and Cs_2TiCl_6 can be prepared using a hot injection method and that both materials are stable in air.

The synthesis of Cs_2TiBr_6 was reported in **Chapter 3**. We found that it is necessary to use an excess of Ti and Br precursors in order to avoid the formation of byproducts. The same result was observed for all the halide titanium perovskites. Furthermore, we replaced the commonly-used primary amine with a zwitterionic ligand containing a quartenary amminic group because we observed degradation of the perovskite when in contact with primary amines. While the shape of the NCs does not change when using only OA or a combination of OA and DMOP, in the latter case the solution in more stable during the washing step. Finally, we found that quenching the reaction with dilution in toluene is an effective method to stop the growth of the NCs, while the most frequently used ice/water bath does not work, since the reaction occurs also at lower temperatures, at which anisotropic NCs form.

In chapter 3, we also demonstrated that by partially or fully replacing the bromide precursor with the analogue iodide precursor all the mixed and pure halide-$Cs_2TiBr_{6-x}I_x$ perovskites can be prepared. The bandgap decreases with increasing amounts of iodide in the structure, following the common trend observed for all perovskites.

Finally, we observed fast decomposition in air for all these perovskites, which motivated us to look for solutions to stabilize them.

In **Chapter 4**, we report an increase in stability when adding tin in the structure of Cs_2TiI_6. We first study the synthesis of Cs_2SnI_6 and how the synthetic parameters affect the morphology of the NCs. We then demonstrate the synthesis of mixed tin/titanium $Cs_2Ti_{1-x}Sn_xI_6$ and characterize the mixtures structurally, chemically and optically. Finally, we observe that the mixture with the higher amount of tin in the structure has the highest stability in air.

In **Chapter 5**, we reported two different methods to improve the stability of Cs_2TiBr_6 in air through the addition of tin in the structure. First, we synthesized and characterized Cs_2SnBr_6 NCs. Afterwards, we demonstrated the preparation of the mixed tin/titanium $Cs_2Ti_{1-x}Sn_xBr_6$ perovskites using the same method. For the alloy with 60% of tin in the structure, we observed a considerable increase in stability compared to the pure titanium perovskite. Lastly, we reported a room temperature surface-treatment using $SnBr_4$ on Cs_2TiBr_6 NCs, which produced a material with a stability comparable to that of the alloy.

Overall, this thesis provides an insight into novel lead-free perovskites based on titanium and tin and it represents a milestone for the understanding and development of this new class of materials.

Appendices

A

Experimental section of Chapter 2

Chemicals. Cesium acetate (CsAc 99.9% trace metals basis), titanium(IV) isopropoxide ($Ti(O\text{-}i\text{-}Pr)_4$, 97.0%), oleic acid (OA, technical grade 90%), bromotrimethylsilane (TMSBr, 97%), chlorotrimethylsilane (TMSCl, 99%), 3-(N,N-dimethyloctadecylammonio) propanesulfonate (DMOP, 99.0%) and acetone (99.5%) were purchased from Sigma-Aldrich. Tin(IV) acetate ($SnAc_4$, 98%) and iodotrimethylsilane (TMSI, 97%) were purchased from Fischer Scientific. Toluene (anhydrous, 99.8%) was purchased from Scharlabs. 1-Octadecene (90%) was purchased from Alfa Aesar. All chemicals were used without any further purification.

Preparation of cesium oleate solution. Cesium oleate was prepared following a previously reported method. [181] 0.768 g (4 mmol) of cesium acetate were loaded in a 50 ml three-neck flask together with 7.56 ml of oleic acid and 18.72 ml of octadecene. The solution was degassed through 3 cycles of argon and vacuum and heated at 110 °C for 30 minutes under argon. Afterwards, the solution was left under vacuum for 3 hours at 110°C. The as-prepared solution was stored under nitrogen. The final concentration was calculated by measuring the final volume of the solution and by considering the moles of titanium precursor used in the synthesis.

Preparation of titanium oleate solution. For the synthesis of the titanium oleate solution, 16 ml of oleic acid were loaded in a 50 ml three-neck flask and degassed through 3 cycles of argon and vacuum. 2 ml of titanium (IV) isopropoxide taken from the glovebox were slowly added while stirring and the solution was heated under argon for 1 hour at 140°C. Afterwards, the solution was left under vacuum at 110°C overnight and acquired a dark red tone. The as-prepared solution was stored under nitrogen. The final concentration was calculated by measuring the final volume of the solution and by considering the moles of titanium precursor used in the synthesis.

Synthesis of Cs_2SnX_6 NCs. For the synthesis of the Cs_2SnI_6 NCs, 112.8 mg of Sn(IV) acetate (0.31 mmol) and 60 mg of DMOP were weighed in the glovebox and loaded in a 50 ml three-neck flask together with 4 ml of the cesium oleate solution (0.62 mmol), 2 ml of octadecene and 2 ml of oleic acid. The solution was degassed through 3 cycles of argon and vacuum and heated at 110 °C for 35 minutes under vacuum. At this point, 273 μL of TMSI (1.86 mmol) was injected under argon at 140 °C and the reaction was carried out for 20 seconds and then quenched by diluting the solution with 10 ml of toluene.

Cs_2SnCl_6 and Cs_2SnBr_6 NCs were prepared by following the above procedure except that the Cs:Sn:X precursors ratio used was 2:2:9 instead of 2:1:6, which means that 225.6 mg (0.62 mmol) of Sn acetate were weighted and 360 μL (2.8 mmol) of TMSCl, in the case of Cs_2SnCl_6 NCs, and 380 μL (2.8 mmol) of TMSBr, in the case of Cs_2SnBr_6, were injected.

Synthesis of Cs_2TiX_6 NCs. For the synthesis of Cs_2TiBr_6 and Cs_2TiI_6, 4 ml of cesium oleate (0.625 mmol) and 60 mg of DMOP were weighed in the glovebox and loaded in a 50 ml three-neck flask together with 2 ml of octadecene, 2 ml of oleic acid and 1.85 ml of titanium oleate solution (0.78 mmol). The solution was degassed through 3 cycles of argon and vacuum treatment and heated at 110 °C for 35 minutes under vacuum. At this point, for the case of Cs_2TiBr_6 synthesis, 574 μL (4.218 mmol) of TMSBr was injected under argon at 140 °C and the reaction was carried out for 20 seconds and then quenched by diluting the solution with 15 ml of toluene. For the case of Cs_2TiI_6, 1.238 ml (8.436 mmol) of TMSI was needed to prepare pure Cs_2TiI_6. Cs_2TiCl_6 was prepared with the same method, but a higher amount of halide precursor was needed, namely 2.4 ml of TMSCl, while DMOP ligand was not used in the synthesis.

Washing of the NC solutions. For the case of the Cs_2SnX_6 and Cs_2TiBr_6 NC solutions, the first washing was carried out by adding 5 ml of acetone as an antisolvent to 5 ml of solution already diluted in toluene and centrifuging at 5800 rpm for 10

minutes, while for the Cs_2TiI_6 and Cs_2TiCl_6 NC solutions no antisolvent was added before centrifuging. The supernatant was discarded and the precipitate redispersed in 3 ml of toluene and centrifuged again at 5800 rpm for 10 minutes. The supernatant was discarded again and the precipitate redispersed in toluene and centrifuged again at 2000 rpm for 4 minutes to remove possible aggregates. Finally, the supernatant was filtered using a 0.22 μm PTFE filter. The solutions were stored under inert atmosphere.

UV-vis absorption. Optical absorption spectra were collected using a Varian Cary5000 UV-vis-NIR spectrophotometer. When measuring the absorption below 300 nm, the nanocrystals were dispersed in hexane instead of toluene. For the case of Cs_2SnCl_6, since the nanocrystals were not stable in hexane, they were deposited on a sapphire substrate and the absorption was measured using an internal DRA 2500 integrating sphere.

X-ray Diffraction (XRD) characterization. XRD patterns were collected using a Rigaku SmartLab diffractometer in Bragg-Brentano $\Theta/2\Theta$ geometry, Cu kα radiation (wavelength=1.5406 Å) and a D/teX Ultra 250 silicon strip detector. The NC samples were prepared by drop casting the nanocrystals' solutions on the top of a silicon wafer.

Lattice parameters were determined from Rietveld refinement of the diffraction patterns. The table below collects the space group, lattice parameter, weighted-profile R-factor (Rwp) and goodness of fit (χ^2) values for Cs_2SnCl_6 and Cs_2TiCl_6 perovskites.

Table A.1: Rietveld refinement parameters for Cs_2SnCl_6 and Cs_2TiCl_6 samples

Material	Space Group	a = b = c/Å	Rwp(%)	χ^2
Cs_2SnCl_6	$Fm\bar{3}m$	10.381(6)	8.75	1.37
Cs_2TiCl_6	$Fm\bar{3}m$	10.253(13)	12.12	0.97

B

Experimental section of Chapter 3

Chemicals. Cesium acetate (CsAc 99.9% trace metals basis), titanium (IV) isopropoxide (Ti(O-i-Pr)$_4$, 97.0%), oleic acid (OA, technical grade 90%), bromotrimethylsilane (TMSBr, 97%), 3-(N,N-dimethyloctadecylammonio) propanesulfonate (DMOP, 99.0%) and acetone (99.5%) were purchased from Sigma-Aldrich. Iodotrimethylsilane (TMSI, 97%) was purchased from Fischer Scientific. Toluene (anhydrous, 99.8%) was purchased from Scharlabs. 1-octadecene (90%) was purchased from Alfa Aesar. All chemicals were used without any further purification.

Preparation of titanium oleate solution. The preparation of the titanium oleate solution has been described in Appendix A.

Synthesis of $Cs_2TiBr_{6-x}I_x$ nanocrystals. 120 mg of cesium acetate (0.625 mmol) and 60 mg of DMOP were weighted in the glovebox and loaded in a 50 ml three-neck flask together with 2 ml of octadecene, 2 ml of oleic acid and 1.85 ml of titanium oleate solution (0.78 mmol). The solution was degassed through 3 cycles of argon and vacuum and heated at 110°C for 35 minutes under vacuum. At this point, for the case of Cs_2TiBr_6 synthesis, 574 μL (4.218 mmol) of TMSBr, were injected under argon at 140°C and the reaction carried out for 20 seconds and then quenched by diluting

the solution with 15 ml of toluene. For the case of Cs_2TiI_6, 1238 μL (8.436 mmol) of TMSI were needed to prepare pure Cs_2TiI_6. For the mixed halide perovskite synthesis, different amounts of TMSBr and TMSI were mixed in the glovebox and injected in the flask, taking into account the optimal moles for the two pure halide perovskites syntheses. For instance, for the 70% synthesis, 70% of the iodide precursor used in the pure iodide perovskite synthesis were mixed with 30% of the bromide precursor used in the pure bromide perovskite synthesis. For the case of Cs_2TiBr_6 and mixed-halide perovskites NCs solutions, the washing procedure was carried out adding to 5 ml of solution already diluted in toluene, 5 ml of acetone as antisolvent and centrifuging at 5800 rpm for 10 minutes, while for Cs_2TiI_6 NCs solution, no antisolvent was added before centrifuging. The supernatant was discarded and the precipitate redispersed in 1 ml of toluene and centrifuged again at 1000 rpm for 2 minutes to remove possible aggregates. The supernatant was filtered using a 0.22 μm PTFE filter. The solutions were stored in the fridge.

X-ray Diffraction (XRD) characterization. XRD patterns were collected using a Rigaku SmartLab diffractometer in Bragg-Brentano $\Theta/2\Theta$ geometry, Cu kα radiation (wavelength=1.5406 Å) and a D/teX Ultra 250 silicon strip detector. The NCs samples were prepared by drop casting the nanocrystals' solutions on the top of a silicon wafer. All the samples were measured inside an air-sensitive sample holder, which was loaded in the glovebox to avoid any contact with air.

Lattice parameters were determined from Rietveld refinement of the diffraction patterns. The table below collects the space group, lattice parameter, weighted-profile R-factor (Rwp) and goodness of fit (χ^2) values for Cs_2TiBr_6 and Cs_2TiI_6 perovskites.

Table B.1: Rietveld refinement parameters for Cs_2TiBr_6 and Cs_2TiI_6 samples

Material	Space Group	a = b = c/Å	Rwp(%)	χ^2
Cs_2TiBr_6	$Fm\bar{3}m$	10.706(3)	10.11	2.75
Cs_2TiI_6	$Fm\bar{3}m$	11.468(5)	5.90	7.28

Transmission Electron Microscopy (TEM) characterization and elemental analysis. TEM measurements were performed at the Scientific and Technological Centres of the University of Barcelona (CCiT-UB). HRTEM images were acquired in a JEOL J2010F TEM microscope, equipped with a field emission electron gun (FEG). EDXS experiments were carried out in a JEOL J2100 TEM microscope, equipped with a LaB_6 thermionic filament, and using an Oxford Instruments INCA X-sight spectrometer with Si (Li) detector. Both microscopes were operated at an accelerating voltage of 200 kV. Samples for TEM characterization were prepared in the glovebox

by drop-casting diluted toluene solutions (50 μL of NCs solution in 1 ml of toluene) onto 200 mesh carbon-coated copper grids.

ICP-OES measurements were performed at the Scientific and Technological Centres of the University of Barcelona (CCiT-UB). Elemental analysis of the samples was carried out using an ICP-OES PerkinElmer, model Optima 3200RL, in standard conditions. The digestion of the sample necessary for this measurement was carried out by adding to the dry NCs obtained from 2.5 ml of the washed solution, 6 ml of HNO_3, 2 ml of H_2O_2, 1 ml of HF and deionized water, and heating the solution at 210 °C at high pressure in a microwave digestion system "Milestone EthosOne".

UV-vis Absorption and PL measurements. Optical absorption spectra were collected using a Varian Cary-5000 UV-vis-NIR spectrophotometer. Photoluminescence (PL) measurements were performed using a Horiba Jobin Yvon iHR550 Fluorolog system, with a OXXIUS 405 nm continuous wave laser as the source. The PL spectra were corrected for the system response function.

C

Experimental section of Chapter 4

Chemicals. Cesium acetate (CsAc 99.9% trace metals basis), titanium (IV) isopropoxide ($Ti(O\text{-}i\text{-}Pr)_4$, 97.0%), oleic acid (OA, technical grade 90%), 3- (N,N-dimethyl octadecylammonio) propanesulfonate (DMOP, 99.0%) and acetone (99.5%) were purchased from Sigma-Aldrich. Tin (IV) acetate ($SnAc_4$ 98%) and iodotrimethylsilane (TMSI, 97%) were purchased from Fischer Scientific. Toluene (anhydrous, 99.8%) was purchased from Scharlabs. 1-octadecene (90%) was purchased from Alfa Aesar. All chemicals were used without any further purification.

Preparation of cesium oleate solution. The preparation of the cesium oleate solution has been described in Appendix A.

Synthesis of $Cs_2Ti_{1-x}Sn_xI_6$ NCs.

Synthesis of Cs_2SnI_6. For the synthesis of Cs_2SnI_6 NCs, 112.8 mg of Sn(IV)acetate (0.31 mmol) and 60 mg of DMOP were weighed in the glovebox and loaded in a 50 ml three-neck flask together with 4 ml of the cesium oleate solution (0.62 mmol), 2 ml of octadecene and 2 ml of oleic acid. The solution was degassed through 3 cycles of argon and vacuum and heated at 110 °C for 35 minutes under vacuum. At this point, 273μL of TMSI (1.86 mmol) was injected under argon at 140 °C and the reaction

was carried out for 20 seconds and then quenched by diluting the solution in 10 ml of toluene.

Synthesis of Cs_2TiI_6. Cs_2TiI_6 was prepared following the procedure described in the experimental section of chapter 3, but cesium oleate was used instead of cesium acetate. Briefly, 4 ml of cesium oleate (0.62 mmol) and 60 mg of DMOP were weighted in the glovebox and loaded in a 50 ml three-neck flask together with 2 ml of octadecene, 2 ml of oleic acid and 1.85 ml of titanium oleate solution (0.78 mmol). The solution was degassed through 3 cycles of argon and vacuum and heated at 110°C for 35 minutes under vacuum. At this point 1238 μL (8.436 mmol) of TMSI were injected and after 20 seconds the reaction was quenched by diluting the solution in 10 ml of toluene.

Synthesis of $Cs_2Ti_{1-x}Sn_xI_6$. Mixed titanium-tin iodide perovskites were prepared using the same method used for the preparation of pure tin and pure titanium perovskite nanocrystals. 4 ml of cesium oleate and 60 mg of DMOP were loaded in a 50 ml three-neck flask together with Sn(IV)acetate and Ti(IV)isopropoxide in different ratio, 2 ml of octadecene and 2 ml of oleic acid. The solution was degassed through 3 cycles of argon and vacuum and heated at 110°C for 35 minutes under vacuum. At this point 1238 μL (8.436 mmol) of TMSI were injected and after 20 seconds the reaction was quenched by diluting the solution in 10 ml of toluene.

Washing of the NCs. In the first step of the washing procedure, 5 ml of methylacetate was added as antisolvent to 5 ml of all the NC solutions except for the case of pure titanium perovskite, which does not need the addition of an antisolvent to precipitate during centrifugation and that decomposes into a whitish product in case of addition of it. The solutions were centrifuged at 5800 rpm for 10 minutes. Afterwards, the supernatant was discarded and the black precipitate was redispersed in 4 ml of toluene. The solution was centrifuged again at 5800 rpm for 10 minutes and the supernatant again discarded while the precipitate redispersed in 3 ml of toluene. Finally, the solution was centrifuged at 1400 rpm for 4 minutes to remove possible aggregates and the supernatant was filtered using a 0.22 μm PTFE filter. The solutions were stored under inert atmosphere.

X-ray Diffraction (XRD) characterization. XRD patterns were collected using a Rigaku SmartLab diffractometer in Bragg-Brentano $\Theta/2\Theta$ geometry, Cu kα radiation (wavelength=1.5406 Å) and a D/teX Ultra 250 silicon strip detector. The NCs samples were prepared by drop casting the nanocrystals' solutions on the top of a silicon wafer. For the characterization, all the samples were measured inside an air-sensitive sample holder, which was loaded in the glovebox to avoid any contact with air, while for the stability study, they were exposed to air.

Lattice parameters were determined from Rietveld refinement of the diffraction patterns. The table below collects the space group, lattice parameter, weighted-profile R-factor (Rwp) and goodness of fit (χ^2) values for $Cs_2Ti_{1-x}Sn_xI_6$ perovskites.

Table C.1: Rietveld refinement parameters for $Cs_2Ti_{1-x}Sn_xI_6$ samples

Material	Space Group	a = b = c/Å	Rwp(%)	χ^2
Cs_2SnI_6	$Fm\bar{3}m$	11.6786(10)	6.45	1.44
25% Sn	$Fm\bar{3}m$	11.537(4)	5.96	2.52
50% Sn	$Fm\bar{3}m$	11.5730(14)	8.05	1.64
75% Sn	$Fm\bar{3}m$	11.594(5)	7.89	1.53

Transmission Electron Microscopy (TEM) characterization. TEM measurements were performed at the Scientific and Technological Centres of the University of Barcelona (CCiT-UB). TEM images were acquired in a JEOL J2010F TEM microscope, equipped with a field emission electron gun (FEG). EDXS experiments were carried out in a JEOL J2100 TEM microscope, equipped with a LaB_6 thermionic filament, and using an Oxford Instruments INCA X-sight spectrometer with Si (Li) detector. Both microscopes were operated at an accelerating voltage of 200 kV. Samples for TEM characterization were prepared in the glovebox by drop-casting diluted toluene solutions (50 μL of NCs solution in 1 ml of toluene) onto 200 mesh carbon-coated copper grids.

ICP-OES measurements. ICP-OES measurements were performed at the Scientific and Technological Centres of the University of Barcelona (CCiT-UB). Elemental analysis of the samples was carried out using an ICP-OES PerkinElmer, model Optima 3200RL, in standard conditions. The digestion of the sample necessary for this measurement was carried out by adding to the dry NCs obtained from 2.5 ml of the washed solution, 6 ml of HNO_3, 2 ml of H_2O_2, 1 ml of HF and deionized water, and heating the solution at 210 °C at high pressure in a microwave digestion system "Milestone EthosOne".

UV-vis Absorption and PL measurements. Optical absorption spectra were collected using a Varian Cary-5000 UV-vis-NIR spectrophotometer. Photoluminescence (PL) measurements were performed using a Horiba Jobin Yvon iHR550 Fluorolog system, with an OXXIUS 405 nm continuous wave laser as the source or, when exciting at different wavelengths, a tungsten lamp with a monochromator to set different excitation wavelengths.

D

Supplementary Data for Chapter 5

Chemicals. Cesium acetate (CsAc 99.9% trace metals basis), titanium (IV) isopropoxide (Ti(O-i-Pr)4, bromotrimethylsilane (TMSBr, 97%), tin (IV) bromide ($SnBr_4$, 99%), oleic acid (OA, technical grade 90%), 3-(N,N-dimethyloctadecylammonio) propanesulfonate (DMOP, 99.0%) and acetone (99.5%) were purchased from Sigma-Aldrich. Tin (IV) acetate ($SnAc_4$ 98%) was purchased from Fischer Scientific. Toluene (anhydrous, 99.8%) was purchased from Scharlabs. 1-octadecene (90%) was purchased from Alfa Aesar. All chemicals were used without any further purification.

Synthesis of $Cs_2Ti_{1-x}Sn_xBr_6$ NCs 4 ml of cesium oleate and 60 mg of DMOP were loaded in a 50 ml three-neck flask together with Sn(IV) acetate and Ti(IV) isopropoxide in different ratio (while the total Cs:B ratio was kept 2:2.5), 2 ml of ODE and 2 ml of OA. The solution was degassed through 3 cycles of argon and vacuum and heated at 110°C for 35 minutes under vacuum. At this point, 574 μL (4.218 mmol) of TMSBr were injected and after 20 seconds the reaction was quenched by diluting the solution in 10 ml of toluene. For the washing procedure, 5 ml of acetone were added to 5 ml of solution very slowly to avoid aggregation of the NCs and the solution was centrifuged at 5800 rpm for 10 minutes. Afterwards, the supernatant was discarded and the NCs

redissolved in toluene.

Treatment with $SnBr_4$. The treatment with $SnBr_4$ was carried out using a solution of $SnBr_4$ dissolved in toluene (for the best stabilities, 103.86 mg were dissolved in 2 ml of toluene) that was slowly added to 2.5 ml of the crude solution of Cs_2TiBr_6 after its quenching. After 30 minutes (the optimized time) stirring, 1 ml of acetone was added to the solution and this was centrifuged at 5800 rpm for 10 minutes. The supernatant was removed and the NCs redispersed in 1 ml of toluene. For this treatment, Cs_2TiBr_6 solution was prepared following the procedure described in Appendix B, except that cesium oleate was used instead of cesium acetate.

X-ray Diffraction (XRD) characterization. XRD patterns were collected using a Rigaku SmartLab diffractometer in Bragg-Brentano $\Theta/2\Theta$ geometry, Cu kα radiation (wavelength=1.5406 Å) and a D/teX Ultra 250 silicon strip detector. The NCs samples were prepared by drop casting the nanocrystals' solutions on the top of a silicon wafer. For the characterization, all the samples were measured inside an air-sensitive sample holder, which was loaded in the glovebox to avoid any contact with air, while for the stability study, they were exposed to air.

Lattice parameters were determined from Rietveld refinement of the diffraction patterns. The table below collects the space group, lattice parameter, weighted-profile R-factor (Rwp) and goodness of fit (χ^2) values for $Cs_2Ti_{1-x}Sn_xBr_6$ perovskites and for the $SnBr_4$-treated Cs_2TiBr_6 sample.

Table D.1: Rietveld refinement parameters for $Cs_2Ti_{1-x}Sn_xBr_6$ and $SnBr_4$-treated Cs_2TiBr_6 samples

Material	Space Group	a = b = c/Å	Rwp(%)	χ^2
Cs_2SnBr_6	$Fm\bar{3}m$	10.840(3)	7.57	1.81
10% Sn	$Fm\bar{3}m$	10.761(5)	3.35	1.56
20% Sn	$Fm\bar{3}m$	10.800(2)	3.53	1.78
30% Sn	$Fm\bar{3}m$	10.819(6)	4.34	2.92
50% Sn	$Fm\bar{3}m$	10.831(4)	5.79	4.75
$SnBr_4$-treated Cs_2TiBr_6	$Fm\bar{3}m$	10.805(4)	6.01	2.19

Transmission Electron Microscopy (TEM) characterization. TEM measurements were performed at the Scientific and Technological Centres of the University of Barcelona (CCiT-UB). TEM images were acquired in a JEOL J2010F TEM microscope, equipped with a field emission electron gun (FEG). EDXS experiments were carried out in a JEOL J2100 TEM microscope, equipped with a LaB_6 thermionic filament, and using an Oxford Instruments INCA X-sight spectrometer with Si (Li) detector.

Both microscopes were operated at an accelerating voltage of 200 kV. Samples for TEM characterization were prepared in the glovebox by drop-casting diluted toluene solutions onto 200 mesh carbon-coated copper grids.

ICP-OES measurements. Elemental analysis of the sample was carried out using an ICP-OES PerkinElmer, model Optima 3200RL, in standard conditions. The digestion of the sample necessary for this measurement was carried out by adding to the dry NCs, 6 ml of HNO_3, 2 ml of H_2O_2, 1 ml of HF and deionized water, and heating the solution at 210 °C at high pressure in a microwave digestion system "Milestone EthosOne".

XPS measurements and analysis of XPS spectra. The samples for XPS were prepared on substrates of gold vapor-deposited on glass, by spin coating 40 μL of solution at 1000 rpm in the glovebox.

XPS measurements were performed at the Institut Català de Nanociencia i Nanotecnologia (ICN2) using a Phoibos 150 analyser (SPECS) under ultra-high vacuum conditions (base pressure of 4 x 10^{-10} mbar) equipped with a monochromatic Al kα X-ray source (1486.74 eV). The pass energy value used was 20 eV for the high-resolution spectrum. The samples were transferred very fast from a nitrogen atmosphere to the XPS setup under vacuum, though they were exposed to air for few seconds.

All the spectra were "charge-corrected" moving the main carbon peak at 284.8 eV. When identifying the chemical species from the position of the peaks, we used a Perkin-Elmer Corporation XPS handbook. [190]

UV-vis Absorption and PL measurements. Optical absorption spectra were collected using a Varian Cary-5000 UV-vis-NIR spectrophotometer. Photoluminescence (PL) measurements were performed using a Horiba Jobin Yvon iHR550 Fluorolog system, with an OXXIUS 405 nm continuous wave laser as the source or, when exciting at different wavelengths, a tungsten lamp with a monochromator to set different excitation wavelengths.

E

Characterization methods

E.1 Morphological and Structural Characterizations

E.1.1 Transmission Electron Microscopy (TEM)

As opposed to optical microscopes that use photons as illumination source, a transmission electron microscope uses a high voltage electron beam to visualize specimens, in order to obtain a higher spatial resolution as a consequence of the smaller wavelengths of the accelerated electrons compared to those of photons. Thanks to this higher resolution, it is possible to observe the size and the shape of NCs and also the atoms' planes, which could not be imaged with optical microscopes. In order to obtain such electrons with small wavelength, TEMs employ a high voltage, in our experiments 200 kV, since the higher is the voltage, the higher will be the resolution of the microscope. The accelerated electrons travel through a vacuum tube in which electromagnetic and electrostatic lenses focus them into a fine beam that passes through the sample. The transmitted electrons hit a fluorescent screen at the bottom of the microscope that creates the final image. This is the technique used to study the morphology of the NCs, i.e. their size distribution and their shapes. Finally, with this technique used in high

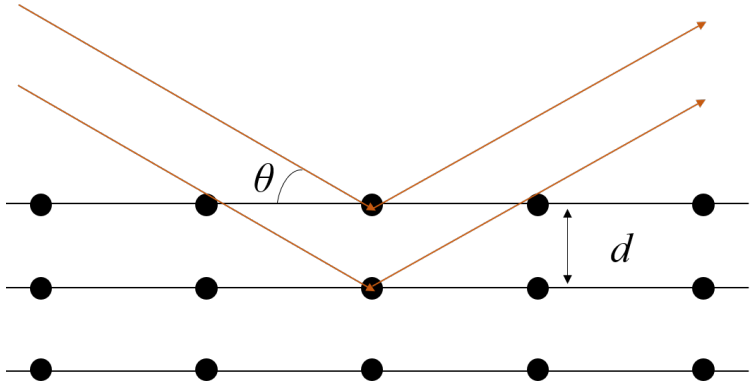

Figure E.1: Representation of the diffraction of X-rays by the arrays of atoms in a crystal. Two beams with the same wavelength are scattered by two different atoms within a solid. Two lower beam travels an extra length of 2dsinθ. Constructive interference occurs when this length is equal to the wavelength of the radiation or to an integer of it

resolution, it is possible to visualize the planes of the atoms composing the NCs, to confirm the crystal structure extracted from XRD patterns.

E.1.2 X-ray diffraction (XRD)

X-ray diffraction is an experimental technique used to determine the structure of a crystal from the way a beam of incident X-rays is diffracted by the crystal at different incident angles. It relies on the elastic scattering of the X-ray beam by the electrons of the atoms forming regular arrays inside the crystals. Indeed, the electrons scatter the X-rays in all directions but the diffracted X-ray waves interfere constructively only at certain directions, indicated as angles, while in the others they cancel each other. These angles depend on the distance between the arrays of atoms in a way described by the Bragg's equation:

$$n\lambda = 2dsin\theta$$

in which λ is the wavelength of the X-ray beam, d is the spacing between diffracting planes in the crystal, θ is the incident angle and n is any integer (Figure E.1).

Therefore, by knowing the angles of diffraction it is possible to extract the distances between the crystals' planes, with smaller angles indicating larger interplanar spacings. Knowing all the angles of diffraction and the intensities of the diffraction peaks, the crystallographic structure of the material can be determined.

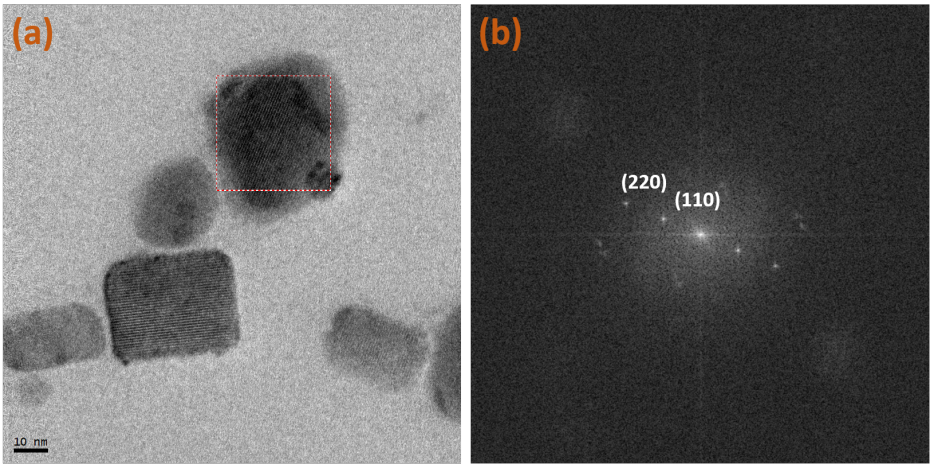

Figure E.2: (a) HRTEM image of Cs_2TiBr_6 NCs, where the dashed red square indicates the area that was processed. (b) FFT processed image, where the 2 points represent the planes (220) and (110) in reciprocal space

E.1.3 Fast-Fourier Transform analysis

This analysis can be applied to High-Resolution TEM images when the planes of atoms are clearly visible in the images. It gives a representation of the crystal in reciprocal space, where the interplanar spacings are easier to identify by measuring the distance from the centre to each of the points, which represent a specific plane of atoms that were visible in the unprocessed image.

An example of an FFT processed HRTEM image, extracted from the morphological study of Cs_2TiBr_6, is shown in Figure E.2.

E.2 Chemical Characterizations

E.2.1 Energy Dispersive X-Ray Spectroscopy (EDX)

EDX is a technique used for the elemental analysis of the samples, which is operated in the scanning transmission electron microscope (STEM) in order to obtain also a spatially-resolved analysis. This technique is based on the fundamental fact that each element is characterized by its unique atomic structure that will produce a specific emission spectrum when excited. In this measurement, the electron beam in the TEM excites the inner shell electrons of the atoms that are subsequently ejected and, as a consequence, electrons in the outer-shell relax into the electron holes, releasing X-rays. The released X-rays are detected by an energy-dispersive spectrometer, and as the difference in energy between an outer-shell electron and an inner-shell electron is

specific for each element, from the spectral analysis it is possible to determine which elements emitted those X-rays.

We used this technique to demonstrate the presence of all the elements composing the perovskite NCs and their distribution in the samples, while the quantitative analysis was carried out using ICP-OES. The data demonstrating the presence of each element in the samples were given as maps of each element's distribution, which is the reason why we used this technique in STEM. In addition, high-angle annular dark field (HAADF) images were taken by detecting the high angle incoherently scattered electrons in order to provide an image of the NCs that overlaps with the elemental maps.

E.2.2 Inductively Coupled Plasma Optical Emission Spectroscopy (ICP-OES)

ICP-OES is the only technique used to determine the absolute concentration of the metals composing the perovskite NCs in solution and their relative ratios. In this technique, the NCs are first digested in acid till the metals that compose them are completely dissolved into deionized water. Later, these metals are ionized and excited by a plasma so that they emit light at wavelengths specific for each element. From the wavelengths of emission and the intensities of the signals it is possible to identify which are the metals inside the sample and their amounts. Compared to XPS and EDX, this is the only technique that provide data on the bulk compositions instead of surface or spatially-resolved ones.

E.2.3 X-Ray Photoelectron Spectroscopy (XPS)

X-ray Photoelectron Spectroscopy (XPS) is a powerful elemental technique used to detect chemical species on the surface of a sample. It gives information not only on which elements are present in the first nanometers of the films, but more interestingly, about their oxidation states and chemical environment. Moreover, it is possible to quantitatively analyse the spectra in order to have information about the amount of each species in their specific chemical states. In this analysis, a soft X-ray beam (usually Al Kα X-rays, with E_{photon} = 1486.7 eV) hits the sample, exciting the core electrons of the atoms that are emitted with a specific energy that depends on the energy of the X-ray beam and on their binding energy. These emitted electrons are then collected by an "electron collector" in which an electromagnetic field bends them depending on their kinetic energy. At the end of the electron collector, the electrons reach a phosphorous screen at different positions, depending on to what extent they have been bended. A CCD camera records the position at which the phosphorous screen

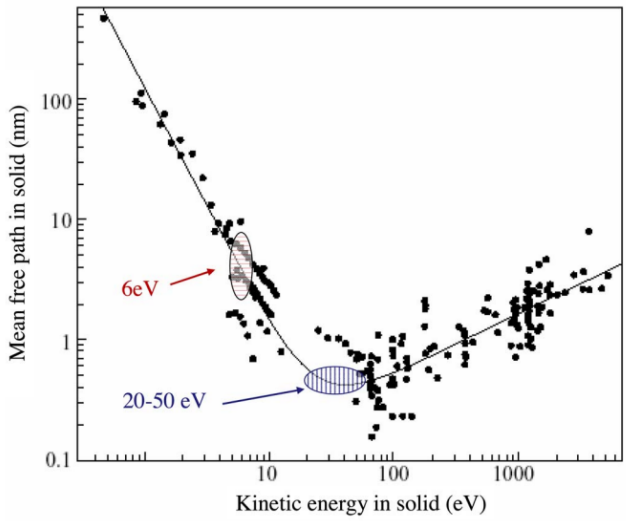

Figure E.3: The "universal curve" for surface sensitivity in photoemission, taken from. [192] Electron inelastic mean free paths from a variety of materials are plotted vs the kinetic energy relative to E_F

shines after absorption of the electrons, and from this position the kinetic energy of the emitted electron is calculated. Core electrons have their specific energy for each atom and therefore, by knowing the binding energy of the electrons in the sample, it is possible to know which species are present in the sample. Moreover, when the chemical environment changes, the bonding energy of the electrons slightly shifts to higher or lower energies, and it is from these small energy shifts that is possible to distinguish between different chemical states. XPS spectroscopy is a surface sensitive technique because the electrons that are emitted from the atoms can travel only few nanometers before being absorbed again by other atoms in the sample. Indeed, the electron inelastic mean free path lengths in solids is of the order of few nanometers [191] and depends on the material and on the kinetic energy of the electrons, as shown in Figure E.3.

E.3 Optical Characterizations

E.3.1 UV-vis absorption spectroscopy

Since all the materials synthesized in this thesis have a bandgap in the UV-Vis range, their optical properties were analyzed using UV-vis absorption spectrophotometry, from which their optical bandgaps were extracted together with the analyses of the absorption shapes, discussed in Chapter 2. The principle of this technique relies on irradiating the sample with light of a known wavelength and measuring how much of

this light is absorbed by the sample. The UV-vis spectrophotometer used for all the measurements carried out in this thesis is a CARY 5000 UV-vis-NIR spectrophotometer that uses two lamps as light source, namely a deuterium arc lamp for the UV range and a tungsten halogen lamp for the visible range, has a monochromator to select single wavelengths during the scan and detects the light transmitted through the samples with a PbSmart NIR detector. When measuring samples in solution, the measurement was performed in transmission mode, using very diluted and well dispersed samples. On the other hand, when measuring samples as thin films, an integrating sphere was used and the absorption (A) was calculated from reflectance (R) and transmittance (T) measurements and using the following law:

$$A = 1 - R - T$$

Where A, R and T are all normalized by the amount of incident flux.

In order to calculate the optical bandgaps of the samples, Tauc plots were used to analyze the optical spectra. In a Tauc plot, the energy, hν (eV), is represented in the abscissa while the (Ahν)1/r values are shown in the ordinate, where A is the absorption, and r depends on the kind of transition represented, when direct r=1/2, when indirect r=2.

E.3.2 Photoluminescence spectroscopy

Photoluminescence (PL) spectroscopy consists in irradiating the sample with a specific wavelength with energy above the bandgap to stimulate the emission from the sample, which will occur at longer wavelengths. The experiments in this thesis were performed using a Horiba Jobin Yvon iHR550 Fluorolog system, with an OXXIUS 405 nm continuous wave laser or a tungsten halogen lamp combined with a monochromator, when using different excitation wavelengths.

For Cs_2TiBr_6 NCs, relative photoluminescence quantum yield (PLQY) measurements were carried out, where PLQY is defined as the number of photons emitted by the sample over the number of photons absorbed. The relative measurement was done following the method described in. [193] We used Rhodamine 6G in absolute ethanol as PLQY standard (PLQY = 95%), and excited at 480 nm, which is the shortest wavelength at which the standard value is valid. The Rhodamine 6G solution was prepared in a concentration higher than 2 x 10^{-4} M, which is the lowest concentration at which its PLQY is concentration independent.

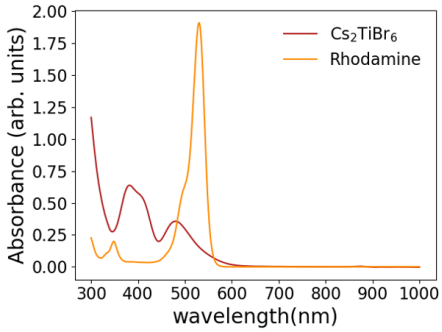

Figure E.4: Absorption spectra of Cs_2TiBr_6 NCs solution and Rhodamine 6G standard

In order to measure the relative PLQY yield we used the following formula:

$$\Phi_{f,x} = \Phi_{f,st} \times \frac{F_x}{F_{st}} \times \frac{f_{st}(\lambda_{ex})}{f_x(\lambda_{ex})} \times \frac{n_x^2(\lambda_{em})}{n_{st}^2(\lambda_{em})}$$

Where x is the sample, st is the standard, F is the integral photon flux, f is the absorption factor, and n is the refractive index of the solvents where the sample and the standard are dissolved. Finally, the absorption factor is defined as

$$f(\lambda_{ex}) = 1 - 10^{-A(\lambda_{ex})}$$

Figure E.4 shows the absorption of the sample and of the standard solutions, using a 1mm thick cuvette. From this plot we took the values of the absorbance at 480 nm, which is the excitation wavelength for the PL measurement, and we calculated the absorption factor f for the standard and for the sample.

Afterwards, we measured the PL intensity of the sample and of the standard with the same conditions (except the integration time), and their spectra are shown in Figure E.5.

We calculated the integral photon fluxes emitted from the sample and from the standard by calculating the area under the PL curves. Table E.1 summarizes the values of the absorption intensities of the samples at 480 nm, the absorption factors, the photon

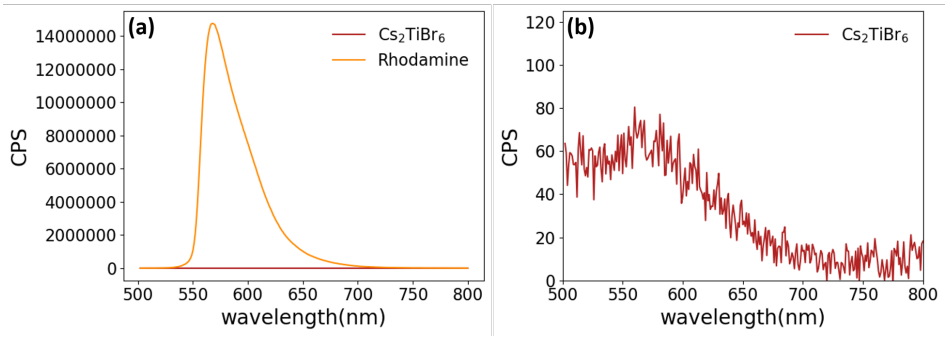

Figure E.5: Absorption spectra of Cs_2TiBr_6 NCs solution and Rhodamine 6G standard

fluxes, the refractive indexes of ethanol and toluene, the standard PLQY for Rhodamine 6G and the calculated PLQY of Cs_2TiBr_6. We calculated the relative PLQY of the sample, which is equal to 0.001.

This result is consistent with the fact that all the papers published so far on Cs_2TiBr_6 failed in measuring the PLQY, except one, [111] where they claim that the measured PLQYs are "much less than 1%", even though they do not give any information about the experimental method used.

Table E.1: Optical results and data for relative PLQY measurement of Cs_2TiBr_6 using Rhodamine 6G standard

	A (480 nm)	f (480 nm)	F	n (λ_{em})	PLQY
Rhodamine	0.28	0.47	723303749.5	1.36	95
Cs_2TiBr_6	0.36	0.56	8002.5	1.5	0.001

Bibliography

[1] IPCC Working Group III, *Summary for Policymakers. In: Climate Change 2022: Mitigation of Climate Change. Contribution of Working Group III to the Sixth Assessment Report of the Intergovernmental Panel on Climate Change*. Cambridge University Press, Cambridge, UK and New York, NY, USA, 2022. (see p. 1)

[2] J. C. Goldschmidt, L. Wagner, R. Pietzcker, and L. Friedrich, "Technological learning for resource efficient terawatt scale photovoltaics," *Energy and Environmental Science*, vol. 14, pp. 5147–5160, 10 2021. (see p. 1)

[3] N. M. Haegel, H. Atwater, T. Barnes, C. Breyer, A. Burrell, Y. M. Chiang, S. D. Wolf, B. Dimmler, D. Feldman, S. Glunz, J. C. Goldschmidt, D. Hochschild, R. Inzunza, I. Kaizuka, B. Kroposki, S. Kurtz, S. Leu, R. Margolis, K. Matsubara, A. Metz, W. K. Metzger, M. Morjaria, S. Niki, S. Nowak, I. M. Peters, S. Philipps, T. Reindl, A. Richter, D. Rose, K. Sakurai, R. Schlatmann, M. Shikano, W. Sinke, R. Sinton, B. J. Stanbery, M. Topic, W. Tumas, Y. Ueda, J. V. D. Lagemaat, P. Verlinden, M. Vetter, E. Warren, M. Werner, M. Yamaguchi, and A. W. Bett, "Terawatt-scale photovoltaics: Transform global energy improving costs and scale reflect looming opportunities," *Science*, vol. 364, pp. 836–838, 2019. (see p. 1)

[4] N. M. Haegel, R. Margolis, T. Buonassisi, D. Feldman, A. Froitzheim, R. Garabedian, M. Green, S. Glunz, H. M. Henning, B. Holder, I. Kaizuka, B. Kroposki, K. Matsubara, S. Niki, K. Sakurai, R. A. Schindler, W. Tumas, E. R. Weber, G. Wilson, M. Woodhouse, and S. Kurtz, "Terawatt-scale photovoltaics: Trajectories and challenges," *Science*, vol. 356, pp. 141–143, 4 2017. (see p. 1)

[5] F. Creutzig, P. Agoston, J. C. Goldschmidt, G. Luderer, G. Nemet, and R. C. Pietzcker, "The underestimated potential of solar energy to mitigate climate change," *Nature Energy*, vol. 2, 8 2017. (see p. 1)

[6] IEA, *Solar PV*. 2022. (see p. 2)

[7] IEA, *Net Zero by 2050.* 2021. (see p. 2)

[8] W. Shockley and H. J. Queisser, "Detailed balance limit of efficiency of p-n junction solar cells," *Journal of Applied Physics*, vol. 32, pp. 510–519, 1961. (see p. 2)

[9] A. Polman and H. A. Atwater, "Photonic design principles for ultrahigh-efficiency photovoltaics," *Nature Materials*, vol. 11, pp. 174–177, 3 2012. (see p. 2)

[10] NREL, "Best research-cell efficiency," 2022. (see pp. 2 and 4)

[11] J. Werner, F. Sahli, F. Fu, J. J. D. Leon, A. Walter, B. A. Kamino, B. Niesen, S. Nicolay, Q. Jeangros, and C. Ballif, "Perovskite/perovskite/silicon monolithic triple-junction solar cells with a fully textured design," *ACS Energy Letters*, vol. 3, pp. 2052–2058, 9 2018. (see p. 2)

[12] K. Xiao, J. Wen, Q. Han, R. Lin, Y. Gao, S. Gu, Y. Zang, Y. Nie, J. Zhu, J. Xu, and H. Tan, "Solution-processed monolithic all-perovskite triple-junction solar cells with efficiency exceeding 20%," *ACS Energy Letters*, vol. 5, pp. 2819–2826, 9 2020. (see p. 2)

[13] S. Rahmany and L. Etgar, "Semitransparent perovskite solar cells," *ACS Energy Letters*, vol. 5, pp. 1519–1531, 5 2020. (see p. 3)

[14] S. Lie, A. Bruno, L. H. Wong, and L. Etgar, "Semitransparent perovskite solar cells with $>$ 13% efficiency and 27% transperancy using plasmonic au nanorods," *ACS Applied Materials and Interfaces*, vol. 14, pp. 11339–11349, 3 2022. (see p. 3)

[15] H. J. Snaith, "Perovskites: The emergence of a new era for low-cost, high-efficiency solar cells," *Journal of Physical Chemistry Letters*, vol. 4, pp. 3623–3630, 11 2013. (see p. 3)

[16] D. Weber, "$CH_3NH_3PbX_3$, ein Pb(II)-system mit kubischer perowskitstruktur," *Z. Naturforsch*, vol. 33, pp. 1443–1445, 1978. (see p. 3)

[17] D. Weber, "$CH_3NH_3SnBr_xI_{3-x}$ (x = 0-3), ein Sn(II)-system mit kubischer perowskitstruktur," *Z. Naturforsch*, vol. 33, pp. 862–865, 1978. (see p. 3)

[18] D. Mitzi, C. Feild, W. T. A. Harrison, and A. M. Guloy, "Conducting tin halides with a layered organic-based perovskite structure," *Nature*, vol. 369, pp. 467–469, 1994. (see p. 4)

[19] D. B. Mitzi, S. Wang, C. A. Feild, C. A. Chess, and A. M. Guloy, "Conducting layered organic-inorganic halides containing (110)-oriented perovskite sheets," *Science*, vol. 267, pp. 1473–1476, 1995. (see p. 4)

[20] A. Kojima, K. Teshima, Y. Shirai, and T. Miyasaka, "Organometal halide perovskites as visible-light sensitizers for photovoltaic cells," *Journal of the American Chemical Society*, vol. 131, pp. 6050–6051, 5 2009. (see p. 4)

[21] H.-S. Kim, C.-R. Lee, J.-H. Im, K.-B. Lee, T. Moehl, A. Marchioro, S.-J. Moon, R. Humphry-Baker, J.-H. Yum, J. E. Moser, M. Gratzel, and N.-G. Park, "Lead iodide perovskite sensitized all-solid-state submicron thin film mesoscopic solar cell with efficiency exceeding 9%," *Scientific Report*, vol. 2, pp. 1–7, 2012. (see p. 4)

[22] J.-H. Im, J. Chung, S.-J. Kim, and N.-G. Park, "Synthesis, structure, and photovoltaic property of a nanocrystalline 2h perovskite-type novel sensitizer $(CH_3CH_2NH_3)PbI_3$, volume = 7, year = 2012,," *Nanoscale Research Letters*, pp. 1–7. (see p. 4)

[23] M. M. Lee, J. Teuscher, T. Miyasaka, T. N. Murakami, and H. J. Snaith, "Efficient hybrid solar cells based on meso-superstructured organometal halide perovskites," *Science*, vol. 338, pp. 643–647, 11 2012. (see p. 4)

[24] L. Etgar, P. Gao, Z. Xue, Q. Peng, A. K. Chandiran, B. Liu, M. K. Nazeeruddin, and M. Grätzel, "Mesoscopic $CH_3NH_3PbI_3/TiO_2$ heterojunction solar cells, volume = 134, year = 2012,," *Journal of the American Chemical Society*, pp. 17396–17399, 10. (see p. 4)

[25] M. Liu, M. B. Johnston, and H. J. Snaith, "Efficient planar heterojunction perovskite solar cells by vapour deposition," *Nature*, vol. 501, pp. 395–398, 2013. (see p. 4)

[26] M. A. Green, A. Ho-Baillie, and H. J. Snaith, "The emergence of perovskite solar cells," *Nature Photonics*, vol. 8, pp. 506–514, 2014. (see p. 4)

[27] Q. Dong, Y. Fang, Y. Shao, P. Mulligan, J. Qiu, L. Cao, and J. Huang, "Electron-hole diffusion lengths > 175 μm in solution-grown $CH_3NH_3PbI_3$ single crystals," *Science*, vol. 347, pp. 967–970, 2 2015. (see p. 4)

[28] Y. Bi, E. M. Hutter, Y. Fang, Q. Dong, J. Huang, and T. J. Savenije, "Charge carrier lifetimes exceeding 15 μs in methylammonium lead iodide single crystals," *Journal of Physical Chemistry Letters*, vol. 7, pp. 923–928, 3 2016. (see p. 4)

[29] L. Protesescu, S. Yakunin, M. I. Bodnarchuk, F. Krieg, R. Caputo, C. H. Hendon, R. X. Yang, A. Walsh, and M. V. Kovalenko, "Nanocrystals of cesium lead halide perovskites ($CsPbI_3$, X = Cl, Br, and I): Novel optoelectronic materials showing bright emission with wide color gamut," *Nano Letters*, vol. 15, pp. 3692–3696, 2015. (see pp. 4, 5, 22, and 25)

[30] P. Walter, E. Welcomme, P. Hallégot, N. J. Zaluzec, C. Deeb, J. Castaing, P. Veyssière, R. Bréniaux, J. L. Lévêque, and G. Tsoucaris, "Early use of PbS nanotechnology for an ancient hair dyeing formula," *Nano Letters*, vol. 6, pp. 2215–2219, 10 2006. (see p. 4)

[31] S. Padovani, C. Sada, and P. Mazzoldi, "Copper in glazes of renaissance luster pottery: Nanoparticles, ions, and local environment," *Journal of Applied Physics*, vol. 93, pp. 10058–10063, 2003. (see p. 4)

[32] T. W. Odom, "Printable stained glass," *Nature Nanotechnology*, vol. 7, pp. 550–551, 2012. (see p. 4)

[33] M. Faraday, "The bakerian lecture: Experimental relations of gold (and other metals) to light," *Philosophical Transactions of the Royal Society of London*, vol. 147, pp. 145–181, 1857. (see p. 4)

[34] L. Brus, "Electronic wave functions in semiconductor clusters: Experiment and theory," *J. Phys. Chem*, vol. 90, pp. 2555–2560, 1986. (see p. 4)

[35] C. B. Murray, D. J. Noms, and M. G. Bawendi', "Synthesis and Characterization of Nearly Monodisperse CdE (E = S, Se, Te) Semiconductor Nanocrystallites," *J. Am. Chem. Soc*, vol. 115, pp. 8706–8715, 1993. (see pp. 5 and 23)

[36] J. Butkus, P. Vashishtha, K. Chen, J. K. Gallaher, S. K. Prasad, D. Z. Metin, G. Laufersky, N. Gaston, J. E. Halpert, and J. M. Hodgkiss, "The Evolution of Quantum Confinement in $CsPbBr_3$ Perovskite Nanocrystals," *Chemistry of Materials*, vol. 29, pp. 3644–3652, 4 2017. (see p. 5)

[37] J. Maes, L. Balcaen, E. Drijvers, Q. Zhao, J. D. Roo, A. Vantomme, F. Vanhaecke, P. Geiregat, and Z. Hens, "Light Absorption Coefficient of $CsPbBr_3$ Perovskite Nanocrystals," *Journal of Physical Chemistry Letters*, vol. 9, pp. 3093–3097, 6 2018. (see p. 5)

[38] Q. A. Akkerman, D. Meggiolaro, Z. Dang, F. D. Angelis, and L. Manna, "Fluorescent Alloy $CsPb_xMn_{1-x}I_3$ Perovskite Nanocrystals with High Structural and Optical Stability," *ACS Energy Letters*, vol. 2, pp. 2183–2186, 9 2017. (see p. 5)

[39] R. X. Yang and L. Z. Tan, "Understanding size dependence of phase stability and band gap in $CsPbI_3$ perovskite nanocrystals," *Journal of Chemical Physics*, vol. 152, 1 2020. (see p. 5)

[40] S. Paul and A. Samanta, "Phase-Stable and Highly Luminescent $CsPbI_3$ Perovskite Nanocrystals with Suppressed Photoluminescence Blinking," *Journal of Physical Chemistry Letters*, vol. 13, pp. 5742–5750, 6 2022. (see p. 5)

[41] A. Swarnkar, A. R. Marshall, E. M. Sanehira, B. D. Chernomordik, D. T. Moore, J. A. Christians, J. M. L. T. Chakrabarti, and joseph M. Luther, "Quantum dot–induced phase stabilization of a $CsPbI_3$ perovskite for high-efficiency photovoltaics," *Science*, vol. 354, pp. 92–96, 2016. (see pp. 5, 25, and 26)

[42] S. Sun, D. Yuan, Y. Xu, A. Wang, and Z. Deng, "Ligand-Mediated Synthesis of Shape-Controlled Cesium Lead Halide Perovskite Nanocrystals via Reprecipitation Process at Room Temperature," *ACS Nano*, vol. 10, pp. 3648–3657, 2016. (see pp. 5 and 25)

[43] A. Swarnkar, R. Chulliyil, V. K. Ravi, M. Irfanullah, A. Chowdhury, and A. Nag, "Colloidal $CsPbBr_3$ Perovskite Nanocrystals: Luminescence beyond Traditional Quantum Dots," *Angewandte Chemie*, vol. 127, pp. 15644–15648, 12 2015. (see p. 5)

[44] F. D. Stasio, S. Christodoulou, N. Huo, and G. Konstantatos, "Near-Unity Photoluminescence Quantum Yield in $CsPbBr_3$ Nanocrystal Solid-State Films via Postsynthesis Treatment with Lead Bromide," *Chemistry of Materials*, vol. 29, pp. 7663–7667, 2017. (see pp. 5 and 24)

[45] H. Shankar, W. W. Yu, Y. Kang, and P. Kar, "Significant boost of the stability and PLQY of $CsPbBr_3$ NCs by Cu-BTC MOF," *Scientific Reports*, vol. 12, pp. 1–9, 2022. (see p. 5)

[46] K. Wu, G. Liang, Q. Shang, Y. Ren, D. Kong, and T. Lian, "Ultrafast interfacial electron and hole transfer from $CsPbBr_3$ perovskite quantum dots," *Journal of the American Chemical Society*, vol. 137, pp. 12792–12795, 10 2015. (see p. 5)

[47] X. Ling, J. Yuan, X. Zhang, Y. Qian, S. M. Zakeeruddin, B. W. Larson, Q. Zhao, J. Shi, J. Yang, K. Ji, Y. Zhang, Y. Wang, C. Zhang, S. Duhm, J. M. Luther, M. Grätzel, and W. Ma, "Guanidinium-Assisted Surface Matrix Engineering for Highly Efficient Perovskite Quantum Dot Photovoltaics," *Advanced Materials*, vol. 32, 7 2020. (see p. 5)

[48] E. M. Sanehira, A. R. Marshall, J. A. Christians, S. P. Harvey, P. N. Ciesielski, L. M. Wheeler, P. Schulz, L. Y. Lin, M. C. Beard, and J. M. Luther, "Enhanced mobility $CsPbI_3$ quantum dot arrays for record-efficiency, high-voltage photovoltaic cells," *Science Advances*, vol. 3, pp. 1–8, 2017. (see pp. 5 and 26)

[49] J. Yuan, X. Ling, D. Yang, F. Li, S. Zhou, J. Shi, Y. Qian, J. Hu, Y. Sun, Y. Yang, X. Gao, S. Duhm, Q. Zhang, and W. Ma, "Band-Aligned Polymeric Hole Transport Materials for Extremely Low Energy Loss -$CsPbI_3$ Perovskite Nanocrystal Solar Cells," *Joule*, vol. 2, pp. 2450–2463, 11 2018. (see pp. 5 and 26)

[50] X. Ling, S. Zhou, J. Yuan, J. Shi, Y. Qian, B. W. Larson, Q. Zhao, C. Qin, F. Li, G. Shi, C. Stewart, J. Hu, X. Zhang, J. M. Luther, S. Duhm, and W. Ma, "14.1% $CsPbI_3$ Perovskite Quantum Dot Solar Cells via Cesium Cation Passivation," *Advanced Energy Materials*, vol. 9, 7 2019. (see pp. 5 and 26)

[51] F. Li, S. Zhou, J. Yuan, C. Qin, Y. Yang, J. Shi, X. Ling, Y. Li, and W. Ma, "Perovskite Quantum Dot Solar Cells with 15.6% Efficiency and Improved Stability Enabled by an α-$CsPbI_3$/$FAPbI_3$ Bilayer Structure," *ACS Energy Letters*, vol. 4, pp. 2571–2578, 11 2019. (see pp. 5 and 26)

[52] M. Hao, Y. Bai, S. Zeiske, L. Ren, J. Liu, Y. Yuan, N. Zarrabi, N. Cheng, M. Ghasemi, P. Chen, M. Lyu, D. He, J. H. Yun, Y. Du, Y. Wang, S. Ding, A. Armin, P. Meredith, G. Liu, H. M. Cheng, and L. Wang, "Ligand-assisted cation-exchange engineering for high-efficiency colloidal $Cs_{1-x}FA_xPbI_3$ quantum dot solar cells with reduced phase segregation," *Nature Energy*, vol. 5, pp. 79–88, 1 2020. (see p. 5)

[53] E. Parliament and C. of the European Union (2011), "Directive 2011/65/EU of the European Parliament and of the Council of 8 June 2011 on the restriction of the use of certain hazardous substances in electrical and electronic equipment.," *Official Journal of the European Union*, vol. 174, pp. 88–110, 2011. (see p. 6)

[54] E. P. Agency, "Hazardous Waste Management System; Identification and Listing of Hazardous Waste; Toxicity Characteristic Revisions," *Federal Register*, vol. 55, pp. 26986–26998, 1990. (see p. 6)

[55] G. Flora, D. Gupta, and A. Tiwari, "Toxicity of lead: A review with recent updates," *Interdisciplinary Toxicology*, vol. 5, pp. 47–58, 2012. (see p. 6)

[56] W. Ke and M. G. Kanatzidis, "Prospects for low-toxicity lead-free perovskite solar cells," *Nature Communications*, vol. 10, pp. 1–4, 2019. (see pp. 6 and 7)

[57] A. Babayigit, D. D. Thanh, A. Ethirajan, J. Manca, M. Muller, H. G. Boyen, and B. Conings, "Assessing the toxicity of Pb-and Sn-based perovskite solar cells in model organism Danio rerio," *Scientific Reports*, vol. 6, pp. 1–11, 2016. (see pp. 6 and 7)

[58] A. Abate, "Perovskite Solar Cells Go Lead Free," *Joule*, vol. 1, pp. 659–664, 12 2017. (see pp. 6, 8, and 49)

[59] N. Moody, S. Sesena, D. W. deQuilettes, B. D. Dow, R. Swartwout, J. T. Buchman, A. Johnson, U. Eze, R. Brenes, M. Johnston, C. L. Haynes, V. Bulovic, and M. G. Bawendi, "Assessing the Regulatory Requirements of Lead-Based Perovskite Photovoltaics," *Joule*, vol. 4, pp. 967–974, 5 2020. (see p. 6)

[60] A. Babayigit, A. Ethirajan, M. Muller, and B. Conings, "Toxicity of organometal halide perovskite solar cells," *Nature Materials*, vol. 15, pp. 247–251, 2 2016. (see p. 6)

[61] R. Y. Kim, J. K. Yoon, T. S. Kim, J. E. Yang, G. Owens, and K. R. Kim, "Bioavailability of heavy metals in soils: definitions and practical implementation—a critical review," *Environmental Geochemistry and Health*, vol. 37, pp. 1041–1061, 12 2015. (see p. 6)

[62] G. Schileo and G. Grancini, "Lead or no lead? Availability, toxicity, sustainability and environmental impact of lead-free perovskite solar cells," *Journal of Materials Chemistry C*, vol. 9, pp. 67–76, 1 2021. (see p. 6)

[63] J. Li, H.-L. Cao, W.-B. Jiao, Q. Wang, M. Wei, I. Cantone, J. Lü, and A. Abate, "Biological impact of lead from halide perovskites reveals the risk of introducing a safe threshold," *Nature Communications*, vol. 11, p. 310, 2020. (see p. 7)

[64] L. Serrano-Lujan, N. Espinosa, T. T. Larsen-Olsen, J. Abad, A. Urbina, and F. C. Krebs, "Tin- and lead-based perovskite solar cells under scrutiny: An environmental perspective," *Advanced Energy Materials*, vol. 5, pp. 1–5, 2015. (see p. 7)

[65] X. Jiang, H. Li, Q. Zhou, Q. Wei, M. Wei, L. Jiang, Z. Wang, Z. Peng, F. Wang, Z. Zang, K. Xu, Y. Hou, S. Teale, W. Zhou, R. Si, X. Gao, E. H. Sargent, and Z. Ning, "One-Step Synthesis of $SnI_2 \cdot (DMSO)_x$Adducts for High-Performance Tin Perovskite Solar Cells," *Journal of the American Chemical Society*, vol. 143, pp. 10970–10976, 7 2021. (see p. 7)

[66] F. Giustino and H. J. Snaith, "Toward Lead-Free Perovskite Solar Cells," *ACS Energy Letters*, vol. 1, pp. 1233–1240, 2016. (see p. 7)

[67] M. R. Filip and F. Giustino, "Computational Screening of Homovalent Lead Substitution in Organic-Inorganic Halide Perovskites," *Journal of Physical Chemistry C*, vol. 120, pp. 166–173, 2016. (see p. 7)

[68] S. E. Creutz, E. N. Crites, M. C. D. Siena, and D. R. Gamelin, "Colloidal Nanocrystals of Lead-Free Double-Perovskite (Elpasolite) Semiconductors: Synthesis and Anion Exchange to Access New Materials," *Nano Letters*, vol. 18, pp. 1118–1123, 2018. (see pp. 7 and 25)

[69] M. Pantaler, K. T. Cho, V. I. Queloz, I. G. Benito, C. Fettkenhauer, I. Anusca, M. K. Nazeeruddin, D. C. Lupascu, and G. Grancini, "Hysteresis-Free Lead-Free Double-Perovskite Solar Cells by Interface Engineering," *ACS Energy Letters*, vol. 3, pp. 1781–1786, 2018. (see p. 7)

[70] J. Kangsabanik, V. Sugathan, A. Yadav, A. Yella, and A. Alam, "Double perovskites overtaking the single perovskites: A set of new solar harvesting materials with much higher stability and efficiency," *Physical Review Materials*, vol. 2, pp. 1–12, 2018. (see p. 7)

[71] J. Li, J. Duan, X. Yang, Y. Duan, P. Yang, and Q. Tang, "Review on recent progress of lead-free halide perovskites in optoelectronic applications," *Nano Energy*, vol. 80, 2 2021. (see p. 7)

[72] X. G. Zhao, J. H. Yang, Y. Fu, D. Yang, Q. Xu, L. Yu, S. H. Wei, and L. Zhang, "Design of Lead-Free Inorganic Halide Perovskites for Solar Cells via Cation-Transmutation," *Journal of the American Chemical Society*, vol. 139, pp. 2630–2638, 2017. (see pp. 8 and 13)

[73] Z. Xiao, K. Z. Du, W. Meng, J. Wang, D. B. Mitzi, and Y. Yan, "Intrinsic Instability of $Cs_2In(I)M(III)X_6$ (M = Bi, Sb; X = Halogen) Double Perovskites: A Combined Density Functional Theory and Experimental Study," *Journal of the American Chemical Society*, vol. 139, pp. 6054–6057, 2017. (see p. 8)

[74] B. Li, X. Wu, S. Zhang, Z. Li, D. Gao, X. Chen, S. Xiao, C. C. Chueh, A. K. Jen, and Z. Zhu, "Efficient and stable $Cs_2AgBiBr_6$ double perovskite solar cells through in-situ surface modulation," *Chemical Engineering Journal*, vol. 446, 10 2022. (see p. 8)

[75] Z. Zhang, Q. Sun, Y. Lu, F. Lu, X. Mu, S.-H. Wei, and M. Sui, "Hydrogenated $Cs_2AgBiBr_6$ for significantly improved efficiency of lead-free inorganic double perovskite solar cell," *Nature Communications*, vol. 13, pp. 1–12, 2022. (see p. 8)

[76] F. Bai, Y. Hu, Y. Hu, T. Qiu, X. Miao, and S. Zhang, "Lead-free, air-stable ultrathin $Cs_3Bi_2I_9$ perovskite nanosheets for solar cells," *Solar Energy Materials and Solar Cells*, vol. 184, pp. 15–21, 9 2018. (see p. 8)

[77] S. M. Jain, D. Phuyal, M. L. Davies, M. Li, B. Philippe, C. D. Castro, Z. Qiu, J. Kim, T. Watson, W. C. Tsoi, O. Karis, H. Rensmo, G. Boschloo, T. Edvinsson, and J. R. Durrant, "An effective approach of vapour assisted morphological tailoring for reducing metal defect sites in lead-free, $(CH_3NH_3)_3Bi_2I_9$ bismuth-based perovskite solar cells for improved performance and long-term stability," *Nano Energy*, vol. 49, pp. 614–624, 7 2018. (see p. 8)

[78] W. Hu, X. He, Z. Fang, W. Lian, Y. Shang, X. Li, W. Zhou, M. Zhang, T. Chen, Y. Lu, L. Zhang, L. Ding, and S. Yang, "Bulk heterojunction gifts bismuth-based lead-free perovskite solar cells with record efficiency," *Nano Energy*, vol. 68, 2 2020. (see p. 8)

[79] R. Nie, A. Mehta, B. W. Park, H. W. Kwon, J. Im, and S. I. Seok, "Mixed Sulfur and Iodide-Based Lead-Free Perovskite Solar Cells," *Journal of the American Chemical Society*, vol. 140, pp. 872–875, 1 2018. (see p. 8)

[80] S. A. Adonin, L. A. Frolova, M. N. Sokolov, G. V. Shilov, D. V. Korchagin, V. P. Fedin, S. M. Aldoshin, K. J. Stevenson, and P. A. Troshin, "Antimony (V) Complex Halides: Lead-Free Perovskite-Like Materials for Hybrid Solar Cells," *Advanced Energy Materials*, vol. 8, 2 2018. (see p. 8)

[81] M. Chen, M. G. Ju, A. D. Carl, Y. Zong, R. L. Grimm, J. Gu, X. C. Zeng, Y. Zhou, and N. P. Padture, "Cesium Titanium(IV) Bromide Thin Films Based Stable Lead-free Perovskite Solar Cells," *Joule*, vol. 2, pp. 558–570, 2018. (see pp. 8, 19, 31, 35, 44, and 71)

[82] A. Singh, K. M. Boopathi, A. Mohapatra, Y. F. Chen, G. Li, and C. W. Chu, "Photovoltaic Performance of Vapor-Assisted Solution-Processed Layer Polymorph of $Cs_3Sb_2I_9$," *ACS Applied Materials and Interfaces*, vol. 10, pp. 2566–2573, 1 2018. (see p. 8)

[83] X. Qiu, B. Cao, S. Yuan, X. Chen, Z. Qiu, Y. Jiang, Q. Ye, H. Wang, H. Zeng, J. Liu, and M. G. Kanatzidis, "From unstable $CsSnI_3$ to air-stable Cs_2SnI_6: A lead-free perovskite solar cell light absorber with bandgap of 1.48 eV and high absorption coefficient," *Solar Energy Materials and Solar Cells*, vol. 159, pp. 227–234, 1 2017. (see pp. 8 and 49)

[84] H. Gordon, "Rare Earth Elements-Critical Resources for High Technology," *US Department of the Interior, US Geological Survey*, vol. 87, 2002. (see p. 9)

[85] J. W. Morgan and E. Anders, "Chemical composition of Earth, Venus, and Mercury," *Proceedings of the National Academy of Sciences*, vol. 77, pp. 6973–6977, 1980. (see p. 8)

[86] P. Nuss and M. J. Eckelman, "Life Cycle Assessment of Metals: A Scientific Synthesis," *PLOS ONE*, vol. 9, pp. 1–12, 2014. (see p. 8)

[87] K. P. Ong, T. W. Goh, Q. Xu, and A. Huan, "Structural Evolution in Methylammonium Lead Iodide $CH_3NH_3PbI_3$," *Journal of Physical Chemistry A*, vol. 119, pp. 11033–11038, 10 2015. (see p. 12)

[88] C. Li, K. C. K. Soh, and P. Wu, "Formability of ABO_3 perovskites," *Journal of Alloys and Compounds*, vol. 372, pp. 40–48, 6 2004. (see p. 12)

[89] W. Travis, E. N. Glover, H. Bronstein, D. O. Scanlon, and R. G. Palgrave, "On the application of the tolerance factor to inorganic and hybrid halide perovskites: A revised system," *Chemical Science*, vol. 7, pp. 4548–4556, 2016. (see p. 12)

[90] A. Amat, E. Mosconi, E. Ronca, C. Quarti, P. Umari, M. K. Nazeeruddin, M. Grätzel, and F. D. Angelis, "Cation-induced band-gap tuning in organohalide perovskites: Interplay of spin-orbit coupling and octahedra tilting," *Nano Letters*, vol. 14, pp. 3608–3616, 6 2014. (see p. 12)

[91] C. Li, X. Lu, W. Ding, L. Feng, Y. Gao, and Z. Guo, "Formability of ABX_3 (X = F, Cl, Br, I) halide perovskites," *Acta Crystallographica Section B: Structural Science*, vol. 64, pp. 702–707, 2008. (see p. 13)

[92] S. Vasala and M. Karppinen, "A_2BBO_6 perovskites: A review," *Progress in Solid State Chemistry*, vol. 43, pp. 1–36, 2015. (see p. 13)

[93] A. H. Slavney, T. Hu, A. M. Lindenberg, and H. I. Karunadasa, "A Bismuth-Halide Double Perovskite with Long Carrier Recombination Lifetime for Photovoltaic Applications," *Journal of the American Chemical Society*, vol. 138, pp. 2138–2141, 2016. (see p. 13)

[94] E. T. McClure, M. R. Ball, W. Windl, and P. M. Woodward, "Cs_2AgBiX_6 (X = Br, Cl): New Visible Light Absorbing, Lead-Free Halide Perovskite Semiconductors," *Chemistry of Materials*, vol. 28, pp. 1348–1354, 2016. (see p. 13)

[95] M. R. Filip, S. Hillman, A. A. Haghighirad, H. J. Snaith, and F. Giustino, "Band Gaps of the Lead-Free Halide Double Perovskites $Cs_2BiAgCl_6$ and $Cs_2BiAgBr_6$ from Theory and Experiment," *Journal of Physical Chemistry Letters*, vol. 7, pp. 2579–2585, 2016. (see p. 13)

[96] M. Roy, S. Ghorui, Bhawna, J. Kangsabanik, R. Yadav, A. Alam, and M. Aslam, "Enhanced Visible Light Absorption in Layered $Cs_3Bi_2Br_9$ Halide Perovskites: Heterovalent Pb^{+2} Substitution-Induced Defect Band Formation," *Journal of Physical Chemistry C*, vol. 124, pp. 19484–19491, 9 2020. (see p. 13)

[97] C. J. Krajewska, S. R. Kavanagh, L. Zhang, D. J. Kubicki, K. Dey, K. Gałkowski, C. P. Grey, S. D. Stranks, A. Walsh, D. O. Scanlon, and R. G. Palgrave, "Enhanced visible light absorption in layered $Cs_3Bi_2Br_9$ through mixed-valence Sn(II)/Sn(IV) doping," *Chemical Science*, vol. 12, pp. 14686–14699, 11 2021. (see p. 13)

[98] Y. Peng, F. Li, Y. Wang, Y. Li, R. L. Hoye, L. Feng, K. Xia, and V. Pecunia, "Enhanced photoconversion efficiency in cesium-antimony-halide perovskite derivatives by tuning crystallographic dimensionality," *Applied Materials Today*, vol. 19, 6 2020. (see p. 13)

[99] B. Lee, C. C. Stoumpos, N. Zhou, F. Hao, C. Malliakas, C. Y. Yeh, T. J. Marks, M. G. Kanatzidis, and R. P. Chang, "Air-stable molecular semiconducting iodosalts for solar cell applications: $Cs_2 2SnI_6$ as a hole conductor," *Journal of the American Chemical Society*, vol. 136, pp. 15379–15385, 10 2014. (see pp. 13, 19, and 49)

[100] A. E. Maughan, A. M. Ganose, D. O. Scanlon, and J. R. Neilson, "Perspectives and Design Principles of Vacancy-Ordered Double Perovskite Halide Semiconductors," *Chemistry of Materials*, vol. 31, pp. 1184–1195, 2 2019. (see p. 13)

[101] B. Saparov, J. P. Sun, W. Meng, Z. Xiao, H. S. Duan, O. Gunawan, D. Shin, I. G. Hill, Y. Yan, and D. B. Mitzi, "Thin-Film Deposition and Characterization of a Sn-Deficient Perovskite Derivative $Cs_2 2SnI_6$," *Chemistry of Materials*, vol. 28, pp. 2315–2322, 2016. (see pp. 13, 31, and 49)

[102] N. Sakai, A. A. Haghighirad, M. R. Filip, P. K. Nayak, S. Nayak, A. Ramadan, Z. Wang, F. Giustino, and H. J. Snaith, "Solution-Processed Cesium Hexabromopalladate(IV), Cs_2PdBr_6, for Optoelectronic Applications," *Journal of the American Chemical Society*, vol. 139, pp. 6030–6033, 2017. (see pp. 13 and 31)

[103] I. Vázquez-Fernández, S. Mariotti, O. S. Hutter, M. Birkett, T. D. Veal, T. D. Hobson, L. J. Phillips, L. Danos, P. K. Nayak, H. J. Snaith, W. Xie, M. P. Sherburne, M. Asta, and K. Durose, "Vacancy-Ordered Double Perovskite Cs_2TeI_6 Thin Films for Optoelectronics," *Chemistry of Materials*, vol. 32, pp. 6676–6684, 2020. (see pp. 13 and 31)

[104] S. M. Liga and G. Konstantatos, "Colloidal synthesis of lead-free $Cs_2TiBr_{6-x}I_x$ perovskite nanocrystals," *Journal of Materials Chemistry C*, vol. 9, pp. 11098–11103, 9 2021. (see pp. 13, 14, and 19)

[105] W. Zhu, G. Xin, Y. Wang, X. Min, T. Yao, W. Xu, M. Fang, S. Shi, J. Shi, and J. Lian, "Tunable optical properties and stability of lead free all inorganic perovskites ($Cs_3SnI_xCl_{6-x}$)," *Journal of Materials Chemistry A*, vol. 6, pp. 2577–2584, 2018. (see pp. 14, 19, 27, 28, and 49)

[106] M. M. Karim, A. M. Ganose, L. Pieters, W. W. W. Leung, J. Wade, L. Zhang, D. O. Scanlon, and R. G. Palgrave, "Anion Distribution, Structural Distortion, and Symmetry-Driven Optical Band Gap Bowing in Mixed Halide Cs_2SnX_6 Vacancy Ordered Double Perovskites," *Chemistry of Materials*, vol. 31, pp. 9430–9444, 11 2019. (see pp. 14, 19, 27, 28, 49, and 72)

[107] C. C. Stoumpos, C. D. Malliakas, and M. G. Kanatzidis, "Semiconducting tin and lead iodide perovskites with organic cations: Phase transitions, high mobilities, and near-infrared photoluminescent properties," *Inorganic Chemistry*, vol. 52, pp. 9019–9038, 8 2013. (see pp. 14 and 15)

[108] B. Lee, A. Krenselewski, S. I. Baik, D. N. Seidman, and R. P. Chang, "Solution processing of air-stable molecular semiconducting iodosalts, $Cs_2SnI_{6-x}Br_x$, for potential solar cell applications," *Sustainable Energy and Fuels*, vol. 1, pp. 710–724, 2017. (see pp. 14, 19, 49, and 72)

[109] A. E. Maughan, A. M. Ganose, A. M. Candia, J. T. Granger, D. O. Scanlon, and J. R. Neilson, "Anharmonicity and Octahedral Tilting in Hybrid Vacancy-Ordered Double Perovskites," *Chemistry of Materials*, vol. 30, pp. 472–483, 1 2018. (see p. 14)

[110] A. Kaltzoglou, M. Antoniadou, A. G. Kontos, C. C. Stoumpos, D. Perganti, E. Siranidi, V. Raptis, K. Trohidou, V. Psycharis, M. G. Kanatzidis, and P. Falaras, "Optical-Vibrational Properties of the Cs_2SnX_6 (X = Cl, Br, I) Defect Perovskites and Hole-Transport Efficiency in Dye-Sensitized Solar Cells," *Journal of Physical Chemistry C*, vol. 120, pp. 11777–11785, 6 2016. (see p. 14)

[111] D. Kong, D. Cheng, X. Wang, K. Zhang, H. Wang, K. Liu, H. Li, X. Sheng, and L. Yin, "Solution processed lead-free cesium titanium halide perovskites and their structural, thermal and optical characteristics," *Journal of Materials Chemistry C*, vol. 8, 2020. (see pp. 14, 19, 28, 31, 32, 44, and 112)

[112] G. K. Grandhi, A. Matuhina, M. Liu, S. Annurakshita, H. Ali-Löytty, G. Bautista, and P. Vivo, "Lead-free cesium titanium bromide double perovskite nanocrystals," *Nanomaterials*, vol. 11, 6 2021. (see pp. 14, 19, 28, 45, and 71)

[113] J. Euvrard, X. Wang, T. Li, Y. Yan, and D. B. Mitzi, "Is Cs_2TiBr_6 a promising Pb-free perovskite for solar energy applications? ," *Journal of Materials Chemistry A*, 2020. (see pp. 14, 19, 32, 35, 45, and 71)

[114] W. Meng, X. Wang, Z. Xiao, J. Wang, D. B. Mitzi, and Y. Yan, "Parity-Forbidden Transitions and Their Impact on the Optical Absorption Properties of Lead-Free Metal Halide Perovskites and Double Perovskites," *Journal of Physical Chemistry Letters*, vol. 8, pp. 2999–3007, 2017. (see p. 15)

[115] C. Wehrenfennig, M. Liu, H. J. Snaith, M. B. Johnston, and L. M. Herz, "Charge-carrier dynamics in vapour-deposited films of the organolead halide perovskite $CH_3NH_3PbI_{3-x}Cl_x$," *Energy and Environmental Science*, vol. 7, pp. 2269–2275, 2014. (see p. 15)

[116] G. Xing, N. Mathews, S. Sun, S. S. Lim, Y. M. Lam, M. Grätzel, S. Mhaisalkar, and T. C. Sum, "Long-Range Balanced Electron-and Hole-Transport Lengths inOrganic-Inorganic $CH_3NH_3PbI_3$," *Science*, vol. 342, pp. 344–348, 11 2013. (see p. 15)

[117] M. R. Filip, G. E. Eperon, H. J. Snaith, and F. Giustino, "Steric engineering of metal-halide perovskites with tunable optical band gaps," *Nature Communications*, vol. 5, 2014. (see p. 15)

[118] I. Borriello, G. Cantele, and D. Ninno, "Ab initio investigation of hybrid organic-inorganic perovskites based on tin halides," *Physical Review B - Condensed Matter and Materials Physics*, vol. 77, 6 2008. (see p. 15)

[119] G. E. Eperon, S. D. Stranks, C. Menelaou, M. B. Johnston, L. M. Herz, and H. J. Snaith, "Formamidinium lead trihalide: A broadly tunable perovskite for efficient planar heterojunction solar cells," *Energy and Environmental Science*, vol. 7, pp. 982–988, 3 2014. (see p. 15)

[120] L. Y. Huang and W. R. Lambrecht, "Electronic band structure, phonons, and exciton binding energies of halide perovskites $CsSnCl_3$, $CsSnBr_3$, and $CsSnI_3$," *Physical Review B - Condensed Matter and Materials Physics*, vol. 88, 10 2013. (see p. 15)

[121] F. Brivio, A. B. Walker, and A. Walsh, "Structural and electronic properties of hybrid perovskites for high-efficiency thin-film photovoltaics from first-principles," *APL Materials*, vol. 1, p. 042111, 2013. (see p. 15)

[122] N. Kitazawa, Y. Watanabe, and Y. Nakamura, "Optical properties of $CH_3NH_3PbX_3$ (X = halogen) and their mixed-halide crystals," *Journal of materials science*, vol. 37, pp. 3585–3587, 2002. (see p. 15)

[123] E. Mosconi, P. Umari, and F. D. Angelis, "Electronic and optical properties of $MAPbX_3$ perovskites (X = I, Br, Cl): A unified DFT and GW theoretical analysis," *Physical Chemistry Chemical Physics*, vol. 18, pp. 27158–27164, 2016. (see p. 15)

[124] S. Adjokatse, H. H. Fang, and M. A. Loi, "Broadly tunable metal halide perovskites for solid-state light-emission applications," *Materials Today*, vol. 20, pp. 413–424, 10 2017. (see p. 15)

[125] V. D'Innocenzo, G. Grancini, M. J. Alcocer, A. R. S. Kandada, S. D. Stranks, M. M. Lee, G. Lanzani, H. J. Snaith, and A. Petrozza, "Excitons versus free charges in organo-lead tri-halide perovskites," *Nature Communications*, vol. 5, 4 2014. (see p. 16)

[126] M. Saba, M. Cadelano, D. Marongiu, F. Chen, V. Sarritzu, N. Sestu, C. Figus, M. Aresti, R. Piras, A. G. Lehmann, C. Cannas, A. Musinu, F. Quochi, A. Mura, and G. Bongiovanni, "Correlated electron-hole plasma in organometal perovskites," *Nature Communications*, vol. 5, 2014. (see p. 16)

[127] G. M. Dalpian, Q. Liu, C. C. Stoumpos, A. P. Douvalis, M. Balasubramanian, M. G. Kanatzidis, and A. Zunger, "Changes in charge density vs changes in formal oxidation states: The case of Sn halide perovskites and their ordered vacancy analogues," *Physical Review Materials*, vol. 1, 7 2017. (see pp. 19, 49, 51, and 72)

[128] J. Zhou, J. Luo, X. Rong, P. Wei, M. S. Molokeev, Y. Huang, J. Zhao, Q. Liu, X. Zhang, J. Tang, and Z. Xia, "Lead-Free Perovskite Derivative $Cs_2SnCl_{6-x}Br_x$Single Crystals for Narrowband Photodetectors," *Advanced Optical Materials*, vol. 7, 5 2019. (see pp. 19 and 72)

[129] S. Bonomi, M. Patrini, G. Bongiovanni, and L. Malavasi, "Versatile vapor phase deposition approach to cesium tin bromide materials $CsSnBr_3$, $CsSn_2Br_5$ and Cs_2SnBr_6," *RSC Advances*, vol. 10, pp. 28478–28482, 8 2020. (see pp. 19 and 72)

[130] A. E. Maughan, A. M. Ganose, M. M. Bordelon, E. M. Miller, D. O. Scanlon, and J. R. Neilson, "Defect Tolerance to Intolerance in the Vacancy-Ordered Double Perovskite Semiconductors Cs_2SnI_6 and Cs_2TeI_6," *Journal of the American Chemical Society*, vol. 138, pp. 8453–8464, 2016. (see pp. 19 and 49)

[131] J. Zhang, C. Yu, L. Wang, Y. Li, Y. Ren, and K. Shum, "Energy barrier at the N719-dye/$CsSnI_3$ interface for photogenerated holes in dye-sensitized solar cells," *Scientific Reports*, vol. 4, 2014. (see pp. 19 and 49)

[132] M. G. Ju, M. Chen, Y. Zhou, H. F. Garces, J. Dai, L. Ma, N. P. Padture, and X. C. Zeng, "Earth-Abundant Nontoxic Titanium(IV)-based Vacancy-Ordered Double Perovskite Halides with Tunable 1.0 to 1.8 eV Bandgaps for Photovoltaic Applications," *ACS Energy Letters*, vol. 3, pp. 297–304, 2018. (see pp. 19, 31, 32, 35, 44, and 45)

[133] J. L. Mendes, W. Gao, J. L. Martin, A. D. Carl, N. A. Deskins, S. Granados-Focil, and R. L. Grimm, "Interfacial States, Energetics, and Atmospheric Stability of Large-Grain Antifluorite Cs_2TiBr_6," *The Journal of Physical Chemistry C*, vol. 124, pp. 24289–24297, 2020. (see pp. 19, 45, and 71)

[134] Y. He, X. Guo, H. Zheng, L. Xv, and S. Li, "Stability investigation of the titanium-based eco-friendly perovskite-like antifluorite Cs_2TiBr_6," *Journal of Materials Chemistry C*, vol. 10, pp. 9301–9309, 5 2022. (see pp. 19, 45, and 71)

[135] B. J. Brisdon, T. E. L. Ster, and R. A. W. lton, "Complex halides of transition metals III* Electronic absorption spectra of hexahalotitanates(IV), vanadates (IV), and zirconates(IV)," *Spectrochimica Acta*, vol. 23, 1967. (see p. 21)

[136] A. Abfalterer, J. Shamsi, D. J. Kubicki, C. N. Savory, J. Xiao, G. Divitini, W. Li, S. Macpherson, K. Gałkowski, J. L. Macmanus-Driscoll, D. O. Scanlon, and S. D. Stranks, "Colloidal Synthesis and Optical Properties of Perovskite-Inspired Cesium Zirconium Halide Nanocrystals," *ACS Materials Letters*, vol. 2, pp. 1644–1652, 12 2020. (see pp. 21 and 31)

[137] M. Buryi, V. Babin, R. A. Ligthart, S. S. Nagorny, V. B. Mikhailik, V. Vaněček, L. P. Prochazková, R. Kandel, V. V. Nahorna, and P. Wang, "Correlation of emission, scintillation and charge trapping properties in Cs_2HfCl_6 and Cs_2ZrCl_6 single crystals," *Journal of Materials Chemistry C*, vol. 9, pp. 2955–2968, 2 2021. (see p. 21)

[138] S. Liu, B. Yang, J. Chen, D. Zheng, Z. Tang, W. Deng, and K. Han, "Colloidal Synthesis and Tunable Multicolor Emission of Vacancy-Ordered Cs_2HfCl_6 Per-

ovskite Nanocrystals," *Laser and Photonics Reviews*, vol. 16, 2 2022. (see p. 21)

[139] R. I. Biega, M. R. Filip, L. Leppert, and J. B. Neaton, "Chemically Localized Resonant Excitons in Silver-Pnictogen Halide Double Perovskites," *Journal of Physical Chemistry Letters*, vol. 12, pp. 2057–2063, 3 2021. (see p. 21)

[140] A. D. Wright, L. R. Buizza, K. J. Savill, G. Longo, H. J. Snaith, M. B. Johnston, and L. M. Herz, "Ultrafast Excited-State Localization in $Cs_2AgBiBr_6$ Double Perovskite," *Journal of Physical Chemistry Letters*, vol. 12, pp. 3352–3360, 4 2021. (see p. 21)

[141] M. Palummo, E. Berrios, D. Varsano, and G. Giorgi, "Optical Properties of Lead-Free Double Perovskites by Ab Initio Excited-State Methods," *ACS Energy Letters*, pp. 457–463, 2020. (see p. 21)

[142] C. N. Savory, A. Walsh, and D. O. Scanlon, "Can Pb-Free Halide Double Perovskites Support High-Efficiency Solar Cells?," *ACS Energy Letters*, vol. 1, pp. 949–955, 2016. (see p. 21)

[143] Z. Xiao, W. Meng, J. Wang, D. B. Mitzi, and Y. Yan, "Searching for promising new perovskite-based photovoltaic absorbers: The importance of electronic dimensionality," *Materials Horizons*, vol. 4, pp. 206–216, 3 2017. (see p. 21)

[144] Q. Zhao, A. Hazarika, X. Chen, S. P. Harvey, B. W. Larson, G. R. Teeter, J. Liu, T. Song, C. Xiao, L. Shaw, M. Zhang, G. Li, M. C. Beard, and J. M. Luther, "High efficiency perovskite quantum dot solar cells with charge separating heterostructure," *Nature Communications*, vol. 10, 2019. (see p. 22)

[145] A. Hazarika, Q. Zhao, E. A. Gaulding, J. A. Christians, B. Dou, A. R. Marshall, T. Moot, J. J. Berry, J. C. Johnson, and J. M. Luther, "Perovskite Quantum Dot Photovoltaic Materials beyond the Reach of Thin Films: Full-Range Tuning of A-Site Cation Composition," *ACS Nano*, 2018. (see p. 22)

[146] Q. A. Akkerman, M. Gandini, F. D. Stasio, P. Rastogi, F. Palazon, G. Bertoni, J. M. Ball, M. Prato, A. Petrozza, and L. Manna, "Strongly emissive perovskite nanocrystal inks for high-voltage solar cells," *Nature Energy*, vol. 2, 2017. (see p. 22)

[147] S. T. Ochsenbein, F. Krieg, Y. Shynkarenko, G. Rainò, and M. V. Kovalenko, "Engineering Color-Stable Blue Light-Emitting Diodes with Lead Halide Perovskite Nanocrystals," *ACS Applied Materials and Interfaces*, vol. 11, pp. 21655–21660, 2019. (see p. 22)

[148] J. Li, L. Xu, T. Wang, J. Song, J. Chen, J. Xue, Y. Dong, B. Cai, Q. Shan, B. Han, and H. Zeng, "50-Fold EQE Improvement up to 6.27% of Solution-Processed All-Inorganic Perovskite $CsPbBr_3$ QLEDs via Surface Ligand Density Control," *Advanced Materials*, vol. 29, 2017. (see p. 22)

[149] D. H. Kwak, D. H. Lim, H. S. Ra, P. Ramasamy, and J. S. Lee, "High performance hybrid graphene-$CsPbBr_{3-x}I_x$ perovskite nanocrystal photodetector," *RSC Advances*, vol. 6, pp. 65252–65256, 2016. (see p. 22)

[150] S. Yakunin, L. Protesescu, F. Krieg, M. I. Bodnarchuk, G. Nedelcu, M. Humer, G. D. Luca, M. Fiebig, W. Heiss, and M. V. Kovalenko, "Low-threshold amplified spontaneous emission and lasing from colloidal nanocrystals of caesium lead halide perovskites," *Nature Communications*, vol. 6, 2015. (see p. 22)

[151] C. B. Murray, C. R. Kagan, and M. G. Bawendi, "Synthesis and characterization of monodisperse nanocrystals and close-packed nanocrystal assemblies," *Annual review of materials Science*, vol. 30, pp. 545–610, 2000. (see p. 23)

[152] S. G. Kwon and T. Hyeon, "Formation mechanisms of uniform nanocrystals via hot-injection and heat-up methods," *Small*, vol. 7, pp. 2685–2702, 10 2011. (see p. 23)

[153] V. K. Lamer and R. H. Dinegar, "Theory, Production and Mechanism of Formation of Monodispersed Hydrosols," *Journal of the american chemical society*, vol. 72, pp. 4847–4854, 1950. (see p. 24)

[154] F. Krieg, P. C. Sercel, M. Burian, H. Andrusiv, M. I. Bodnarchuk, T. Stöferle, R. F. Mahrt, D. Naumenko, H. Amenitsch, G. Rainò, and M. V. Kovalenko, "Monodisperse Long-Chain Sulfobetaine-Capped $CsPbBr_3$ Nanocrystals and Their Superfluorescent Assemblies," *ACS Central Science*, vol. 7, pp. 135–144, 1 2021. (see p. 24)

[155] F. D. Stasio, I. Ramiro, Y. Bi, S. Christodoulou, A. Stavrinadis, and G. Konstantatos, "High-Efficiency Light-Emitting Diodes Based on Formamidinium Lead Bromide Nanocrystals and Solution Processed Transport Layers," *Chemistry of Materials*, vol. 30, pp. 6231–6235, 2018. (see p. 24)

[156] Z. Wu, S. Yang, and W. Wu, "Shape control of inorganic nanoparticles from solution," *Nanoscale*, vol. 8, pp. 1237–1259, 2016. (see p. 25)

[157] A. Wang, X. Yan, M. Zhang, S. Sun, M. Yang, W. Shen, X. Pan, P. Wang, and Z. Deng, "Controlled synthesis of lead-free and stable perovskite derivative

Cs_2SnI_6 nanocrystals via a facile hot-injection process," *Chemistry of Materials*, vol. 28, pp. 8132–8140, 2016. (see pp. 25, 31, and 50)

[158] T. C. Jellicoe, J. M. Richter, H. F. J. Glass, M. Tabachnyk, R. Brady, S. E. Dutton, A. Rao, R. H. Friend, D. Credgington, N. C. Greenham, and M. L. Bohm, "Synthesis and optical properties of lead-free cesium tin halide perovskite nanocrystals," *Journal of the American chemical society*, vol. 138, pp. 2941–2944, 2016. (see p. 25)

[159] M. Koolyk, D. Amgar, S. Aharon, and L. Etgar, "Kinetics of cesium lead halide perovskite nanoparticle growth; Focusing and de-focusing of size distribution," *Nanoscale*, vol. 8, pp. 6403–6409, 3 2016. (see p. 25)

[160] O. Vybornyi, S. Yakunin, and M. V. Kovalenko, "Polar-solvent-free colloidal synthesis of highly luminescent alkylammonium lead halide perovskite nanocrystals," *Nanoscale*, vol. 8, pp. 6278–6283, 2016. (see p. 25)

[161] J. Kang and L. W. Wang, "High Defect Tolerance in Lead Halide Perovskite $CsPbBr_3$," *Journal of Physical Chemistry Letters*, vol. 8, pp. 489–493, 1 2017. (see p. 25)

[162] X. Li, Y. Wu, S. Zhang, B. Cai, Y. Gu, J. Song, and H. Zeng, "$CsPbX_3$ Quantum Dots for Lighting and Displays: Roomerature Synthesis, Photoluminescence Superiorities, Underlying Origins and White Light-Emitting Diodes," *Advanced Functional Materials*, vol. 26, pp. 2435–2445, 4 2016. (see p. 25)

[163] J. Y. Woo, Y. Kim, J. Bae, T. G. Kim, J. W. Kim, D. C. Lee, and S. Jeong, "Highly Stable Cesium Lead Halide Perovskite Nanocrystals through in Situ Lead Halide Inorganic Passivation," *Chemistry of Materials*, vol. 29, pp. 7088–7092, 9 2017. (see p. 25)

[164] L. Protesescu, S. Yakunin, S. Kumar, J. Ba, F. Bertolotti, N. Masciocchi, A. Guagliardi, M. Grotevent, I. Shorubalko, M. I. Bodnarchuk, C.-J. Shih, and M. V. Kovalenko, "Dismantling the "Red Wall" of Colloidal Perovskites: Highly Luminescent Formamidinium and Formamidinium Cesium Lead Iodide Nanocrystals," *ACS Nano*, vol. 11, pp. 3119–3134, 2017. (see p. 25)

[165] Q. Li, H. Li, H. Shen, F. Wang, F. Zhao, F. Li, X. Zhang, D. Li, X. Jin, and W. Sun, "Solid Ligand-Assisted Storage of Air-Stable Formamidinium Lead Halide Quantum Dots via Restraining the Highly Dynamic Surface toward Brightly Luminescent Light-Emitting Diodes," *ACS Photonics*, vol. 4, pp. 2504–2512, 10 2017. (see p. 25)

[166] M. Imran, V. Caligiuri, M. Wang, L. Goldoni, M. Prato, R. Krahne, L. D. Trizio, and L. Manna, "Benzoyl Halides as Alternative Precursors for the Colloidal Synthesis of Lead-Based Halide Perovskite Nanocrystals," *Journal of the American Chemical Society*, vol. 140, pp. 2656–2664, 2 2018. (see p. 25)

[167] J. D. Roo, M. Ibáñez, P. Geiregat, G. Nedelcu, W. Walravens, J. Maes, J. C. Martins, I. V. Driessche, M. V. Kovalenko, and Z. Hens, "Highly Dynamic Ligand Binding and Light Absorption Coefficient of Cesium Lead Bromide Perovskite Nanocrystals," *ACS Nano*, vol. 10, pp. 2071–2081, 2016. (see p. 26)

[168] F. Krieg, S. T. Ochsenbein, S. Yakunin, S. T. Brinck, P. Aellen, A. Süess, B. Clerc, D. Guggisberg, O. Nazarenko, Y. Shynkarenko, S. Kumar, C. J. Shih, I. Infante, and M. V. Kovalenko, "Colloidal $CsPbX_3$ (X = Cl, Br, I) Nanocrystals 2.0: Zwitterionic Capping Ligands for Improved Durability and Stability," *ACS Energy Letters*, vol. 3, pp. 641–646, 2018. (see pp. 26 and 37)

[169] M. Antler and A. W. Laubengayer, "Donor-Acceptor Bonding. VI. The Reactions of Trimethylamine, Dimethylamine, Monomethylamine, and Ammonia with Titanium Tetrachloride and of Trimethylamine with Titanium Trichloride," *Journal of the American Chemical Society*, vol. 77, pp. 5250–5253, 1955. (see p. 37)

[170] R. Ouyang, "Exploiting Ionic Radii for Rational Design of Halide Perovskites," *Chemistry of Materials*, vol. 32, pp. 595–604, 1 2020. (see pp. 49 and 73)

[171] G. E. Eperon and D. S. Ginger, "B-Site Metal Cation Exchange in Halide Perovskites," *ACS Energy Letters*, vol. 2, pp. 1190–1196, 5 2017. (see p. 49)

[172] E. M. Hutter, M. C. Gélvez-Rueda, D. Bartesaghi, F. C. Grozema, and T. J. Savenije, "Band-Like Charge Transport in $Cs_2AgBiBr_6$ and Mixed Antimony-Bismuth $Cs_2AgBi_{1-x}Sb_xBr_6$ Halide Double Perovskites," *ACS Omega*, vol. 3, pp. 11655–11662, 9 2018. (see p. 49)

[173] B. Yang, F. Hong, J. Chen, Y. Tang, L. Yang, Y. Sang, X. Xia, J. Guo, H. He, S. Yang, W. Deng, and K. Han, "Colloidal Synthesis and Charge-Carrier Dynamics of $Cs_2AgSb_{1-y}Bi_yX_6$ (X=Br, Cl; 0 y 1) Double Perovskite Nanocrystals," *Angewandte Chemie*, vol. 131, pp. 2300–2305, 2019. (see pp. 49 and 50)

[174] F. Locardi, E. Sartori, J. Buha, J. Zito, M. Prato, V. Pinchetti, M. L. Zaffalon, M. Ferretti, S. Brovelli, I. Infante, L. D. Trizio, and L. Manna, "Emissive Bi-Doped Double Perovskite $Cs_2Ag_{1-x}Na_xInCl_6$ Nanocrystals," *ACS Energy Letters*, vol. 4, pp. 1976–1982, 8 2019. (see pp. 49 and 50)

[175] J. Zhou, X. Rong, P. Zhang, M. S. Molokeev, P. Wei, Q. Liu, X. Zhang, and Z. Xia, "Manipulation of Bi^{3+}/In^{3+} Transmutation and Mn^{2+} -Doping Effect on the Structure and Optical Properties of Double Perovskite $Cs_2NaBi_{1-x}In_xCl_6$," *Advanced Optical Materials*, vol. 7, 4 2019. (see p. 49)

[176] M. Chen, M. G. Ju, H. F. Garces, A. D. Carl, L. K. Ono, Z. Hawash, Y. Zhang, T. Shen, Y. Qi, R. L. Grimm, D. Pacifici, X. C. Zeng, Y. Zhou, and N. P. Padture, "Highly stable and efficient all-inorganic lead-free perovskite solar cells with native-oxide passivation," *Nature Communications*, vol. 10, 12 2019. (see p. 49)

[177] Z. Li, S. An, R. Kavanagh, M. Napari, R. G. Palgrave, M. Abdi-Jalebi, Z. Andaji-Garmaroudi, D. W. Davies, M. Laitinen, J. Julin, M. A. Isaacs, R. H. Friend, D. O. Scanlon, A. Walsh, and R. L. Z. Hoye, "Bandgap lowering in mixed alloys of $Cs_2Ag(Sb_xBi_{1-x})Br_6$ double perovskite thin films," *Journal of Materials Chemistry A*, vol. 8, 2020. (see p. 49)

[178] D. S. Dolzhnikov, C. Wang, Y. Xu, M. G. Kanatzidis, and E. A. Weiss, "Ligand-Free, Quantum-Confined Cs_2SnI_6 Perovskite Nanocrystals," *Chemistry of Materials*, vol. 29, pp. 7901–7907, 9 2017. (see p. 50)

[179] G. Zhang, J. Zhang, Y. Liao, Z. Pan, H. Rao, and X. Zhong, "Cs_2SnI_6 nanocrystals enhancing hole extraction for efficient carbon-based $CsPbI_2Br$ perovskite solar cells," *Chemical Engineering Journal*, vol. 440, 7 2022. (see p. 50)

[180] S. Ghosh, S. Paul, and S. K. De, "Control Synthesis of Air-Stable Morphology Tunable Pb-Free Cs_2SnI_6 Perovskite Nanoparticles and Their Photodetection Properties," *Particle and Particle Systems Characterization*, vol. 35, 9 2018. (see p. 50)

[181] C. Lu, M. W. Wright, X. Ma, H. Li, D. S. Itanze, J. A. Carter, C. A. Hewitt, G. L. Donati, D. L. Carroll, P. M. Lundin, and S. M. Geyer, "Cesium Oleate Precursor Preparation for Lead Halide Perovskite Nanocrystal Synthesis: The Influence of Excess Oleic Acid on Achieving Solubility, Conversion, and Reproducibility," *Chemistry of Materials*, vol. 31, pp. 62–67, 2019. (see pp. 54 and 89)

[182] C. Kupfer, J. Elia, M. Kato, A. Osvet, and C. J. Brabec, "Mechanochemical Synthesis of Cesium Titanium Halide Perovskites $Cs_2TiBr_{6-x}I_x$ (x = 0, 2, 4, 6)," *Crystal Research and Technology*, p. 2200150, 11 2022. (see p. 71)

[183] S. N. Raja, Y. Bekenstein, M. A. Koc, S. Fischer, D. Zhang, L. Lin, R. O. Ritchie, P. Yang, and A. P. Alivisatos, "Encapsulation of Perovskite Nanocrystals into Macroscale Polymer Matrices: Enhanced Stability and Polarization," *ACS Applied Materials and Interfaces*, vol. 8, pp. 35523–35533, 12 2016. (see p. 71)

[184] C. Sun, Y. Zhang, C. Ruan, C. Yin, X. Wang, Y. Wang, and W. W. Yu, "Efficient and Stable White LEDs with Silica-Coated Inorganic Perovskite Quantum Dots," *Advanced Materials*, vol. 28, pp. 10088–10094, 12 2016. (see p. 71)

[185] Z. Li, L. Kong, S. Huang, and L. Li, "Highly Luminescent and Ultrastable $CsPbBr_3$ Perovskite Quantum Dots Incorporated into a Silica/Alumina Monolith," *Angewandte Chemie*, vol. 129, pp. 8246–8250, 7 2017. (see p. 71)

[186] Z. J. Li, E. Hofman, J. Li, A. H. Davis, C. H. Tung, L. Z. Wu, and W. Zheng, "Photoelectrochemically active and environmentally stable $CsPbBr_3/TiO_2$ core/shell nanocrystals," *Advanced Functional Materials*, vol. 28, 1 2018. (see p. 72)

[187] C. Zhang, S. Wang, X. Li, M. Yuan, L. Turyanska, and X. Yang, "Core/Shell Perovskite Nanocrystals: Synthesis of Highly Efficient and Environmentally Stable $FAPbBr_3/CsPbBr_3$ for LED Applications," *Advanced Functional Materials*, vol. 30, 8 2020. (see p. 72)

[188] C. F. Lai, Y. C. Chang, and Y. C. Tien, "Stable Lead-Free Cesium Tin Halide Double-Perovskite Nanocrystals Embedded in Polydimethylsiloxane for Candlelight Light-Emitting Diodes," *ACS Applied Nano Materials*, vol. 4, pp. 1924–1931, 2 2021. (see p. 72)

[189] A. Veronese, M. Patrini, D. Bajoni, C. Ciarrocchi, P. Quadrelli, and L. Malavasi, "Highly Tunable Emission by Halide Engineering in Lead-Free Perovskite-Derivative Nanocrystals: The Cs_2SnX_6 (X = Cl, Br, Br/I, I) System," *Frontiers in Chemistry*, vol. 8, pp. 1–9, 2020. (see p. 72)

[190] J. F. Moulder, W. F. Stickle, P. E. Sobol, and K. D. Bomben, *Handbook of X-ray Photoelectron Spectroscopy*. Perkin-Elmer Corporation Physical Electronics Division 6509, 1992. (see pp. 72 and 103)

[191] M. P. Seah and W. A. Dench, "Quantitative Electron Spectroscopy of Surfaces: A Standard Data Base for Electron Inelastic Mean Free Paths in Solids," *Surface and Interface Analysis*, vol. 1, pp. 1–11, 1979. (see p. 109)

[192] J. D. Koralek, J. F. Douglas, N. C. Plumb, J. D. Griffith, S. T. Cundiff, H. C. Kapteyn, M. M. Murnane, and D. S. Dessau, "Experimental setup for low-energy laser-based angle resolved photoemission spectroscopy," *Review of Scientific Instruments*, vol. 78, 2007. (see p. 109)

[193] C. Würth, M. Grabolle, J. Pauli, M. Spieles, and U. Resch-Genger, "Relative and absolute determination of fluorescence quantum yields of transparent samples," *Nature protocols*, vol. 8, pp. 1535–1550, 2013. (see p. 110)

List of Publications

The studies reported in Chapters 2 and 3 have already been published, while the research reported in Chapters 4 and 5 will be published soon:

- *Colloidal synthesis of lead-free $Cs_2TiBr_{6-x}I_x$ perovskite nanocrystals*
  Shanti M. Liga and Gerasimos Konstantatos
  Journal of Materials Chemistry C, 2021, 9 (34), 11098-11103. (**Chapter 3**)

- *Frenkel Excitons in Vacancy-ordered Titanium Halide Perovskites (Cs_2TiX_6)*
  Seàn R. Kavanagh, Christopher N. Savory, Shanti M. Liga, Gerasimos Konstantatos, Aron Walsh and David O. Scanlon
  Journal of Physical Chemistry Letters, (2022). (**Chapter 2**)

- *Mixed tin/titanium vacancy-ordered double perovskites*
  Shanti M. Liga, Seàn R. Kavanagh, Aran Walsh, David O. Scanlon and Gerasimos Konstantatos
  (in preparation) (**Chapter 4**)

- *Increasing the stability of Cs_2TiBr_6 with $SnBr_4$ surface treatment*
  Shanti M. Liga and Gerasimos Konstantatos
  (in preparation) (**Chapter 5**)

Other publications by the author:

- *Colloidal Quantum Dot Infrared Lasers Featuring Sub-Single-Exciton Threshold and Very High Gain*
  Nima Taghipour, Mariona Dalmases, Guy L. Whitworth, Miguel Dosil, Andreas Othonos, Sotirios Christodoulou, Shanti Maria Liga, Gerasimos Konstantatos
  Advances Materials, (2022)